

Exact solution of the Falicov-Kimball model with dynamical mean-field theory

J. K. Freericks*

Department of Physics, Georgetown University, Washington, DC 20057

V. Zlatić†

Institute of Physics, Zagreb, Croatia

(Dated: October 22, 2018)

The Falicov-Kimball model was introduced in 1969 as a statistical model for metal-insulator transitions; it includes itinerant and localized electrons that mutually interact with a local Coulomb interaction and is the simplest model of electron correlations. It can be solved exactly with dynamical mean-field theory in the limit of large spatial dimensions which provides an interesting benchmark for the physics of locally correlated systems. In this review, we develop the formalism for solving the Falicov-Kimball model from a path-integral perspective, and provide a number of expressions for single and two-particle properties. We examine many important theoretical results that show the absence of fermi-liquid features and provide a detailed description of the static and dynamic correlation functions and of transport properties. The parameter space is rich and one finds a variety of many-body features like metal-insulator transitions, classical valence fluctuating transitions, metamagnetic transitions, charge density wave order-disorder transitions, and phase separation. At the same time, a number of experimental systems have been discovered that show anomalies related to Falicov-Kimball physics [including YbInCu_4 , $\text{EuNi}_2(\text{Si}_{1-x}\text{Ge}_x)_2$, NiI_2 and Ta_xN].

PACS numbers: 71.10.-W, 71.30.+h, 71.45.-d, 72.10.-d

Contents

I. Introduction	1
A. Brief History	1
B. Hamiltonian and Symmetries	3
C. Outline of the Review	4
II. Formalism	5
A. Limit of Infinite Spatial Dimensions	5
B. Single-Particle Properties (Itinerant Electrons)	6
C. Static Charge, Spin, or Superconducting Order	10
D. Dynamical Charge Susceptibility	13
E. Static and Dynamical Transport	16
F. Single-Particle Properties (Localized Electrons)	19
G. Spontaneous Hybridization	23
III. Analysis of Solutions	24
A. Charge-Density-Wave Order and Phase Separation	24
B. Mott-like Metal-Insulator Transitions	27
C. Falicov-Kimball-like Metal-Insulator Transitions	28
D. Intermediate-Valence	29
E. Transport Properties	30
F. Magnetic-Field Effects	31
G. Static Holstein Model	33
IV. Comparison with Experiment	34
A. Valence-Change Materials	34
B. Electronic Raman Scattering	39
C. Josephson Junctions	40
D. Resistivity Saturation	42
E. Pressure-Induced Metal-Insulator Transitions	43

V. New Directions	43
A. $1/d$ Corrections	43
B. Hybridization and f -Electron Hopping	46
C. Nonequilibrium Effects	46
VI. Conclusions	47
Acknowledgments	48
List of Symbols	48
References	48

I. INTRODUCTION

A. Brief History

The Falicov-Kimball model (Falicov and Kimball, 1969) was introduced in 1969 to describe metal-insulator transitions in a number of rare-earth and transition-metal compounds [but see Hubbard's earlier work (Hubbard, 1963) where the spinless version of the Falicov-Kimball model was introduced as an approximate solution to the Hubbard model; one assumes that one species of spin does not hop and is frozen on the lattice]. The initial work by Falicov and collaborators focused primarily on analyzing the thermodynamics of the metal-insulator transition with a static mean-field theory approach (Falicov and Kimball, 1969; Ramirez *et al.*, 1970). The resulting solutions displayed both continuous and discontinuous metal-insulator phase transitions, and they could fit the conductivity of a wide variety of transition-metal and rare-earth compounds with their

*Electronic address: freericks@physics.georgetown.edu;
URL: <http://www.physics.georgetown.edu/~jkf>

†Electronic address: zlati@ifs.hr

results. Next, Ramirez and Falicov (1971) applied the model to describe the $\alpha - \gamma$ phase transition in Cerium. Again, a number of thermodynamic quantities were approximated well by the model, but it did not examine any effects associated with Kondo screening of the f -electrons [and subsequently was discarded in favor of the Kondo volume collapse picture (Allen and Martin, 1982)].

Interest in the model waned once Plischke (1972) showed that when the coherent-potential-approximation (CPA) (Soven, 1967; Velický *et al.*, 1968) was applied to it, all first-order phase transitions disappeared and the solutions only displayed smooth crossovers from a metal to an insulator [this claim was strongly refuted by Falicov's group (Gonçalves da Silva and Falicov, 1972) but interest in the model was limited for almost 15 years].

The field was revitalized by mathematical physicists in the mid 1980's, who realized that the spinless version of this model is the simplest correlated system that displays long-range order at low temperatures and for dimensions greater than one. Indeed, two groups produced independent proofs of the long-range order (Brandt and Schmidt, 1986, 1987; Kennedy and Lieb, 1986; Lieb, 1986). The work by Kennedy and Lieb rediscovered Hubbard's original approximation that yields the spinless Falicov-Kimball model, and also provided a new interpretation of the model for the physics of crystallization. A number of other exact results followed including (i) a proof of no quantum-mechanical mixed valence (or spontaneous hybridization) at finite T (Subrahmanyam and Barma, 1988) [based on the presence of a local gauge symmetry and Elitzur's theorem (Elitzur, 1975)]; (ii) proofs of phase separation and of periodic ordering in one dimension (with large interaction strength) (Lemberger, 1992); (iii) proofs about ground-state properties in two dimensions (also at large interaction strength) (Haller, 2000; Haller and Kennedy, 2001; Kennedy, 1994, 1998); (iv) a proof of phase separation in one dimension and small interaction strength (Freericks *et al.*, 1996); and (v) a proof of phase separation for large interaction strength and all dimensions (Freericks *et al.*, 2002a,b). Most of these rigorous results have already been summarized in reviews (Gruber, 1999; Gruber and Macris, 1996). In addition, a series of numerical calculations were performed in one and two dimensions (de Vries *et al.*, 1993, 1994; Freericks and Falicov, 1990; Gruber *et al.*, 1994; Michielsen, 1993; Watson and Lemański, 1995). While not providing complete results for the model, the numerics do illustrate a number of important trends in the physics of the FK model.

At about the same time, there was a parallel development of the dynamical mean-field theory (DMFT), which is what we concentrate on in this review. The DMFT was invented by Metzner and Vollhardt (1989). Almost immediately after the idea that in large spatial dimensions the self energy becomes local, Brandt and collaborators showed how to solve the static problem exactly (requiring no quantum Monte Carlo), thereby providing the exact solution of

the Falicov-Kimball model (Brandt and Fledderjohann, 1992; Brandt *et al.*, 1990; Brandt and Mielsch, 1989, 1990, 1991; Brandt and Urbanek, 1992). This work is the extension of Onsager's famous solution for the transition temperature of the two-dimensional Ising model to the fermionic case (and large dimensions). These series of papers revolutionized Falicov-Kimball model physics and provided the only exact quantitative results for electronic phase transitions in the thermodynamic limit for all values of the interaction strength. They showed how to solve the infinite-dimensional DMFT model, illustrated how to determine the order-disorder transition temperature for a checkerboard (and incommensurate) charge-density-wave phase, showed how to find the free energy (including a first study of phase separation), examined properties of the spin-one-half model, and calculated the f -particle spectral function.

Further work concentrated on static properties such as charge-density-wave order (van Dongen, 1991a, 1992; van Dongen and Vollhardt, 1990; Freericks, 1993a,b; Gruber *et al.*, 2001) and phase separation (Freericks *et al.*, 1999; Freericks and Lemański, 2000; Letfulov, 1999). The original Falicov-Kimball problem of the metal-insulator transition (Chung and Freericks, 1998) was solved, as was the problem of classical intermediate valence (Chung and Freericks, 2000) [both using the spin-one-half generalization (Brandt *et al.*, 1990; Freericks and Zlatić, 1998)]. The "Mott-like" metal-insulator transition (van Dongen and Leinung, 1997) and the non-fermi-liquid behavior (Si *et al.*, 1992) were also investigated. Dynamical properties and transport have been determined ranging from the charge susceptibility (Freericks and Miller, 2000; Shvaika, 2000, 2001), to the optical conductivity (Moeller *et al.*, 1992), to the Raman response (Devereaux *et al.*, 2003; Freericks and Devereaux, 2001a,b; Freericks *et al.*, 2001a), to an evaluation of the f -spectral function (Brandt and Urbanek, 1992; Si *et al.*, 1992; Zlatić *et al.*, 2001). Finally, the static susceptibility for spontaneous polarization was also determined (Portengen *et al.*, 1996a,b; Si *et al.*, 1992; Subrahmanyam and Barma, 1988; Zlatić *et al.*, 2001).

These solutions have allowed the FK model to be applied to a number of different experimental systems ranging from valence-change-transition materials (Zlatić and Freericks, 2001a,b) like YbInCu_4 and $\text{EuNi}_2(\text{Si}_{1-x}\text{Ge}_x)_2$ to materials that can be doped through a metal-insulator transition like Ta_xN [used as a barrier in Josephson junctions (Freericks *et al.*, 2001b, 2002c; Miller and Freericks, 2001)], to Raman scattering in materials on the insulating side of the metal-insulator transition (Freericks and Devereaux, 2001b) like FeSi or SmB_6 . The model, and some straightforward modifications appropriate for double-exchange, have been used to describe the CMR materials (Allub and Alascio, 1996, 1997; Letfulov and Freericks, 2001; Ramakrishnan, 2003).

Generalizations of the FK model to the static Holstein model were first carried out by Millis *et al.* (1995, 1996) and also applied to the CMR materials. Later more fundamental properties relating to the transition temperature for the harmonic (Blawid and Millis, 2000; Ciuchi and de Pasquale, 1999) and anharmonic cases (Freericks *et al.*, 2000) and relating to the gap ratio for the harmonic (Blawid and Millis, 2001) and anharmonic cases (Freericks and Zlatić, 2001a) were completed. Modifications to examine diluted magnetic semiconductors have also appeared (Chattopadhyay *et al.*, 2001; Hwang *et al.*, 2002). A new approach to DMFT, which allows the correlated hopping Falicov-Kimball model to be solved has also been completed recently (Schiller, 1999; Shvaika, 2002).

B. Hamiltonian and Symmetries

The Falicov-Kimball model is the simplest model of correlated electrons. The original version (Falicov and Kimball, 1969) involved spin-one-half-electrons. Here, we will generalize to the case of an arbitrary degeneracy of the itinerant and localized electrons. The general Hamiltonian is then

$$\begin{aligned}
\mathcal{H} = & -t \sum_{\langle ij \rangle} \sum_{\sigma=1}^{2s+1} c_{i\sigma}^\dagger c_{j\sigma} + \sum_i \sum_{\eta=1}^{2S+1} E_{f\eta} f_{i\eta}^\dagger f_{i\eta} \\
& + U \sum_i \sum_{\sigma=1}^{2s+1} \sum_{\eta=1}^{2S+1} c_{i\sigma}^\dagger c_{i\sigma} f_{i\eta}^\dagger f_{i\eta} \\
& + \sum_i \sum_{\eta\eta'=1}^{2S+1} U_{\eta\eta'}^{ff} f_{i\eta}^\dagger f_{i\eta} f_{i\eta'}^\dagger f_{i\eta'} \\
& - g\mu_B H \sum_i \sum_{\sigma=1}^{2s+1} m_\sigma c_{i\sigma}^\dagger c_{i\sigma} \\
& - g_f \mu_B H \sum_i \sum_{\eta=1}^{2S+1} m_\eta f_{i\eta}^\dagger f_{i\eta}. \tag{1}
\end{aligned}$$

The symbols $c_{i\sigma}^\dagger$ ($c_{i\sigma}$) denote the itinerant electron creation (annihilation) operators at site i in state σ (the index σ takes $2s+1$ values). Similarly, the symbols $f_{i\eta}^\dagger$ ($f_{i\eta}$) denote the localized electron creation (annihilation) operators at site i in state η (the index η takes $2S+1$ values). Customarily, we identify the index σ and η with the z -component of spin, but the index could denote other quantum numbers in more general cases. The first term is the kinetic energy (hopping) of the conduction electrons (with t denoting the nearest-neighbor hopping integral); the summation is over nearest neighbor sites i and j (we count each pair twice to guarantee hermiticity). The second term is the localized electron site energy (which we allow to depend on the index η to include crystal-field effects [without spin-orbit coupling for simplicity]); in most applications the site-energy is taken to be η -independent. The third term is the Falicov-Kimball interaction term

(of strength U) which represents the local Coulomb interaction when itinerant and localized electrons occupy the same lattice site (we could make U depend on σ or η , but this complicates the formulas and is not normally needed). The fourth term is the ff Coulomb interaction energy of strength $U_{\eta\eta'}^{ff}$ (which can be chosen to depend on η if desired; the term with $\eta = \eta'$ is unnecessary and can be absorbed into $E_{f\eta}$). Finally, the fifth and sixth terms represent the magnetic energy due to the interaction with an external magnetic field H , with μ_B the Bohr magneton, g (g_f) the respective Landé g -factors, and m_σ (m_η) the z -component of spin for the respective states. Chemical potentials μ and μ_f are employed to adjust the itinerant and localized electron concentrations, respectively (in cases where the localized particle is fixed independently of the itinerant electron concentration, the localized particle chemical potential μ_f can be absorbed into the site-energy E_f ; in cases where the localized particles are electrons, they share a common chemical potential with the conduction electrons $\mu = \mu_f$).

The spinless case corresponds to the case where $s = S = 0$ and there is no ff interaction term because of the Pauli exclusion principle. The original Falicov-Kimball model corresponds to the case where $s = S = 1/2$, with spin-one-half electrons for both itinerant and localized cases (and the limit $U^{ff} \rightarrow \infty$).

The Hamiltonian in Eq. (1) possesses a number of different symmetries. The partial particle-hole symmetry holds on a bipartite lattice in no magnetic field ($H = 0$), where the lattice sites can be organized into two sublattices A and B , and the hopping integral only connects different sublattices. In this case, one performs a partial particle-hole symmetry transformation on either the itinerant or localized electrons (Kennedy and Lieb, 1986). The transformation includes a phase factor of (-1) for electrons on the B sublattice. When the partial particle-hole transformation is applied to the itinerant electrons,

$$c_{i\sigma} \rightarrow c_{i\sigma}^{h\dagger} (-1)^{p(i)}, \tag{2}$$

with $p(i) = 0$ for $i \in A$ and $p(i) = 1$ for $i \in B$ and h denoting the hole operators, then the Hamiltonian maps onto itself (when expressed in terms of the hole operators for the itinerant electrons), up to a numerical shift, with $U \rightarrow -U$, $E_{f\eta} \rightarrow E_{f\eta} + U$, and $\mu \rightarrow -\mu$. When applied to the localized electrons,

$$f_{i\eta} \rightarrow f_{i\eta}^{h\dagger} (-1)^{p(i)}, \tag{3}$$

the Hamiltonian maps onto itself (when expressed in terms of the hole operators for the localized electrons), up to a numerical shift with $U \rightarrow -U$, $\mu \rightarrow \mu + U$, $E_{f\eta} \rightarrow -E_{f\eta} - \sum_{\eta'} U_{\eta\eta'}^{ff} - \sum_{\eta'} U_{\eta'\eta}^{ff}$, and $\mu_f \rightarrow -\mu_f$.

These particle-hole symmetries are particularly useful when $E_{f\eta} = 0$, $\sum_{\eta'} U_{\eta\eta'}^{ff}$ does not depend on η , and we work in the canonical formalism with fixed values of ρ_e and ρ_f , the total itinerant and localized electron densities. Then, one can show that the ground-state energies

of \mathcal{H} are simply related

$$\begin{aligned} E_{g.s.}(\rho_e, \rho_f, U) &= E_{g.s.}(2s + 1 - \rho_e, \rho_f, -U) \\ &= E_{g.s.}(\rho_e, 2S + 1 - \rho_f, -U) \\ &= E_{g.s.}(2s + 1 - \rho_e, 2S + 1 - \rho_f, U), \end{aligned} \quad (4)$$

(up to constant shifts or shifts proportional to ρ_e or ρ_f) and one can restrict the phase space to $\rho_e \leq s + \frac{1}{2}$ and $\rho_f \leq S + \frac{1}{2}$.

When one or more of the Coulomb interactions are infinite, then there are additional symmetries to the Hamiltonian (Freericks *et al.*, 1999, 2002b). In the case where all $U^{ff} = \infty$, then we are restricted to the subspace $\rho_f \leq 1$. This system is formally identical to the case of spinless localized electrons, and we will develop a full solution of this limit using DMFT below. The extra symmetry is precisely that of Eq. (4), but now with $S = 0$ (*regardless of the number of η states*). Similarly, when both $U^{ff} = \infty$ and $U = \infty$, then Eq. (4) holds for $s = S = 0$ as well (*regardless of the number of σ and η states*). These infinite- U symmetries are also related to particle-hole symmetry, but now restricted to the lowest Hubbard band in the system, since all upper Hubbard bands are pushed out to infinite energy.

The Falicov-Kimball model also possesses a local symmetry, related to the localized particles. One can easily show that $[\mathcal{H}, f_{i\eta}^\dagger f_{i\eta}] = 0$, implying that the *local occupancy* of the f -electrons is conserved. Indeed, this leads to a local $U(1)$ symmetry, as the phase of the localized electrons can be rotated at will, without any effect on the Hamiltonian. Because of this local gauge symmetry, Elitzur's theorem requires that there can be no quantum-mechanical mixing of the f -particle number at finite temperature (Elitzur, 1975; Subrahmanyam and Barma, 1988), hence the system can never develop a spontaneous hybridization (except possibly at $T = 0$).

There are a number of different ways to provide a physical interpretation of the Falicov-Kimball model. In the original idea (Falicov and Kimball, 1969), we think of having itinerant and localized electrons, that can change their statistical occupancy as a function of temperature (maintaining a constant total number of electrons). This is the interpretation that leads to a metal-insulator transition due to the change in the occupancy of the different electronic levels, rather than via a change in the character of the electronic states themselves (the Mott-Hubbard approach). Another interpretation (Kennedy and Lieb, 1986), is to consider the localized particles as ions, which have an attractive interaction with the electrons. Then one can examine how the Pauli principle forces the system to minimize its energy by crystallizing into a periodic arrangement of ions and electrons (as seen in nearly all condensed-matter systems at low temperature). Finally, we can map onto a binary alloy problem (Freericks and Falicov, 1990), where the presence of an "ion" denotes the A species, and the absence of an "ion" denotes a B species, with U becoming the difference in site energies for an electron on an A or a B site.

In these latter two interpretations, the localized particle number is always a constant, and a canonical formalism is most appropriate. In the first interpretation, a grand canonical ensemble is the best approach, with a common chemical potential ($\mu = \mu_f$) for the itinerant and localized electrons.

In addition to the traditional Falicov-Kimball model, in which conduction electrons interact with a discrete set of classical variables (the localized electron-number operators), there is another class of static models that can be solved using the same kind of techniques—the static anharmonic Holstein model (Holstein, 1959; Millis *et al.*, 1995). This is a model of classical phonons interacting with conduction electrons and can be viewed as replacing the discrete spin variable of the FK model by a continuous classical field. The phonon is an Einstein mode, with infinite mass (and hence zero frequency), but nonzero spring constant. One can add any form of local anharmonic potential for the phonons into the system as well. The Hamiltonian becomes (in the spin one-half case for the conduction electrons, with one phonon mode per site)

$$\begin{aligned} \mathcal{H}_{Hol} &= -t \sum_{\langle ij \rangle \sigma} c_{i\sigma}^\dagger c_{j\sigma} + g_{ep} \sum_{i\sigma} x_i (c_{i\sigma}^\dagger c_{i\sigma} - \rho_{e\sigma}) \\ &+ \frac{1}{2} \kappa \sum_i x_i^2 + \beta_{an} \sum_i x_i^3 + \alpha_{an} \sum_i x_i^4, \end{aligned} \quad (5)$$

where, for concreteness, we assumed a quartic phonon potential. The phonon coordinate at site i is x_i , g_{ep} is the electron-phonon interaction strength (the so-called deformation potential), and the coefficients β_{an} and α_{an} measure the strength of the (anharmonic) cubic and quartic contributions to the local phonon potential. Note that the phonon couples to the fluctuations in the local electronic charge (rather than the total charge). This makes no difference for a harmonic system, where the shift in the phonon coordinate can always be absorbed, but it does make a difference for the anharmonic case, where such shifts cannot be transformed away. The particle-hole symmetry of this model is similar to that of the discrete Falicov-Kimball model, described above, except the particle-hole transformation on the phonon coordinate requires us to send $x_i \rightarrow -x_i$. Hence, the presence of a cubic contribution to the phonon potential $\beta_{an} \neq 0$, breaks the particle-hole symmetry of the system (Hirsch, 1993); in this case the phase diagram is not symmetric about half filling for the electrons. We will discuss some results of the static Holstein model, but we will not discuss any further extensions (such as including double exchange for colossal magnetoresistance materials or including interactions with classical spins to describe doped magnetic semiconductors).

C. Outline of the Review

The Falicov-Kimball model (and the static Holstein model) become exactly solvable in the limit of infinite

spatial dimensions (or equivalently when the coordination number of the lattice becomes large). This occurs because both the self energy and the (relevant) irreducible two-particle vertices are local. The procedure involves a mapping of the infinite-dimensional lattice problem onto a single-site impurity problem in the presence of a time-dependent (dynamical) mean field. The path integral for the partition function can be evaluated exactly via the so-called static approximation (in an arbitrary time-dependent field). Hence the problem is reduced to one of “quadratures” to determine the correct self-consistent dynamical mean field for the quantum system. One can next employ the Baym-Kadanoff conserving approximation approach to determine the self energies and the irreducible charge vertices (both static and dynamic). Armed with these quantities, one can calculate essentially all many-body correlation functions imaginable, ranging from static charge-density order to a dynamical Raman response. Finally, one can also calculate the properties of the f -electron spectral function, and with that, one can calculate the susceptibility for spontaneous hybridization formation. The value of the Falicov-Kimball model lies in the fact that all of these many-body properties can be determined exactly, and thereby form a useful benchmark for the properties of correlated electronic systems.

In Section II, we review the formalism that develops the exact solution for all of these different properties employing DMFT. Our attempt is to provide all details of the most important derivations, and summarizing formulae for some of the more complicated results, which are treated fully in the literature. We believe that this review provides a useful starting point for interested researchers to then understand that literature. Section III presents a summary of the results for a number of different properties of the model, concentrating mainly on the spinless and spin-one-half cases. In Section IV, we provide a number of examples where the Falicov-Kimball model can be applied to model real materials, concentrating mainly on valence-change systems like YbInCu₄. We discuss a number of interesting new directions in Section V, followed by our conclusions in Section VI.

II. FORMALISM

A. Limit of Infinite Spatial Dimensions

In 1989, Metzner and Vollhardt demonstrated that the many-body problem simplified in the limit of large dimensions (Metzner and Vollhardt, 1989); equivalently, this observation could be noted to be a simplification when the coordination number Z on a lattice becomes large. Such ideas find their origin in the justification of the inverse coordination number $1/Z$ as the small parameter governing the convergence of the coherent potential approximation (Schwartz and Siggia, 1972). Metzner and Vollhardt (1989) introduced an im-

portant scaling of the hopping matrix element

$$t = t^*/2\sqrt{d} = t^*/\sqrt{2Z} \quad (6)$$

where d is the spatial dimension. In the limit where $d \rightarrow \infty$, the hopping to nearest neighbors vanishes, but the coordination number becomes infinite—this is the only scaling that produces a nontrivial electronic density of states in the large dimensional limit. Since there is a noninteracting “band”, one can observe the effects of the competition of kinetic-energy delocalization, with potential energy localization, which forms the crux of the many-body problem. Hence, this limit provides an example where the many-body problem can be solved exactly, and these solutions can be analyzed for correlated-electron behavior.

Indeed, the central limit theorem shows that the noninteracting density of states on a hypercubic lattice $\rho_{hyp}(\epsilon)$ satisfies (Metzner and Vollhardt, 1989)

$$\rho_{hyp}(\epsilon) = \frac{1}{t^* \sqrt{\pi} \Omega_{uc}} \exp(-\epsilon^2/t^{*2}), \quad (7)$$

which follows from the fact that the band structure is a sum of cosines, which are distributed between -1 and 1 for a “general” wave-vector in the Brillouin zone (Ω_{uc} is the volume of the unit cell, which we normally take to be equal to one). Adding together d cosines will produce a sum that typically grows like \sqrt{d} , which is why the hopping is chosen to scale like $1/\sqrt{d}$. The central limit theorem then states that the distribution of these energies is in a Gaussian [an alternate derivation relying on tight-binding Green’s functions and the properties of Bessel functions can be found in Müller-Hartmann (1989a)]. Another common lattice that is examined is the infinite-coordination Bethe lattice (which can be thought of as the interior of a large Cayley tree). The noninteracting density of states is (Economou, 1983)

$$\rho_{Bethe}(\epsilon) = \frac{1}{2\pi t^{*2} \Omega_{uc}} \sqrt{4t^{*2} - \epsilon^2}, \quad (8)$$

where we used the number of neighbors $Z = 4d$ and the scaling in Eq. (6).

The foundation for DMFT comes from two facts: first the self energy is a local quantity (possesses temporal but not spatial fluctuations) and second it is a functional of the local interacting Green’s function. These observations hold for any “impurity” model as well, where the self energy can be extracted by a functional derivative of the Luttinger-Ward skeleton expansion for the self-energy generating functional (Luttinger and Ward, 1960). Hence, a solution of the impurity problem provides the functional relationship between the Green’s function and the self energy. A second relationship is found from Dyson’s equation, which expresses the local Green’s function as a summation of the momentum-dependent Green’s functions over all momenta in the Brillouin zone. Since the self energy has no momentum dependence, this relation is a simple integral relation

(called the Hilbert transformation) of the noninteracting density of states. Combining these two ideas together, in a self-consistent fashion provides the basic strategy of DMFT.

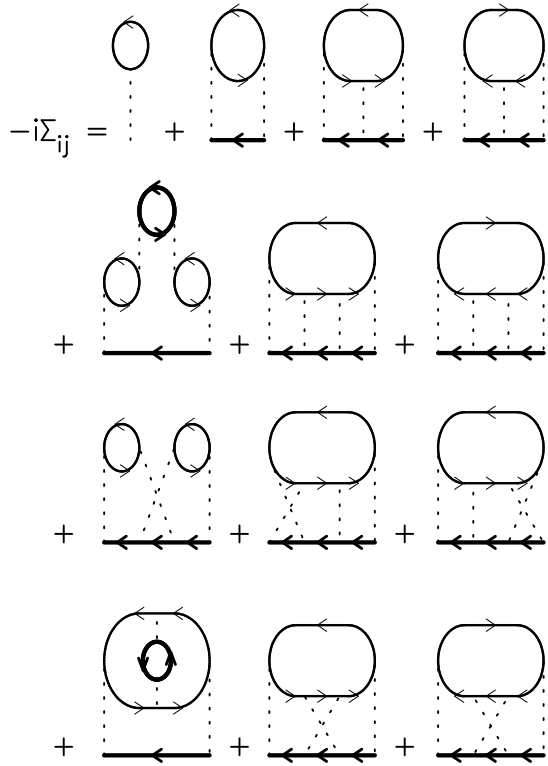


FIG. 1 Skeleton expansion for the itinerant electron self energy Σ_{ij} through fourth order. The wide solid lines denote itinerant electron Green's functions and the thin solid lines denote localized electron Green's functions; the dotted lines denote the Falicov-Kimball interaction U . The series is identical to that of the Hubbard model, except we must restrict the localized electron propagator to be diagonal in real space (which reduces the number of off-diagonal diagrams significantly). The first diagrams in the second and third rows are the only diagrams that contribute when $i \neq j$ for the Falicov-Kimball model.

For the Falicov-Kimball model, we need to establish these two facts. The locality of the self energy is established most directly from an examination of the perturbation series, where one can show nonlocal self energies are smaller by powers of $1/\sqrt{d}$. The skeleton expansion for the self energy (determined by the functional derivative of the Luttinger-Ward self-energy generating functional with respect to G), appears in Fig. 1 through fourth order in U . This expansion is identical to the expansion for the Hubbard model, except we explicitly note the localized and itinerant Green's functions graphically. Since the localized electron propagator is local (i.e. no off-diagonal spatial components), many of the diagrams in Fig. 1 are also purely local. The only nonlocal diagrams through fourth order are the first diagrams in the second and third rows. If we suppose i and j cor-

respond to nearest neighbors, then we immediately conclude that the diagram has three factors of $G_{ij} \propto 1/\sqrt{d^3}$ (each $1/\sqrt{d}$ factor comes from t_{ij}). Summing over all of the $2d$ nearest neighbors, still produces a result that scales like $1/\sqrt{d}$ in the large dimensional limit, which vanishes. A similar argument can be extended to all nonlocal diagrams (Brandt and Mielsch, 1989; Metzner, 1991). Hence, the self energy is local in the infinite-dimensional limit. The functional dependence on the local Green's function then follows from the skeleton expansion, restricted to the local self energy ($i = j$).

B. Single-Particle Properties (Itinerant Electrons)

We start our analysis by deriving the set of equations satisfied by the single-particle lattice Green's function for the itinerant electrons defined by the time-ordered product

$$G_{ij\sigma}(\tau) = -\frac{1}{\mathcal{Z}_L} \text{Tr}_{cf} \langle e^{-\beta(\mathcal{H} - \mu N - \mu_f N_f)} \mathcal{T}_\tau c_{i\sigma}(\tau) c_{j\sigma}^\dagger(0) \rangle, \quad (9)$$

where $\beta = 1/T$ is the inverse temperature, $0 \leq \tau \leq \beta$ is the imaginary time, \mathcal{Z}_L is the lattice partition function, N is the total itinerant electron number, N_f is the total localized electron number, and \mathcal{T}_τ denotes imaginary time ordering (earlier times to the right). The time dependence of the electrons is

$$c_{i\sigma}(\tau) = e^{\tau(\mathcal{H} - \mu N)} c_{i\sigma}(0) e^{-\tau(\mathcal{H} - \mu N)}, \quad (10)$$

and the trace is over all of the itinerant and localized electronic states. It is convenient to introduce a path-integral formulation using Grassman variables $\bar{\psi}_{i\sigma}(\tau)$ and $\psi_{i\sigma}(\tau)$ for the itinerant electrons at site- i with spin σ . Using the Grassman form for the coherent states, then produces the following path integral

$$G_{ij\sigma}(\tau) = -\frac{1}{\mathcal{Z}_L} \text{Tr}_f e^{-\beta(\mathcal{H}_f - \mu_f N_f)} \int \mathcal{D}\bar{\psi} \mathcal{D}\psi \psi_{i\sigma}(\tau) \bar{\psi}_{j\sigma}(0) e^{-S^L}, \quad (11)$$

for the Green's function, where \mathcal{H}_f denotes the f -electron-only piece of the Hamiltonian [corresponding to the second, fourth and sixth terms in Eq. (1)]. The lattice action associated with the Hamiltonian in Eq. (1) is

$$S^L = \sum_{ij} \sum_{\sigma=1}^{2s+1} \int_0^\beta d\tau' \bar{\psi}_{i\sigma}(\tau') \times \left[\delta_{ij} \frac{\partial}{\partial \tau'} - \frac{t_{ij}^*}{2\sqrt{d}} + \delta_{ij} (UN_{fi} - \mu - g\mu_B H m_\sigma) \right] \times \psi_{j\sigma}(\tau'), \quad (12)$$

with N_{fi} the total number of f -electrons at site i . Since the Grassman variables are antiperiodic on the interval $0 \leq \tau \leq \beta$, we can expand them in Fourier modes,

indexed by the fermionic Matsubara frequencies $i\omega_n = i\pi T(2n+1)$:

$$\psi_{i\sigma}(\tau) = T \sum_{n=-\infty}^{\infty} e^{-i\omega_n \tau} \psi_{i\sigma}(i\omega_n) \quad (13)$$

and

$$\bar{\psi}_{i\sigma}(\tau) = T \sum_{n=-\infty}^{\infty} e^{i\omega_n \tau} \bar{\psi}_{i\sigma}(i\omega_n). \quad (14)$$

In terms of this new set of Grassman variables, the lattice action becomes $S^L = T \sum_{n=-\infty}^{\infty} S_n^L$, with

$$S_n^L = \sum_{ij} \sum_{\sigma=1}^{2s+1} \left[(-i\omega_n - \mu - g\mu_B H m_{\sigma} + UN_{fi}) \delta_{ij} - \frac{t_{ij}^*}{2\sqrt{d}} \right] \bar{\psi}_{i\sigma}(i\omega_n) \psi_{j\sigma}(i\omega_n) \quad (15)$$

and the Fourier component of the local Green's function becomes

$$\begin{aligned} G_{ii\sigma}(i\omega_n) &= \int_0^{\beta} d\tau e^{i\omega_n \tau} G_{ii\sigma}(\tau) \\ &= -\frac{T}{\mathcal{Z}_L} \text{Tr}_f e^{-\beta(\mathcal{H}_f - \mu_f N_f)} \\ &\quad \times \int \mathcal{D}\bar{\psi} \mathcal{D}\psi \psi_{i\sigma}(i\omega_n) \bar{\psi}_{i\sigma}(i\omega_n) e^{-T \sum_{n'} S_{n'}^L}. \end{aligned} \quad (16)$$

Now we are ready to begin the derivation of the DMFT equations for the Green's functions. We start with the

many-body-variant of the cavity method (Georges *et al.*, 1996; Gruber *et al.*, 2001), where we separate the path integral into pieces that involve site- i only and all other terms. The action, is then broken into three pieces: (i) the local piece at site i , $S_n(i, i)$; (ii) the piece that couples to site i , $S_n(i, j)$; and the piece that does not involve site i at all, $S_n(\text{cavity})$ (called the cavity piece). Hence,

$$S_n = S_n(i, i) + S_n(i, j) + S_n(\text{cavity}) \quad (17)$$

with

$$S_n(i, i) = \sum_{\sigma=1}^{2s+1} (-i\omega_n - \mu - g\mu_B H m_{\sigma} + UN_{fi}) \times \bar{\psi}_{i\sigma}(i\omega_n) \psi_{i\sigma}(i\omega_n), \quad (18)$$

$$S_n(i, j) = - \sum_{j, t_{ij}^* \neq 0} \sum_{\sigma=1}^{2s+1} \frac{t_{ij}^*}{2\sqrt{d}} \times [\bar{\psi}_{i\sigma}(i\omega_n) \psi_{j\sigma}(i\omega_n) + \bar{\psi}_{j\sigma}(i\omega_n) \psi_{i\sigma}(i\omega_n)], \quad (19)$$

and

$$S_n(\text{cavity}) = S_n - S_n(i, i) - S_n(i, j). \quad (20)$$

Let $\mathcal{Z}_{\text{cavity}}$ and $\langle - \rangle_{\text{cavity}}$ denote the partition function and path-integral average associated with the cavity action $S_{\text{cavity}} = T \sum_n S_n(\text{cavity})$ (the path-integral average for the cavity is divided by the cavity partition function). Then the Green's function can be written as

$$\begin{aligned} G_{ii\sigma}(i\omega_n) &= -T \frac{\mathcal{Z}_{\text{cavity}}}{\mathcal{Z}_L} \text{Tr}_f e^{-\beta(\mathcal{H}_f - \mu_f N_f)} \int \mathcal{D}\bar{\psi}_i \mathcal{D}\psi_i \psi_{i\sigma}(i\omega_n) \bar{\psi}_{i\sigma}(i\omega_n) e^{-T \sum_{n'} S_{n'}(i, i)} \\ &\quad \times \left\langle \exp \left\{ T \sum_{n'=-\infty}^{\infty} \sum_{j, t_{ij}^* \neq 0} \sum_{\sigma'=1}^{2s+1} \frac{t_{ij}^*}{2\sqrt{d}} [\bar{\psi}_{i\sigma'}(i\omega_{n'}) \psi_{j\sigma'}(i\omega_{n'}) + \bar{\psi}_{j\sigma'}(i\omega_{n'}) \psi_{i\sigma'}(i\omega_{n'})] \right\} \right\rangle_{\text{cavity}}. \end{aligned} \quad (21)$$

A simple power-counting argument, shows that only the second moment of the exponential factor in the cavity average contributes as $d \rightarrow \infty$ (Georges *et al.*, 1996), which then becomes

$$\begin{aligned} G_{ii\sigma}(i\omega_n) &= -T \frac{\mathcal{Z}_{\text{cavity}}}{\mathcal{Z}_L} \text{Tr}_f e^{-\beta(\mathcal{H}_f - \mu_f N_f)} \int \mathcal{D}\bar{\psi}_i \mathcal{D}\psi_i \psi_{i\sigma}(i\omega_n) \bar{\psi}_{i\sigma}(i\omega_n) \\ &\quad \times \exp \left[T \sum_{n'=-\infty}^{\infty} \sum_{\sigma'=1}^{2s+1} \{ i\omega_{n'} + \mu + g\mu_B H m_{\sigma'} - UN_{fi} - \lambda_{i\sigma'}(i\omega_{n'}) \} \bar{\psi}_{i\sigma'}(i\omega_{n'}) \psi_{i\sigma'}(i\omega_{n'}) \right]. \end{aligned} \quad (22)$$

with $\lambda_{i\sigma}(i\omega_n)$ the function that results from the second-moment average that is called the dynamical mean field. On a Bethe lattice, one finds $\lambda_{i\sigma}(i\omega_n) = t^{*2} G_{ii\sigma}(i\omega_n)$, while on a general lattice, one finds $\lambda_{i\sigma}(i\omega_n) = \sum_{jk} t_{ij}^* t_{ik} [G_{jk\sigma}(i\omega_n) - G_{ji\sigma}(i\omega_n) G_{ik\sigma}(i\omega_n) / G_{ii\sigma}(i\omega_n)]$ (Georges *et al.*, 1996). But the exact form is not important for deriving the DMFT equations. Instead we simply need to note that after integrating over the cavity, we find an impurity path integral for the Green's function (after defining the impurity partition function via $\mathcal{Z}_{\text{imp}} = \mathcal{Z}_L / \mathcal{Z}_{\text{cavity}}$)

$$G_{ii\sigma}(i\omega_n) = -\frac{\partial \ln \mathcal{Z}_{\text{imp}}}{\partial \lambda_{i\sigma}(i\omega_n)},$$

$$\mathcal{Z}_{imp} = \text{Tr}_f e^{-\beta(\mathcal{H}_f - \mu_f N_f)} \int \mathcal{D}\bar{\psi}_i \mathcal{D}\psi_i \exp[T \sum_{n=-\infty}^{\infty} \sum_{\sigma=1}^{2s+1} \{\i\omega_n + \mu + g\mu_B H m_\sigma - U N_{fi} - \lambda_{i\sigma}(i\omega_n)\} \bar{\psi}_{i\sigma}(i\omega_n) \psi_{i\sigma}(i\omega_n)]. \quad (23)$$

The impurity partition function is easy to calculate, because the effective action is quadratic in the Grassman variables. Defining $\mathcal{Z}_{0\sigma}(\mu)$ by

$$\mathcal{Z}_{0\sigma}(\mu) = 2e^{\beta\mu/2} \prod_{n=-\infty}^{\infty} \frac{i\omega_n + \mu - \lambda_{n\sigma}}{i\omega_n}, \quad (24)$$

[where we used the notation $\lambda_{n\sigma} = \lambda_{i\sigma}(i\omega_n)$ and adjusted the prefactor to give the noninteracting result] allows us to write the partition function as

$$\mathcal{Z}_{imp} = \text{Tr}_f \exp[-\beta(\mathcal{H}_{fi} - \mu_f N_{fi})] \times \prod_{\sigma=1}^{2s+1} \mathcal{Z}_{0\sigma}(\mu + g\mu_B H m_\sigma - U N_{fi}). \quad (25)$$

[$\mathcal{Z}_{0\sigma}$ is the generating functional for the $U = 0$ impurity problem and satisfies the relation $\mathcal{Z}_{0\sigma} = \text{Det} G_{0\sigma}^{-1}$, with $G_{0\sigma}^{-1}$ defined below in frequency space in Eq. (29).] It is cumbersome to write out the trace over the fermionic states in Eq. (25) for the general case. The spin-one-half case appears in Brandt *et al.* (1990). Here we consider only the strong-interaction limit, where $U^{ff} \rightarrow \infty$, so that there is no double occupancy of the f -electrons. In this case, we find

$$\begin{aligned} \mathcal{Z}_{imp} &= \prod_{\sigma=1}^{2s+1} \mathcal{Z}_{0\sigma}(\mu + g\mu_B H m_\sigma) \\ &+ \sum_{\eta=1}^{2S+1} e^{-\beta(E_{f\eta} - \mu_f - g_f \mu_B H m_\eta)} \\ &\times \prod_{\sigma=1}^{2s+1} \mathcal{Z}_{0\sigma}(\mu + g\mu_B H m_\sigma - U). \end{aligned} \quad (26)$$

Evaluating the derivative yields

$$G_{n\sigma} = \frac{w_0}{i\omega_n + \mu + g\mu_B H m_\sigma - \lambda_{n\sigma}} + \frac{w_1}{i\omega_n + \mu + g\mu_B H m_\sigma - \lambda_{n\sigma} - U}, \quad (27)$$

with

$$w_0 = \prod_{\sigma=1}^{2s+1} \mathcal{Z}_{0\sigma}(\mu + g\mu_B H m_\sigma) / \mathcal{Z}_{imp}, \quad (28)$$

and $w_1 = 1 - w_0$. The weight w_1 equals the average f -electron concentration ρ_f . If we relaxed the restriction $U^{ff} \rightarrow \infty$, then we would have additional terms corresponding to w_i , with $1 < i \leq 2S + 1$. Defining the effective medium (or bare Green's function) via

$$[G_{0\sigma}(i\omega_n)]^{-1} = i\omega_n + \mu + g\mu_B H m_\sigma - \lambda_{n\sigma}, \quad (29)$$

allows us to re-express Eq. (27) as

$$G_{n\sigma} = \frac{w_0}{G_{0\sigma}^{-1}(i\omega_n)} + \frac{w_1}{G_{0\sigma}^{-1}(i\omega_n) - U}, \quad (30)$$

which is a form that often appears in the literature. Dyson's equation for the impurity self energy is

$$\Sigma_{n\sigma} = \Sigma_\sigma(i\omega_n) = [G_{0\sigma}(i\omega_n)]^{-1} - [G_\sigma(i\omega_n)]^{-1}. \quad (31)$$

This impurity self energy is equated with the local self energy of the lattice (since they satisfy the same skeleton expansion with respect to the local Green's function). We can calculate the local Green's function directly from this self energy by performing a spatial Fourier transform of the momentum-dependent Green's function on the lattice:

$$\begin{aligned} G_{n\sigma} &= \sum_{\mathbf{k}} G_{n\sigma}(\mathbf{k}) \\ &= \sum_{\mathbf{k}} \frac{1}{i\omega_n + \mu + g\mu_B H m_\sigma - \Sigma_{n\sigma} - \epsilon_{\mathbf{k}}} \\ &= \int d\epsilon \rho(\epsilon) \frac{1}{i\omega_n + \mu + g\mu_B H m_\sigma - \Sigma_{n\sigma} - \epsilon} \end{aligned} \quad (32)$$

where $\epsilon_{\mathbf{k}}$ is the noninteracting bandstructure. This relation is called the Hilbert transformation of the noninteracting density of states. Equating the Green's function in Eq. (32) to that in Eq. (30) is the self consistency relation of DMFT. Substituting Eq. (31) into Eq. (30) to eliminate the bare Green's function, produces a quadratic equation for the self energy, solved by Brandt and Mielsch (1989, 1990)

$$\Sigma_{n\sigma} = \frac{1}{2} \left[U - \frac{1}{G_{n\sigma}} \pm \sqrt{\left(U - \frac{1}{G_{n\sigma}} \right)^2 + 4w_1 \frac{U}{G_{n\sigma}}} \right], \quad (33)$$

which is the *exact summation of the skeleton expansion for the self energy in terms of the interacting Green's function* (the sign in front of the square root is chosen to preserve analyticity of the self energy). Note that because w_1 is a complicated functional of G_n and Σ_n , Eq. (33) actually corresponds to a highly nonlinear functional relation between the Green's function and the self energy.

There are two independent strategies that one can employ to calculate the FK model Green's functions. The original method of Brandt and Mielsch is to substitute Eq. (33) into Eq. (32), which produces a transcendental equation for $G_{n\sigma}$ in the complex plane (Brandt and Mielsch, 1989, 1990) (for fixed w_1). This equation can be solved by a one-dimensional *complex* root-finding technique (typically Newton's method

or Mueller's method is employed), as long as one pays attention to maintaining the analyticity of the self energy by choosing the proper sign for the square root [for large U , the sign changes at a critical value of the Matsubara frequency (Freericks, 1993a)]. The other technique is the iterative technique first introduced by Jarrell (1992), which is the most commonly used method. One starts the algorithm either with $\Sigma_{n\sigma} = 0$ or with it chosen appropriately from an earlier calculation. Evaluating Eq. (32) for $G_{n\sigma}$ then allows one to calculate G_0 from Eq. (31). If we work at fixed chemical potential and fixed E_f , then we must determine w_0 and w_1 from Eq. (28); this step is not necessary if w_0 and w_1 are fixed in a canonical ensemble. Eq. (30) is employed to find the new Green's function, and Eq. (31) is used to extract the new self energy. The algorithm then iterates to convergence by starting with this new self energy. Typically, the algorithm converges to eight decimal points in less than 100 iterations, but for some regions of parameter space the equations can either converge very slowly, or not converge at all. Convergence can be accelerated by averaging the last iteration with the new result for determining the new self energy, but there are regions of parameter space where the iterative technique does not appear to converge.

Once w_0 , w_1 , and μ are known from the imaginary-axis calculation, one can employ the analytic continuation of Eqs. (30–32) (with $i\omega_n \rightarrow \omega + i0^+$) to calculate $G_\sigma(\omega)$ on the real axis. In general, the convergence is slower on the real axis, than on the imaginary axis, with the spectral weight slowest to converge near correlation-induced “band edges”. A stringent consistency test of this technique is a comparison of the Green's function calculated directly on the imaginary axis to that found from the spectral formula

$$G_\sigma(z) = \int d\omega \frac{A_\sigma(\omega)}{z - \omega + i0^+}, \quad (34)$$

with

$$A_\sigma(\omega) = \int d\epsilon \rho(\epsilon) A_\sigma(\epsilon, \omega), \quad (35)$$

and

$$A_\sigma(\epsilon, \omega) = -\frac{1}{\pi} \text{Im} \frac{1}{\omega + \mu + g\mu_B H m_\sigma - \Sigma_\sigma(\omega) - \epsilon + i0^+} \quad (36)$$

[the infinitesimal 0^+ is needed only when $\text{Im}\Sigma_\sigma(\omega) = 0$]. Note that this definition of the interacting DOS has the chemical potential located at $\omega = 0$.

In zero magnetic field, one need perform these calculations for one σ state only, since all $G_{n\sigma}$'s are equal, but in a magnetic field, one must perform $2s + 1$ parallel calculations to determine the $G_{n\sigma}$'s.

Our derivation of the single-particle Green's functions has followed a path-integral approach throughout. One could have used an equation of motion approach instead. This technique has been reviewed in Zlatić *et al.* (2001).

The formalism for the static Holstein model is similar (Millis *et al.*, 1996). Taking η to be a continuous variable (x) and $H = 0$, we find

$$\mathcal{Z}_{imp} = \int_{-\infty}^{\infty} dx \prod_{\sigma=1}^{2s+1} \mathcal{Z}_{0\sigma}(\mu - g_{ep}x) \times \exp(-\beta[\frac{1}{2}\kappa x^2 + \beta_{an}x^3 + \alpha_{an}x^4]), \quad (37)$$

$$G_{n\sigma} = \int_{-\infty}^{\infty} dx \frac{w(x)}{i\omega_n + \mu - g_{ep}x - \lambda_{n\sigma}}, \quad (38)$$

and

$$w(x) = \prod_{\sigma=1}^{2s+1} \mathcal{Z}_{0\sigma}(\mu - g_{ep}x) \times \exp(-\beta[\frac{1}{2}\kappa x^2 + \beta_{an}x^3 + \alpha_{an}x^4]) / \mathcal{Z}_{imp}. \quad (39)$$

These equations (37–39) and Eqs. (31) and (32) are all that are needed to determine the Green's functions by using the iterative algorithm.

The final single-particle quantity of interest is the Helmholtz free energy per lattice site $F_{Helm.}$. We restrict our discussion to the case of zero magnetic field $H = 0$ and to $E_{f\eta} = E_f$ (no η dependence to E_f). There are two equivalent ways to calculate the free energy. The original method uses the noninteracting functional form for the free energy, with the interacting density of states $A(\epsilon)$ replacing the noninteracting density of states $\rho(\epsilon)$ (Plischke, 1972; Ramirez *et al.*, 1970)

$$\begin{aligned} F_{Helm.}(\text{lattice}) &= (2s + 1) \int d\epsilon f(\epsilon) A(\epsilon)(\epsilon + \mu) + E_f n_f \\ &+ (2s + 1)T \int d\epsilon \left\{ f(\epsilon) \ln f(\epsilon) \right. \\ &+ [1 - f(\epsilon)] \ln[1 - f(\epsilon)] \left. \right\} A(\epsilon) \\ &+ T[w_1 \ln w_1 + w_0 \ln w_0 - w_1 \ln(2S + 1)], \end{aligned} \quad (40)$$

where $f(\epsilon) = 1/[1 + \exp(\beta\epsilon)]$ is the Fermi-Dirac distribution function. This form has the itinerant electron energy (plus interactions) and the localized electron energy on the first line [the shift by μ is needed because $A(\epsilon)$ is defined to have $\epsilon = 0$ lie at the chemical potential μ], the itinerant electron entropy on the second and third lines, and the localized electron entropy on the fourth line. Note that the total energy does not need the standard many-body correction to remove double counting of the interaction because the localized particles commute with the Hamiltonian (Fetter and Walecka, 1971).

The Brandt-Mielsch approach is different (Brandt and Mielsch, 1991) and is based on the equality of the impurity and the lattice Luttinger-Ward self-energy generating functionals Φ . A general conserving analysis (Baym, 1962) shows that the lattice free energy satisfies

$$F_{Helm.}(\text{lattice}) = T\Phi_{latt} - T \sum_{n\sigma} \Sigma_{n\sigma} G_{n\sigma}$$

$$\begin{aligned}
& + T \sum_{n\sigma} \int d\epsilon \rho(\epsilon) \ln \left[\frac{1}{i\omega_n + \mu + g\mu_B H m_\sigma - \Sigma_{n\sigma} - \epsilon} \right] \\
& + \mu \rho_e + \mu_f w_1 \quad (41)
\end{aligned}$$

while the impurity (or atomic) free energy satisfies (Brandt and Mielsch, 1991)

$$\begin{aligned}
F_{Helm.}(\text{impurity}) &= T \Phi_{imp} - T \sum_{n\sigma} \Sigma_{n\sigma} G_{n\sigma} \\
& + T \sum_{n\sigma} \ln G_{n\sigma} + \mu \rho_e + \mu_f w_1. \quad (42)
\end{aligned}$$

The first two terms on the right hand side of Eqs. (41) and (42) are equal, so we immediately learn that

$$\begin{aligned}
F_{Helm.}(\text{lattice}) &= -T \ln \mathcal{Z}_{imp} - T \sum_{n\sigma} \int d\epsilon \rho(\epsilon) \\
& \times \ln[(i\omega_n + \mu + g\mu_B H m_\sigma - \Sigma_{n\sigma} - \epsilon) G_{n\sigma}] + \mu \rho_e + \mu_f w_1 \quad (43)
\end{aligned}$$

since $F_{Helm.}(\text{impurity}) = -T \ln \mathcal{Z}_{imp} + \mu \rho_e + \mu_f w_1$. The equivalence of Eqs. (40) and (43) has been explicitly shown (Shvaika and Freericks, 2002). When calculating these terms numerically, one needs to use caution to ensure that sufficient Matsubara frequencies are employed to guarantee convergence of the summation in Eq. (43).

C. Static Charge, Spin, or Superconducting Order

The FK model undergoes a number of different phase transitions as a function of the parameters of the system.

Many of these transitions are continuous (second-order) transitions, that can be described by the divergence of a static susceptibility at the transition temperature T_c . Thus, it is useful to examine how one can calculate different susceptibilities within the FK model. In this section, we will examine the charge susceptibility for arbitrary spin, and then will consider the spin and superconducting susceptibilities for the spin-one-half model. In addition, we will examine how one can perform an ordered phase calculation when such an ordered phase exists. Our discussion follows closely that of Brandt and Mielsch (1989, 1990); Freericks and Zlatić (1998) and we consider only the case of vanishing external magnetic field $H = 0$ and the case when $E_{f\eta}$ has no η dependence.

We begin with the static itinerant-electron charge susceptibility in real space defined by (our extra factor of $2s + 1$ makes the normalization simpler)

$$\begin{aligned}
\chi^{cc}(\mathbf{R}_i - \mathbf{R}_j) &= \frac{1}{2s + 1} \int_0^\beta d\tau [\text{Tr}_{cf} \frac{\langle e^{-\beta \mathcal{H}} n_i^c(\tau) n_j^c(0) \rangle}{\mathcal{Z}_L} \\
& - \text{Tr}_{cf} \frac{\langle e^{-\beta \mathcal{H}} n_i^c \rangle}{\mathcal{Z}_L} \text{Tr}_{cf} \frac{\langle e^{-\beta \mathcal{H}} n_j^c \rangle}{\mathcal{Z}_L}], \quad (44)
\end{aligned}$$

where \mathcal{Z}_L is the lattice partition function, $n_i^c = \sum_{\sigma=1}^{2s+1} c_{i\sigma}^\dagger c_{i\sigma}$ and $n_i^c(\tau) = \exp[\tau(\mathcal{H} - \mu N)] n_i^c(0) \exp[-\tau(\mathcal{H} - \mu N)]$. If we imagine introducing a symmetry breaking field $-\sum_i \bar{h}_i n_i^c$ to the Hamiltonian, then we can evaluate the susceptibility as a derivative with respect to this field (in the limit where $\bar{h} = 0$)

$$\chi^{cc}(\mathbf{R}_i - \mathbf{R}_j) = \frac{T}{2s + 1} \sum_n \sum_\sigma \frac{dG_{jj\sigma}(i\omega_n)}{d\bar{h}_i} = -\frac{T}{2s + 1} \sum_n \sum_\sigma \sum_{kl} G_{jk\sigma}(i\omega_n) \frac{dG_{kl\sigma}^{-1}(i\omega_n)}{d\bar{h}_i} G_{lj\sigma}(i\omega_n). \quad (45)$$

Since $G_{kl\sigma}^{-1} = [i\omega_n + \mu + \bar{h}_k - \Sigma_{kk\sigma}(i\omega_n)] \delta_{kl} - t_{kl}^*/2\sqrt{d}$, we find

$$\chi^{cc}(\mathbf{R}_i - \mathbf{R}_j) = \frac{T}{2s + 1} \sum_n \sum_\sigma \left[-G_{ij\sigma}(i\omega_n) G_{ji\sigma}(i\omega_n) + \sum_k \sum_{\sigma'} \sum_m G_{jk\sigma}(i\omega_n) G_{kj\sigma}(i\omega_n) \frac{d\Sigma_{kk\sigma}(i\omega_n)}{dG_{kk\sigma'}(i\omega_m)} \frac{dG_{kk\sigma'}(i\omega_m)}{d\bar{h}_i} \right], \quad (46)$$

where we used the chain rule to relate the derivative of the local self energy with respect to the field to a derivative with respect to G times a derivative of G with respect to the field (recall, the self energy is a functional of the local Green's function). It is easy to verify that both $G_{ij\sigma} G_{ji\sigma}$ and $dG_{jj\sigma}/d\bar{h}_i$ are independent of σ (indeed, this is why we set the external magnetic field to zero). If we now perform a spatial Fourier transform of Eq. (46), we find Dyson's equation

$$\chi_n^{cc}(\mathbf{q}) = \chi_n^{cc0}(\mathbf{q}) - T \sum_m \chi_n^{cc0}(\mathbf{q}) \Gamma_{nm}^{cc} \chi_m^{cc}(\mathbf{q}), \quad (47)$$

where we have defined

$$\begin{aligned}
\chi_n^{cc}(\mathbf{q}) &= \frac{1}{V} \sum_{\mathbf{R}_i - \mathbf{R}_j} \frac{1}{2s + 1} \sum_\sigma \frac{dG_{ii\sigma}(i\omega_n)}{d\bar{h}_j} e^{i\mathbf{q} \cdot (\mathbf{R}_i - \mathbf{R}_j)}, \\
\chi_n^{cc0}(\mathbf{q}) &= -\frac{1}{V} \sum_{\mathbf{R}_i - \mathbf{R}_j} \frac{1}{2s + 1} \sum_\sigma G_{ij\sigma}(i\omega_n) G_{ji\sigma}(i\omega_n) \\
& \times e^{i\mathbf{q} \cdot (\mathbf{R}_i - \mathbf{R}_j)}, \\
\Gamma_{nm}^{cc} &= \frac{1}{T} \frac{1}{2s + 1} \sum_{\sigma\sigma'} \frac{d\Sigma_\sigma(i\omega_n)}{dG_{\sigma'}(i\omega_m)}, \quad (48)
\end{aligned}$$

V is the number of lattice sites and $\chi^{cc}(\mathbf{q}) =$

$T \sum_n \chi_n^{cc}(\mathbf{q})$. The fact that we have taken a Fourier transform, implies that we are considering a periodic lattice here (like the hypercubic lattice); we will discuss below where these results are applicable to the Bethe lattice. Note that it seems like we have made an assumption that the irreducible vertex is local. Indeed, the vertex for the lattice is not local, because the second functional derivative of the lattice Luttinger-Ward functional with respect to G does have nonlocal contributions as $d \rightarrow \infty$. These nonlocal corrections are only for a set of measure zero of \mathbf{q} -values (Georges *et al.*, 1996; Hettler *et al.*, 2000; Zlatić and Horvatić, 1990), and one can safely replace the vertex by its local piece within any momentum summations, which is why Eqs. (47) and (48) are correct.

The local irreducible vertex function Γ can be determined by taking the relevant derivatives of the skeleton expansion for the impurity self energy in Eq. (33). The self energy depends explicitly on G_n and implicitly through w_1 . It is because w_1 has G dependence that the vertex function differs from that of the coherent potential approximation (where the derivative of w_1 with respect to G would be zero). The irreducible vertex becomes

$$\Gamma_{nm}^{cc} = \frac{1}{(2s+1)T} \sum_{\sigma\sigma'} \left\{ \left(\frac{\partial \Sigma_{n\sigma}}{\partial G_{n\sigma}} \right)_{w_1} \delta_{\sigma\sigma'} \delta_{mn} + \left(\frac{\partial \Sigma_{n\sigma}}{\partial w_1} \right)_{G_{n\sigma}} \left(\frac{\partial w_1}{\partial G_{m\sigma'}} \right) \right\}. \quad (49)$$

Substituting the irreducible vertex into the Dyson equation [Eq. (47)], then yields

$$\chi_n^{cc}(\mathbf{q}) = \chi_n^{cc0}(\mathbf{q}) \frac{1 - (\partial \Sigma_{n\sigma_1} / \partial w_1)_{G_{n\sigma_1}} \gamma(\mathbf{q})}{1 + \chi_n^{cc0}(\mathbf{q}) (\partial \Sigma_{n\sigma_1} / \partial G_{n\sigma_1})_{w_1}}, \quad (50)$$

with the function $\gamma(\mathbf{q})$ defined by

$$\gamma(\mathbf{q}) = \sum_n \chi_n^{cc}(\mathbf{q}) \sum_{\sigma} \left(\frac{\partial w_1}{\partial G_{n\sigma}} \right), \quad (51)$$

and we have chosen a particular spin state σ_1 to evaluate the derivatives in Eq. (50) since they do not depend on σ_1 . Multiplying Eq. (50) by $\sum_{\sigma} (\partial w_1 / \partial G_{n\sigma})$ and summing over n yields an equation for $\gamma(\mathbf{q})$. Defining $Z_{n\sigma} = i\omega_n + \mu - \lambda_{n\sigma} = G_{n\sigma}^{-1} + \Sigma_{n\sigma}$ and noting that $\partial w_1 / \partial G_n = \sum_m [\partial w_1 / \partial Z_m] [\partial Z_m / \partial G_n]$, allows us to replace $\partial w_1 / \partial G_n$ by

$$\frac{\partial w_1}{\partial G_n} = - \frac{\frac{\partial w_1}{\partial Z_n} \left[1 - G_n^2 \left(\frac{\partial \Sigma_n}{\partial G_n} \right)_{w_1} \right]}{G_n^2 \left[1 - \sum_m \frac{\partial w_1}{\partial Z_m} \left(\frac{\partial \Sigma_m}{\partial w_1} \right)_{G_n} \right]}, \quad (52)$$

and solve the equation for $\gamma(\mathbf{q})$ to yield

$$\gamma(\mathbf{q}) = \frac{\sum_{n\sigma} \partial w_1 / \partial Z_{n\sigma} [1 - G_n^2 (\partial \Sigma_n / \partial G_n)_{w_1}] / [1 + G_n \eta_n(\mathbf{q}) - G_n^2 (\partial \Sigma_n / \partial G_n)_{w_1}]}{1 - \sum_{n\sigma} \partial w_1 / \partial Z_{n\sigma} G_n \eta_n(\mathbf{q}) (\partial \Sigma_n / \partial w_1)_{G_n} / [1 + G_n \eta_n(\mathbf{q}) - G_n^2 (\partial \Sigma_n / \partial G_n)_{w_1}]}, \quad (53)$$

with $\eta_n(\mathbf{q})$ defined by

$$\eta_n(\mathbf{q}) = G_n \left[-\frac{1}{G_n^2} - \frac{1}{\chi_n^{cc0}(\mathbf{q})} \right], \quad (54)$$

and we have dropped the explicit σ dependence for G and Σ . The full charge-density-wave susceptibility then follows

$$\chi^{cc}(\mathbf{q}) = -T \sum_n \frac{[1 - \gamma(\mathbf{q}) (\partial \Sigma_n / \partial w_1)_{G_n}] G_n^2}{1 + G_n \eta_n(\mathbf{q}) - G_n^2 (\partial \Sigma_n / \partial G_n)_{w_1}}. \quad (55)$$

The derivatives needed in Eqs. (53) and (55) can be determined straightforwardly:

$$\sum_{\sigma=1}^{2s+1} \frac{\partial w_1}{\partial Z_{n\sigma}} = \frac{(2s+1)w_1(1-w_1)UG_n^2}{(1+G_n\Sigma_n)[1+G_n(\Sigma_n-U)]}, \quad (56)$$

$$1 - G_n^2 \left(\frac{\partial \Sigma_n}{\partial G_n} \right)_{w_1} = \frac{(1+G_n\Sigma_n)[1+G_n(\Sigma_n-U)]}{1+G_n(2\Sigma_n-U)}, \quad (57)$$

and

$$G_n^2 \left(\frac{\partial \Sigma_n}{\partial w_1} \right)_{G_n} = \frac{UG_n^2}{1+G_n(2\Sigma_n-U)}. \quad (58)$$

The final expression for the susceptibility and for $\gamma(\mathbf{q})$ appears in Table I.

The mixed cf susceptibilities can be calculated by taking derivatives of w_1 with respect to \bar{h}_i as shown in Brandt and Mielsch (1989) and Freericks and Zlatić (1998). We won't repeat the details here, just the end result in Table I. The calculation of the ff susceptibilities is similar. By recognizing that we could have calculated the cf susceptibility by adding a local f -electron chemical potential and taking the derivative of the itinerant electron concentration with respect to the local field, we can derive a relation between the cf and ff susceptibilities. These results are also summarized in the table.

In addition to charge susceptibilities, we also can calculate spin and pair-field susceptibilities for $s > 0$. We consider the spin-one-half case in detail. The spin susceptibility vertex simplifies, since the off-diagonal terms

now cancel, and one finds a relatively simple result. The mixed cf spin susceptibility vanishes (because the Green's function depends only on the total f -electron concentration). The ff spin susceptibility is difficult to determine in general, but it assumes a Curie form for $\mathbf{q} = 0$. The pair-field susceptibility is determined by employing a Nambu-Gor'kov formalism and taking the limit where the pair-field vanishes. There is an off-diagonal dynamical mean field analogous to λ_n and w_1 depends quadratically on this off-diagonal field. Hence, in the normal state, the irreducible pair-field vertex is diagonal in the Matsubara frequencies, just like the spin vertex. This means the susceptibility is easy to calculate as a function of the bare pair-field susceptibility

$$\bar{\chi}_n^{cc0}(\mathbf{q}) = -\frac{1}{V} \sum_{\mathbf{R}_i - \mathbf{R}_j} G_{ij\uparrow}(i\omega_n) G_{ji\downarrow}(-i\omega_n) e^{i\mathbf{q} \cdot (\mathbf{R}_i - \mathbf{R}_j)}. \quad (59)$$

The result appears in Table I.

The cc charge susceptibility diverges whenever $\gamma(\mathbf{q})$ diverges, which happens when the denominator in Table I vanishes. Since this denominator is identical for the cc , cf , and ff susceptibilities, all three diverge at the same transition temperature as we would expect. This yields the same result as found in Brandt and Mielsch (1989, 1990) for the spinless case, except there is an additional factor of $2s + 1$ multiplying the sum in the denominator arising from the $2s + 1$ derivatives of w_1 , which are all equal. This factor “essentially” increases T_c by $2s + 1$ over that found in the spinless case. The existence of a T_c is easy to establish, since the summation in the denominator goes to zero like $1/T^4$ for large T and diverges like C/T for small T . If $C > 0$, then there is a transition.

The \mathbf{q} -dependence of the charge susceptibility comes entirely from $\eta_n(\mathbf{q})$ and hence from the bare susceptibility

$$\begin{aligned} \chi_n^{cc0}(\mathbf{q}) &= -\sum_{\mathbf{k}} G_n(\mathbf{k} + \mathbf{q}) G_n(\mathbf{k}) \\ &= -\frac{1}{\sqrt{1 - X^2}} \int_{-\infty}^{\infty} d\epsilon \frac{\rho(\epsilon)}{i\omega_n + \mu - \Sigma_n - \epsilon} \\ &\times F_{\infty} \left[\frac{i\omega_n + \mu - \Sigma_n - X\epsilon}{\sqrt{1 - X^2}} \right], \end{aligned} \quad (60)$$

where all of the \mathbf{q} -dependence can be summarized

$$G_{n\sigma}^{A,B}(\mathbf{q}) = \frac{i\omega_n + \mu + g\mu_B H m_{\sigma} - \Sigma_{n\sigma}^{B,A} + \epsilon_{\mathbf{q}}}{(i\omega_n + \mu + g\mu_B H m_{\sigma} - \Sigma_{n\sigma}^A)(i\omega_n + \mu + g\mu_B H m_{\sigma} - \Sigma_{n\sigma}^B) - \epsilon_{\mathbf{q}}^2}, \quad (61)$$

which can be summed over \mathbf{q} to yield

$$\begin{aligned} G_{n\sigma}^A &= \int d\epsilon \frac{\rho(\epsilon)}{\bar{Z}_{n\sigma} - \epsilon} \frac{i\omega_n + \mu + g\mu_B H m_{\sigma} - \Sigma_{n\sigma}^B}{\bar{Z}_{n\sigma}}, & G_{n\sigma}^B &= \int d\epsilon \frac{\rho(\epsilon)}{\bar{Z}_{n\sigma} - \epsilon} \frac{i\omega_n + \mu + g\mu_B H m_{\sigma} - \Sigma_{n\sigma}^A}{\bar{Z}_{n\sigma}}, \\ \bar{Z}_{n\sigma} &= \sqrt{(i\omega_n + \mu + g\mu_B H m_{\sigma} - \Sigma_{n\sigma}^A)(i\omega_n + \mu + g\mu_B H m_{\sigma} - \Sigma_{n\sigma}^B)}. \end{aligned} \quad (62)$$

in a single parameter $X(\mathbf{q}) = \lim_{d \rightarrow \infty} \sum_{i=1}^d \cos q_i / d$ (Müller-Hartmann, 1989a) and we use $F_{\infty}(z) = \int d\epsilon \rho(\epsilon) / (z - \epsilon)$ to denote the Hilbert transform. The results for $\chi_n^{cc0}(\mathbf{q})$ and $\eta_n(\mathbf{q})$ simplify for three general cases (Brandt and Mielsch, 1989): $X = -1$, which corresponds to the “checkerboard” zone-boundary point $\mathbf{Q} = (\pi, \pi, \pi, \dots)$; $X = 1$, which corresponds to the uniform zone-center point $\mathbf{q} = 0$; and $X = 0$, which corresponds to a general momentum vector in the Brillouin zone [since the value of the cosine will look like a random number for a general wave vector and the summation will grow like \sqrt{d} , implying $X \rightarrow 0$; only a set of measure zero of momenta have $X(\mathbf{q}) \neq 0$]. The results for $\chi_n^{cc0}(\mathbf{q})$ and $\eta_n(\mathbf{q})$ appear in Table II for the hypercubic lattice. Both the uniform ($X = 1$) and the “checkerboard” ($X = -1$) susceptibilities can be defined for the Bethe lattice, but there does not seem to be any simple way to extend the definition to all X . Indeed, higher-period ordered phases on the Bethe lattice seem to have first-order (discontinuous) phase transitions (Gruber *et al.*, 2001) so such a generalization is not needed.

We will find that near half filling, the $X = -1$ charge susceptibility diverges and far away from half filling the $X = 1$ charge susceptibility diverges. The $X = 0$ susceptibility never diverges at finite T . This is also true for the spin and pair-field susceptibilities. They are always finite at finite T . One can easily understand why the spin susceptibility does not diverge—it arises simply from the fact that the spins are independent of each other and do not interact. Similarly, one can understand why the pair-field susceptibility does not diverge—Anderson's theorem (Anderson, 1959; Bergmann and Rainer, 1974) states that one cannot have superconductivity with a static electron-electron interaction; the interaction must be dynamic.

Since the ($X = -1$) “checkerboard” charge susceptibility diverges, we can also examine the ordered state (Brandt and Mielsch, 1990). In this case, we have a charge-density wave, with different electronic densities on each of the two sublattices of the bipartite lattice. Hence both $G_{n\sigma}^A$ ($G_{n\sigma}^B$) and $\Sigma_{n\sigma}^A$ ($\Sigma_{n\sigma}^B$) are different on the two sublattices. Evaluating the momentum-dependent Green's functions yields

TABLE I Static charge, spin, and pair-field susceptibilities for the Falicov-Kimball model. The charge susceptibility is given for the general case, the spin susceptibility for spin-one-half (and only $\mathbf{q}=0$ for the ff spin susceptibility), and the pair-field susceptibility only for spin-one-half in the cc channel. Note that the cf charge susceptibility is equal to $\gamma(\mathbf{q})$.

Charge	$\chi^{cc}(\mathbf{q}) = -T \sum_{n=-\infty}^{\infty} \frac{[1+G_n(2\Sigma_n-U)-\gamma(\mathbf{q})U]G_n^2}{[1+G_n(2\Sigma_n-U)]G_n\eta_n(\mathbf{q})+(1+G_n\Sigma_n)[1+G_n(\Sigma_n-U)]}$ $\chi^{cf}(\mathbf{q}) = \gamma(\mathbf{q})$ $= \frac{\sum_{n=-\infty}^{\infty} (2s+1)w_1(1-w_1)UG_n^2/\{[1+G_n(2\Sigma_n-U)]G_n\eta_n(\mathbf{q})+(1+G_n\Sigma_n)[1+G_n(\Sigma_n-U)]\}}{1-\sum_{n=-\infty}^{\infty} (2s+1)w_1(1-w_1)U^2G_n^3\eta_n(\mathbf{q})/(1+G_n\Sigma_n)[1+G_n(\Sigma_n-U)]\{[1+G_n(2\Sigma_n-U)]G_n\eta_n(\mathbf{q})+(1+G_n\Sigma_n)[1+G_n(\Sigma_n-U)]\}}$ $\chi^{ff}(\mathbf{q}) = \frac{w_1(1-w_1)/T}{1-\sum_{n=-\infty}^{\infty} (2s+1)w_1(1-w_1)U^2G_n^3\eta_n(\mathbf{q})/(1+G_n\Sigma_n)[1+G_n(\Sigma_n-U)]\{[1+G_n(2\Sigma_n-U)]G_n\eta_n(\mathbf{q})+(1+G_n\Sigma_n)[1+G_n(\Sigma_n-U)]\}}$
Spin	$\chi'^{cc}(\mathbf{q}) = -T \sum_{n=-\infty}^{\infty} \frac{G_n^2[1+G_n(2\Sigma_n-U)]}{[1+G_n(2\Sigma_n-U)]G_n\eta_n(\mathbf{q})+(1+G_n\Sigma_n)[1+G_n(\Sigma_n-U)]}$ $\chi'^{cf}(\mathbf{q}) = 0$ $\chi'^{ff}(\mathbf{q}=0) = w_1/2T$
Pair-field	$\bar{\chi}^{cc}(\mathbf{q}) = T \sum_{n=-\infty}^{\infty} \bar{\chi}_n^{cc0}(\mathbf{q}) \left\{ 1 - \frac{w_1(1-w_1)U^2 1+G_n\Sigma_n ^2 1+G_n(\Sigma_n-U) ^2}{ 1+G_n(\Sigma_n-[1-w_1]U) ^2[(1-w_1) 1+G_n(\Sigma_n-U)]^2+w_1 1+G_n\Sigma_n ^2} \right\}$

TABLE II Values of $\chi_n^{cc0}(\mathbf{q})$ and $\eta_n(\mathbf{q})$ for the special X points 1, 0, and -1 on the hypercubic lattice.

$X(\mathbf{q})$	$\chi_n^{cc0}(\mathbf{q})$	$\eta_n(\mathbf{q})$
-1	$-G_n/(i\omega_n + \mu - \Sigma_n)$	λ_n
0	$-G_n^2$	0
1	$2[1 - (i\omega_n + \mu - \Sigma_n)G_n]$	$-\frac{1}{G_n} + \frac{1}{2\lambda_n}$

The algorithm to solve for the Green's functions is modified to the following: (i) start with a guess for $\Sigma_{n\sigma}^A$ and $\Sigma_{n\sigma}^B$ (or set both to zero); (ii) evaluate Eq. (62) to find $G_{n\sigma}^A$ and then determine $G_{0\sigma}^A(i\omega_n)$ from Eq. (31) evaluated on the A sublattice [$\Sigma_{n\sigma}^A = \{G_{0\sigma}^A(i\omega_n)\}^{-1} - (G_{n\sigma}^A)^{-1}$]; (iii) determine w_0^A and w_1^A from the appropriate A-sublattice generalization of Eq. (28); (iv) evaluate Eq. (30) on the A-sublattice to find $G_{n\sigma}^A$ and Eq. (31) to find $\Sigma_{n\sigma}^A$; (v) now find $G_{n\sigma}^B$ from Eq. (62) and $G_{0\sigma}^B(i\omega_n)$ from Eq. (31); (vi) determine w_0^B and w_1^B from Eq. (28) on the B-sublattice; and (vii) evaluate Eq. (30) on the B-sublattice to find $G_{n\sigma}^B$ and Eq. (31) to find $\Sigma_{n\sigma}^B$. Now repeat (ii–vii) until convergence is reached. We will need to adjust $E_f - \mu_f$ until $(w_1^A + w_1^B)/2 = w_1$. The calculations are then finished and the order parameter is $(w_1^A - w_1^B)/2$. A similar generalization can be employed for the static Holstein model (Ciuchi and de Pasquale, 1999). Since the skeleton expansion for the self energy in terms of the local Green's function is unknown for the static Holstein model (and hence it is not obvious how to determine Γ), this is the most direct way to search for the ordered checkerboard phase.

D. Dynamical Charge Susceptibility

We now examine the dynamical charge susceptibility (Freericks and Miller, 2000; Shvaika, 2000, 2001), defined by

$$\chi^{cc}(\mathbf{q}, i\nu_l) = \frac{1}{2s+1} \int_0^\beta d\tau e^{i\nu_l\tau} \frac{1}{V} \sum_{\mathbf{R}_i-\mathbf{R}_j} e^{\mathbf{q}\cdot(\mathbf{R}_i-\mathbf{R}_j)} \times \left[\text{Tr}_{cf} \frac{\langle e^{-\beta\mathcal{H}} n_i^c(\tau) n_j^c(0) \rangle}{\mathcal{Z}_L} - \text{Tr}_{cf} \frac{\langle e^{-\beta\mathcal{H}} n_i^c \rangle}{\mathcal{Z}_L} \text{Tr}_{cf} \frac{\langle e^{-\beta\mathcal{H}} n_j^c \rangle}{\mathcal{Z}_L} \right], \quad (63)$$

with $i\nu_l = 2i\pi l/T$ the bosonic Matsubara frequency. Once again we assume we are in zero magnetic field $H = 0$ and the f -electron site-energy is η -independent $E_{f\eta} = E_f$. Our analysis follows the path-integral approach—one can also employ a strong-coupling perturbation theory to derive these formulae (Shvaika, 2000, 2001). The dynamical susceptibilities of the FK model have some subtle properties to them that arise from the fact that the local f -electron number is conserved. In particular, the isothermal susceptibilities (calculated by adding an external field to the system, and determining how it modifies the system in the limit where the field vanishes) and the so-called isolated (Kubo) susceptibilities [which assume the system starts in equilibrium at zero field,

then is removed from the thermal bath (isolated) and the field is turned on slowly] differ from each other (the response of the isolated system to the field is the isolated susceptibility) due to the conserved nature of the f -electrons (Shvaika, 2001; Wilcox, 1968). In particular, the isolated susceptibility vanishes for the ff and mixed cf susceptibilities [due to the fact that the local f -electron number is conserved (*i.e.*, $[\mathcal{H}, n_i^f] = 0$)], but is nonzero for the cc susceptibility. The divergence of the static charge susceptibility arises entirely from the coupling between the itinerant and localized electronic systems; the pure itinerant electron response (isolated susceptibility) never diverges. Hence the isothermal susceptibility is discontinuous at zero frequency (*i.e.*, it is not analytic). The continuous (analytic) susceptibility is the isolated susceptibility, and we will spend our time discussing it for the conduction electrons.

If we express the susceptibility as a matrix in Matsubara frequency space, we find the following Dyson equation:

$$\begin{aligned} & \chi^{cc}(\mathbf{q}, i\omega_m, i\omega_n; i\nu_l) \\ &= \chi^{cc0}(\mathbf{q}, i\omega_m; i\nu_l)\delta_{mn} - T \sum_{n'} \chi^{cc0}(\mathbf{q}, i\omega_m; i\nu_l) \\ & \times \Gamma(i\omega_m, i\omega_{n'}; i\nu_l)\chi^{cc}(\mathbf{q}, i\omega_{n'}, i\omega_n; i\nu_l), \end{aligned} \quad (64)$$

and the susceptibility is found by summing over the Matsubara frequencies $\chi^{cc}(\mathbf{q}, i\nu_l) = T \sum_{mn} \chi^{cc}(\mathbf{q}, i\omega_m, i\omega_n; i\nu_l)$. Once again, the bare susceptibility depends only on the momentum parameter X , and takes the form

$$\begin{aligned} \chi^{cc0}(X, i\omega_m; i\nu_l) &= -\frac{1}{2s+1} \sum_{\mathbf{k}\sigma} G_{m\sigma}(\mathbf{k})G_{m+l\sigma}(\mathbf{k}+\mathbf{q}) \\ &= -\frac{1}{\sqrt{1-X^2}} \int_{-\infty}^{\infty} d\epsilon \frac{\rho(\epsilon)}{i\omega_m + \mu - \Sigma_m - \epsilon} \\ & \times F_{\infty} \left[\frac{i\omega_{m+l} + \mu - \Sigma_{m+l} - X\epsilon}{\sqrt{1-X^2}} \right], \end{aligned} \quad (65)$$

which reduces to our static results for $l = 0$. The bare dynamical susceptibility simplifies in three cases that are summarized in Table III. Note that one needs to evaluate χ^{cc0} with l'Hôpital's rule whenever the denominator vanishes and we dropped the spin subscripts in the Table. The irreducible charge vertex is calculated for the impurity, and it satisfies

$$\Gamma(i\omega_m, i\omega_n; i\nu_l) = \frac{1}{2s+1} \sum_{\sigma} \frac{1}{T} \frac{\delta \Sigma_{\sigma}(i\omega_m, i\omega_{m+l})}{\delta G_{\sigma}(i\omega_n, i\omega_{n+l})}, \quad (66)$$

where we now have both a self energy and a Green's function that depend on *two* Matsubara frequencies, because these functions are not time-translation-invariant in imaginary time. This occurs because we need to add a time-dependent charge field $-\int_0^{\beta} d\tau \chi(\tau) \sum_{\sigma} c_{\sigma}^{\dagger}(\tau) c_{\sigma}(\tau)$ to the action in order to evaluate the dynamic charge susceptibility and this time-dependent field removes time-translation invariance from the system (it does not depend on the time difference of the arguments of the fermionic variables).

TABLE III Values of $\chi^{cc0}(X, i\omega_m; i\nu_l)$ for the special X points 1, 0, and -1 on the hypercubic lattice.

$X(\mathbf{q})$	$\chi^{cc0}(X, i\omega_m; i\nu_l)$
-1	$-(G_m + G_{m+l})/(i\omega_m + i\omega_{m+l} + 2\mu - \Sigma_m - \Sigma_{m+l})$
0	$-G_m G_{m+l}$
1	$-(G_m - G_{m+l})/(i\nu_l + \Sigma_m - \Sigma_{m+l})$

It is not easy to perform calculations for Green's functions that depend on two time variables. The original work by Brandt and Urbanek (1992) illustrates how to proceed. We start with the definition of an auxiliary Green's function

$$g_{\sigma}^{aux}(\tau, \tau') = -\frac{\text{Tr}_c \mathcal{T}_{\tau} \left\langle e^{-\beta \mathcal{H}_0} \exp \left[\sum_{\bar{\sigma}} \int_0^{\beta} d\bar{\tau} \chi(\bar{\tau}) c_{\bar{\sigma}}^{\dagger}(\bar{\tau}) c_{\bar{\sigma}}(\bar{\tau}) \right] c_{\sigma}(\tau) c_{\sigma}^{\dagger}(\tau') \right\rangle}{\left\{ 1 + e^{\beta \mu} \exp \left[\int_0^{\beta} d\bar{\tau} \chi(\bar{\tau}) \right] \right\}^{2s+1}}, \quad (67)$$

where $\mathcal{H}_0 = -\mu \sum_{\sigma} c_{\sigma}^{\dagger} c_{\sigma}$ and the time-dependence is with respect to \mathcal{H}_0 [the auxiliary time-dependent field $\chi(\tau) = \sum_l \chi(i\nu_l) \exp(-i\nu_l \tau)$ should not be confused with any susceptibility]. It is easy to show that this auxiliary Green's function is antiperiodic with respect to either τ variable being increased by β . Hence, we can perform a double Fourier transform to yield

$$g_{\sigma}^{aux}(i\omega_m, i\omega_n)$$

$$= T \int_0^{\beta} d\tau \int_{-\beta+\tau}^{\tau} d\tau' e^{i\omega_m \tau} g_{\sigma}^{aux}(\tau, \tau') e^{-i\omega_n \tau'}, \quad (68)$$

and this is the same Matsubara-frequency dependence as in Eq. (66). Substituting in the fermionic Grassman variables from Eq. (13) and restricting ourselves to χ fields that satisfy $\chi(i\nu_0) = 0$ produces the following path-integral form for the auxiliary Green's function:

$$g_{\sigma}^{aux}(i\omega_m, i\omega_n) = -\frac{T}{\mathcal{Z}^{aux}} \int \mathcal{D}\bar{\psi} \mathcal{D}\psi \psi_{m\sigma} \bar{\psi}_{n\sigma}$$

$$\times \exp \left[T \sum_{m'n'} \sum_{\sigma'} \{ (i\omega_{m'} + \mu) \delta_{m'n'} \right. \\ \left. + \chi(i\omega_{n'} - i\omega_{m'}) \} \bar{\psi}_{n'\sigma'} \psi_{m'\sigma'} \right], \quad (69)$$

where $\mathcal{Z}^{aux} = [1 + e^{\beta\mu}]^{2s+1}$ is the auxiliary partition function for $\chi(i\nu_0) = 0$. We calculate the Green's function by adding an infinitesimal field $T\bar{\chi}_{mn\sigma}\bar{\psi}_{n\sigma}\psi_{m\sigma}$ and noting that $g_{\sigma}^{aux}(i\omega_m, i\omega_n) = \partial \ln \mathcal{Z}^{aux} / \partial \bar{\chi}_{mn\sigma}$. We will restrict our discussion to the case where *only one* Fourier component $\chi(i\nu_l)$ is nonzero. The matrix then has a nonzero diagonal, and one nonzero off-diagonal, whose elements are all equal to $\chi(i\nu_l)$. Now the partition function is the determinant of the matrix that appears in the action of Eq. (69), which assumes the simple form of the product of all diagonal elements (multiplied by a constant to assure the correct limiting behavior)

$$\mathcal{Z}^{aux} = \left[2e^{\beta\mu/2} \prod_{n=-\infty}^{\infty} \frac{i\omega_n + \mu}{i\omega_n} \right]^{2s+1}. \quad (70)$$

When we add the extra field $\bar{\chi}_{\sigma}$ to the action, the eigenvalues of the matrix change only for $m = n$, $m + l = n$, and the σ value of the $\bar{\chi}_{\sigma}$ field. The former case is the diagonal matrix element, which is simply shifted by $\bar{\chi}_{mm\sigma}$. The shift in the latter case can be worked out via perturbation theory to lowest order in $\bar{\chi}$. We find the m th and $m + l$ th eigenvalues change to $i\omega_m + \mu - \bar{\chi}_{m+lm}\chi(i\nu_l)/i\nu_l$ and $i\omega_{m+l} + \mu + \bar{\chi}_{m+lm}\chi(i\nu_l)/i\nu_l$, respectively. Taking the relevant derivatives to calculate the auxiliary Green's function, then yields

$$g_{\sigma}^{aux}(i\omega_m, i\omega_n) = \frac{\delta_{mn}}{i\omega_m + \mu} + \frac{\delta_{m+ln}\chi(i\nu_l)}{i\nu_l} \\ \times \left(\frac{1}{i\omega_{m+l} + \mu} - \frac{1}{i\omega_m + \mu} \right). \quad (71)$$

As before, we define G_0 by adding a λ_{σ} field to the action in Eq. (69) $T\lambda_{n\sigma}\bar{\psi}_{n\sigma}\psi_{n\sigma}$ (and change the partition function normalization accordingly). It is easy to show (Brandt and Urbanek, 1992; Zlatić *et al.*, 2001) that due to the fact that one can write the partition function of a path integral with a quadratic action as $\mathcal{Z} = \det g^{-1}$, with g the corresponding Green's function, one discovers

$$G_0^{-1} = [g^{aux}]^{-1} - \lambda \mathbb{1}. \quad (72)$$

The full Green's function involves an additional trace over f -states. The "itinerant-electron" piece of the impurity Hamiltonian equals $-\mu \sum_{\sigma} c_{\sigma}^{\dagger} c_{\sigma}$ when $n^f = 0$ and equals $(U - \mu) \sum_{\sigma} c_{\sigma}^{\dagger} c_{\sigma}$ when $n^f = 1$. It is a straightforward exercise to then show that

$$G_{\sigma}(i\omega_m, i\omega_n) = w_0 G_{0\sigma}(i\omega_m, i\omega_n) + w_1 [G_{0\sigma}^{-1} - U \mathbb{1}]_{mn}^{-1}, \quad (73)$$

with w_0 given by Eq. (28) for $H = 0$ and $w_1 = 1 - w_0$. Note that all of the Green's functions in Eq. (73) are

matrices, and the -1 superscript denotes the inverse of the corresponding matrix.

Eq. (73) can be rearranged by multiplying on the left or the right by matrices like G^{-1} , G_0^{-1} , and $G_0^{-1} - U$ to produce the following two matrix equations (with matrix indices and spin indices suppressed)

$$G_0^{-2} - (U + G^{-1})G_0^{-1} + (1 - w_1)UG^{-1} = 0, \quad (74)$$

$$G_0^{-2} - G_0^{-1}(U + G^{-1}) + (1 - w_1)UG^{-1} = 0. \quad (75)$$

Adding these two equations together and collecting terms results in

$$\left[G_0^{-1} - \frac{1}{2}(U + G^{-1}) \right]^2 - \frac{1}{4}(U + G^{-1})^2 + (1 - w_1)UG^{-1} = 0. \quad (76)$$

Now we substitute the matrix self energy Σ for G_0 , with the self energy defined by Dyson's equation

$$\Sigma(i\omega_m, i\omega_n) = [G_0^{-1}]_{mn} - [G^{-1}]_{mn}, \quad (77)$$

to yield a matrix quadratic equation

$$\left[\Sigma + \frac{1}{2}(G^{-1} - U) \right]^2 = \frac{1}{4}[U^2 + 2(2w_1 - 1)UG^{-1} + G^{-2}], \quad (78)$$

that relates the self energy to the Green's function. In the case where only one Fourier component $l \neq 0$ of χ is nonzero, both the self energy and the Green's function are nonzero on the diagonal $m = n$ and on the diagonal shifted by l units $m + l = n$. Substituting into the quadratic equation, and solving for the shifted diagonal component of the self-energy [to first order in $\chi(i\nu_l)$] yields the amazingly simple result

$$\Sigma(i\omega_m, i\omega_{m+l}) = G(i\omega_m, i\omega_{m+l}) \frac{\Sigma_m - \Sigma_{m+l}}{G_m - G_{m+l}}, \quad (79)$$

after some tedious algebra. In Eq. (79), the symbols Σ_m and G_m denote the diagonal components of the self energy and the Green's function, respectively, which are equal to the results we already calculated for the self energy and Green's function when $\chi(i\nu_l) = 0$.

We can now calculate the irreducible dynamical charge vertex from Eq. (66), which yields

$$\Gamma(i\omega_m, i\omega_n; i\nu_l \neq 0) = \delta_{mn} \frac{1}{T} \frac{\Sigma_m - \Sigma_{m+l}}{G_m - G_{m+l}}. \quad (80)$$

The dynamical charge vertex is then a relatively simple object for $l \neq 0$ [the static vertex is much more complicated, as can be inferred from Eqs. (48), (49), and (52)]. The original derivation, based on the atomic limit (Shvaika, 2000, 2001), produced a much more complicated looking result for the vertex, but some tedious algebra shows that the two forms are indeed identical (Freericks and Miller, 2000). Using this result for the

vertex, we immediately derive the final form for the dynamical charge susceptibility on the imaginary axis

$$\chi^{cc}(X; i\nu_{l \neq 0}) = T \sum_m \frac{\chi^{cc0}(X, i\omega_m; i\nu_l)}{1 + \chi^{cc0}(X, i\omega_m; i\nu_l) \frac{\Sigma_m - \Sigma_{m+l}}{G_m - G_{m+l}}}. \quad (81)$$

Note, that if we evaluate the uniform, dynamical charge susceptibility $\mathbf{q} = \mathbf{0}$ ($X = 1$), we find

$$\chi^{cc}(X = 1, i\nu_{l \neq 0}) = -T \sum_m \frac{G_m - G_{m+l}}{i\nu_l} = 0, \quad (82)$$

which is what we expect, because the total conduction electron charge commutes with the Hamiltonian, and hence has no τ -dependence, implying only the static response can be nonzero. Note that $\chi^{cc0}(X = 1) \neq 0$, the vertex corrections are needed to produce a vanishing total susceptibility.

In general, one is interested in the dynamical charge response on the real axis. To find the real (dynamical) response, we need to perform an analytical continuation of Eq. (81) to the real axis. Since the isothermal susceptibility is discontinuous at $\nu_l = 0$, we can perform the analytic continuation only for the isolated susceptibility. The procedure is straightforward: we divide the complex plane into regions where the Green's functions, self energies, and susceptibilities are all analytic, and we express the Matsubara summations as contour integrals over the poles of the Fermi-Dirac distribution function. Then, under the assumption that there are no poles in the integrands other than those determined by the fermi factors, we deform the contours until they are parallel to the real axis. After replacing any fermi factors of the form $f(\omega + i\nu_l)$ by $f(\omega)$, we can make the analytic continuation $i\nu_l \rightarrow \nu + i0^+$. The final expressions are straightforward, but cumbersome. We summarize them for $X = -1$ and $X = 0$ in Table IV. Only the $X = -1$ result is meaningful for the Bethe lattice. Note that one could just as easily calculate the incommensurate dynamical charge response, but the equations become significantly more complicated. We will calculate a similar result when we examine inelastic X-ray scattering below.

One can test the accuracy of the analytic continuation by employing the spectral formula for the dynamical charge susceptibility and calculating the charge susceptibility at each of the bosonic Matsubara frequencies. Comparing the spectral form with the result found directly from Eq. (81) is a stringent self-consistency test. In most calculations, these two forms agree to at least one part in a thousand.

E. Static and Dynamical Transport

Some of the most important many-body correlation functions to determine are the correlation functions related to transport properties via their corresponding Kubo formulas (Greenwood, 1958; Kubo, 1957). Transport can also be solved exactly in the FK model, and we

illustrate here how to determine the optical conductivity, the thermopower, the thermal conductivity, and the response to inelastic light scattering.

The Kubo formula relates the response function to the corresponding current-current correlation functions. Before we discuss how to calculate such correlation functions, it makes sense to describe the different transport currents that we consider. Each current (except the heat current) takes the generic form

$$j_a(\mathbf{q}) = \sum_{\sigma=1}^{2s+1} \sum_{\mathbf{k}} \gamma_a(\mathbf{k} + \mathbf{q}/2) c_{\mathbf{k}+\mathbf{q}\sigma}^\dagger c_{\mathbf{k}\sigma}, \quad (83)$$

with $\gamma_a(\mathbf{k})$ the corresponding current vertex function. The heat-current operator takes the form

$$j_Q(0) = \sum_{\sigma=1}^{2s+1} \left\{ \sum_{\mathbf{k}} \gamma_Q(\mathbf{k}) c_{\mathbf{k}\sigma}^\dagger c_{\mathbf{k}\sigma} + \sum_{\mathbf{k}\mathbf{k}'} \bar{\gamma}_Q(\mathbf{k}, \mathbf{k}') c_{\mathbf{k}\sigma}^\dagger c_{\mathbf{k}'\sigma} \right\} \quad (84)$$

with $\gamma_Q(\mathbf{k})$ the vertex that arises from the kinetic energy and $\bar{\gamma}_Q(\mathbf{k}, \mathbf{k}')$ the vertex from the potential energy. For conventional charge, and thermal transport, we are interested only in the $\mathbf{q} \rightarrow 0$ (uniform) limit of the current operators, but the finite- \mathbf{q} dependence is important for inelastic (Raman) scattering of X-ray light. The current vertex functions are summarized in Table V.

The Dyson equation for any current-current correlation function takes the form shown in Fig. 2, which is similar to that given by Eq. (64), but the bare and interacting susceptibilities are now different due to the corresponding γ_a factors. Note that there are two coupled equations illustrated in Figs. 2 (a) and (b); these equations differ by the number of γ_a factors in them (of course, there is only one equation when $\gamma_a = 1$ as we saw for the dynamical charge susceptibility). Note further, that one could evaluate mixed current-current correlation functions where there is a γ_a on the left vertex and a γ_b on the right vertex, but we don't describe that case in detail here. The irreducible vertex function Γ is the dynamical charge vertex of Eq. (80) which has the full symmetry of the lattice. If the vertex factor γ_a does not have a projection onto the full symmetry of the lattice, then there are no vertex corrections from the local dynamical charge vertex (Khurana, 1990). This occurs whenever

$$\sum_{\mathbf{k}} \gamma_a(\mathbf{k} + \frac{\mathbf{q}}{2}) G_{n\sigma}(\mathbf{k}) G_{n+l\sigma}(\mathbf{k} + \mathbf{q}) = 0. \quad (85)$$

If Eq. (85) is satisfied, then the corresponding current-current correlation function is given by the bare bubble depicted by the first diagram on the right-hand-side of Fig. 2 (a).

One case where there are no vertex corrections is the optical conductivity, which is constructed from a $\mathbf{q} = 0$ current-current correlation function. We consider the case where the only effect of the magnetic field is from the Zeeman splitting of the states (which is accurate in large

TABLE IV Dynamical charge susceptibility on the real axis for $X = -1$ and $X = 0$ (the dynamical susceptibility vanishes for $X = 1$).

X	Dynamical susceptibility $\chi^{cc}(X, \nu)$
-1	$\frac{i}{2\pi} \int_{-\infty}^{\infty} d\omega \left\{ \begin{aligned} & f(\omega) \frac{[G(\omega) + G(\omega + \nu)] / [2\omega + 2\mu + \nu + \Sigma(\omega) - \Sigma(\omega + \nu)]}{1 - [G(\omega) + G(\omega + \nu)][\Sigma(\omega) - \Sigma(\omega + \nu)] / [2\omega + 2\mu + \nu + \Sigma(\omega) - \Sigma(\omega + \nu)][G(\omega) - G(\omega + \nu)]} \\ & - f(\omega + \nu) \frac{[G^*(\omega) + G^*(\omega + \nu)] / [2\omega + 2\mu + \nu + \Sigma^*(\omega) - \Sigma^*(\omega + \nu)]}{1 - [G^*(\omega) + G^*(\omega + \nu)][\Sigma^*(\omega) - \Sigma^*(\omega + \nu)] / [2\omega + 2\mu + \nu + \Sigma^*(\omega) - \Sigma^*(\omega + \nu)][G^*(\omega) - G^*(\omega + \nu)]} \\ & - [f(\omega) - f(\omega + \nu)] \frac{[G^*(\omega) + G(\omega + \nu)] / [2\omega + 2\mu + \nu + \Sigma^*(\omega) - \Sigma(\omega + \nu)]}{1 - [G^*(\omega) + G(\omega + \nu)][\Sigma^*(\omega) - \Sigma(\omega + \nu)] / [2\omega + 2\mu + \nu + \Sigma^*(\omega) - \Sigma(\omega + \nu)][G^*(\omega) - G(\omega + \nu)]} \end{aligned} \right\}$
0	$\frac{i}{2\pi} \int_{-\infty}^{\infty} d\omega \left\{ \begin{aligned} & f(\omega) \frac{G(\omega)G(\omega + \nu)}{1 - G(\omega)G(\omega + \nu)[\Sigma(\omega) - \Sigma(\omega + \nu)] / [(G(\omega) - G(\omega + \nu))]} - f(\omega + \nu) \frac{G^*(\omega)G^*(\omega + \nu)}{1 - G^*(\omega)G^*(\omega + \nu)[\Sigma^*(\omega) - \Sigma^*(\omega + \nu)] / [(G^*(\omega) - G^*(\omega + \nu))]} \\ & - [f(\omega) - f(\omega + \nu)] \frac{G^*(\omega)G(\omega + \nu)}{1 - G^*(\omega)G(\omega + \nu)[\Sigma^*(\omega) - \Sigma(\omega + \nu)] / [(G^*(\omega) - G(\omega + \nu))]} \end{aligned} \right\}$

TABLE V Current vertex functions for use in Eqs. (83) and (84). The symbols e_α^I and e_α^O are the polarization vectors for the incident and outgoing light, respectively, and a denotes the lattice spacing. An overall factor depending on properties of the incident and outgoing light is neglected for the inelastic light scattering vertex.

Current type	vertex function $\gamma_a(\mathbf{k})$
Charge	$\gamma_n(\mathbf{k}) = iea\nabla\epsilon(\mathbf{k})/\hbar$
Heat	$\gamma_Q(\mathbf{k}) = ia\nabla\epsilon(\mathbf{k})[\epsilon(\mathbf{k}) - \mu]/\hbar$ $\bar{\gamma}_Q(\mathbf{k}, \mathbf{k}') = iaU[\nabla\epsilon(\mathbf{k}) + \nabla\epsilon(\mathbf{k}')]W(\mathbf{k} - \mathbf{k}')/2\hbar$ $W(\mathbf{k}) = \sum_j \exp(-i\mathbf{k} \cdot \mathbf{R}_j) \sum_\eta f_{j\eta}^\dagger f_{j\eta} / V$
Inelastic light scattering	$\gamma_L(\mathbf{k}) = \sum_{\alpha\beta} e_\alpha^I \frac{\partial^2 \epsilon(\mathbf{k})}{\partial \mathbf{k}_\alpha \partial \mathbf{k}_\beta} e_\beta^{O*}$

dimensions, because the phase factors induced in the hopping matrix occurs only in one dimension). We illustrate here how to calculate the optical conductivity on the hypercubic lattice (Moeller *et al.*, 1992; Pruschke *et al.*, 1993a,b, 1995). The starting point is the current-current correlation function on the imaginary lattice, which is equal to the bare bubble diagram in Fig. 2 (a)

$$\chi^{nn}(i\nu_l) = \frac{e^2}{da^{d-2}\hbar^2} \sum_\sigma \sum_n \sum_{\mathbf{k}} \sin^2(\mathbf{k}_1) G_{n\sigma}(\mathbf{k}) G_{n+l\sigma}(\mathbf{k}), \quad (86)$$

where we have chosen the 1 direction for the velocity operator and the n superscript denotes the particle-number (charge) current operator (note our energy unit t^* equals 1 so it is suppressed). The average of $\sin^2(\mathbf{k}_1)$ (times a function of $\epsilon_{\mathbf{k}}$) is equal to 1/2 times the integral over ϵ of the function times the density of states. Hence, the current-current correlation function becomes

$$\chi^{nn}(i\nu_l) = \frac{e^2}{2da^{d-2}\hbar^2} \sum_{\sigma=1}^{2s+1} \sum_{n=-\infty}^{\infty} \int_{-\infty}^{\infty} d\epsilon \rho(\epsilon) \times \frac{1}{i\omega_n + \mu + g\mu_B H m_\sigma - \Sigma_{n\sigma} - \epsilon}$$

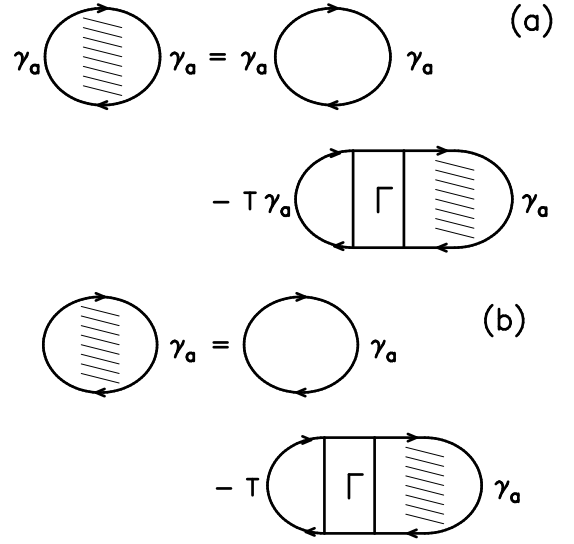


FIG. 2 Coupled Dyson equations for current-current correlation functions described by the vertex function γ_a . Panel (a) depicts the Dyson equation for the interacting correlation function, while panel (b) is the supplemental equation needed to solve for the correlation function. The symbol Γ stands for the local dynamical irreducible charge vertex given in Eq. (80). In situations where Eq. (85) is satisfied, there are no charge vertex corrections, and the correlation function is simply given by the first diagram on the right hand side of panel (a).

$$\times \frac{1}{i\omega_{n+l} + \mu + g\mu_B H m_\sigma - \Sigma_{n+l\sigma} - \epsilon}. \quad (87)$$

Note that the optical conductivity is a $1/d$ correction. The analytic continuation is performed in the same fashion as was done for the dynamic charge susceptibility. The optical conductivity is defined to be $\sigma(\omega) = \text{Im}\chi^{nn}(\nu)/\nu$, so the final result is

$$\sigma(\nu) = \sigma_0 \sum_{\sigma=1}^{2s+1} \int_{-\infty}^{\infty} d\epsilon \rho(\epsilon) \int_{-\infty}^{\infty} d\omega A_\sigma(\epsilon, \omega) A_\sigma(\epsilon, \omega + \nu)$$

$$\times \frac{f(\omega) - f(\omega + \nu)}{\nu}, \quad (88)$$

with $\sigma_0 = e^2\pi^2/hda^{d-2}$ (which is approximately $4.3 \times 10^3 \Omega^{-1}\text{-cm}^{-1}$ in $d = 3$ with $a \approx 3 \times 10^{-8}$ cm). Note that one factor of \hbar is needed to construct the dimensionless energy unit when multiplied by ν in the denominator, which is why only one factor of h appears in σ_0 .

Eq. (88) can be simplified further by performing the integral over ϵ . This is done by using Eq. (36) to rewrite both spectral functions as an imaginary part of a Green's function, and noting that the imaginary part of z is $(z - z^*)/2i$. The integral over ϵ can then be performed after expanding each integrand by partial fractions to yield

$$\begin{aligned} \sigma(\nu) = & \frac{\sigma_0}{2\pi^2} \sum_{\sigma=1}^{2s+1} \int_{-\infty}^{\infty} d\omega \text{Re} \left\{ \frac{G_{\sigma}(\omega) - G_{\sigma}^*(\omega + \nu)}{\nu + \Sigma_{\sigma}(\omega) - \Sigma_{\sigma}^*(\omega + \nu)} \right. \\ & \left. - \frac{G_{\sigma}(\omega) - G_{\sigma}(\omega + \nu)}{\nu + \Sigma_{\sigma}(\omega) - \Sigma_{\sigma}(\omega + \nu)} \right\} \frac{f(\omega) - f(\omega + \nu)}{\nu} \end{aligned} \quad (89)$$

On another lattice, the optical conductivity takes the form of Eq. (88) but with an extra factor of $v^2(\epsilon)$. Enforcing the optical sum rule (which relates the integral of the optical conductivity to the average kinetic energy) (Chattopadhyay *et al.*, 2000; Maldague, 1977) produces a differential equation for $v^2(\epsilon)$

$$\frac{d}{d\epsilon} [v^2(\epsilon)\rho(\epsilon)] + \epsilon\rho(\epsilon) = 0, \quad (90)$$

with the boundary condition that $v^2(\epsilon) \rightarrow 0$ at the band edges (where appropriate). On the hypercubic lattice one needs to sum the optical conductivity over all d axis directions to be able to be put in the above form; solving the differential equation gives $v^2(\epsilon) = 1/2$ as expected. For the infinite coordination Bethe lattice, one finds $v^2(\epsilon) = (4 - \epsilon^2)/3$. This agrees with the conjectured result (Chung and Freericks, 1998; Velický, 1969), but it relies on enforcing the sum rule for the Bethe lattice, which has not been established independently (van Dongen and Blümer, 2002).

If we take the limit $\nu \rightarrow 0$ on the hypercubic lattice, we find

$$\sigma_{dc} = \sigma_0 \int_{-\infty}^{\infty} d\omega \left(-\frac{df(\omega)}{d\omega} \right) \sum_{\sigma=1}^{2s+1} \tau_{\sigma}(\omega), \quad (91)$$

with the spin-dependent relaxation time equal to

$$\begin{aligned} \tau_{\sigma}(\omega) = & \frac{\text{Im}G_{\sigma}(\omega)}{\text{Im}\Sigma_{\sigma}(\omega)} + 2 \\ & - 2\text{Re}\{[\omega + \mu + g\mu_B H m_{\sigma} - \Sigma_{\sigma}(\omega)]G_{\sigma}(\omega)\} \end{aligned} \quad (92)$$

In addition, one is often interested in thermal transport quantities such as the thermopower S and the electronic contribution to the thermal conductivity κ_e . These three quantities are usually expressed in terms of three different transport coefficients L_{11} , $L_{12} = L_{21}$ and L_{22} as follows:

$$\sigma_{dc} = e^2 L_{11}, \quad (93)$$

$$S = \frac{k_B}{|e|T} \frac{L_{12}}{L_{11}}, \quad (94)$$

and

$$\kappa_e = \frac{k_B^2}{T} \left[L_{22} - \frac{L_{12}L_{21}}{L_{11}} \right], \quad (95)$$

with k_B the Boltzmann constant. The individual transport coefficients are determined by the zero-frequency limit of the analytic continuation of the relevant polarization operators $L_{ij} = \lim_{\nu \rightarrow 0} \text{Re}[i\bar{L}_{ij}(\nu)/\nu]$ with

$$\bar{L}_{11}(i\nu_l) = \int_0^{\beta} d\tau e^{i\nu_l\tau} \text{Tr}_{cf} \frac{\langle \mathcal{T}_{\tau} e^{-\beta\mathcal{H}} j_n(\tau) j_n(0) \rangle}{\mathcal{Z}_L}, \quad (96)$$

$$\bar{L}_{12}(i\nu_l) = \int_0^{\beta} d\tau e^{i\nu_l\tau} \text{Tr}_{cf} \frac{\langle \mathcal{T}_{\tau} e^{-\beta\mathcal{H}} j_n(\tau) j_Q(0) \rangle}{\mathcal{Z}_L}, \quad (97)$$

and

$$\bar{L}_{22}(i\nu_l) = \int_0^{\beta} d\tau e^{i\nu_l\tau} \text{Tr}_{cf} \frac{\langle \mathcal{T}_{\tau} e^{-\beta\mathcal{H}} j_Q(\tau) j_Q(0) \rangle}{\mathcal{Z}_L}, \quad (98)$$

where the subscripts n and Q denote the number (charge) and heat currents respectively (and we suppressed the Cartesian vector indices). All of these correlation functions are determined by their corresponding bare bubbles, because there are no vertex corrections for any of them. Note that our sign convention for the thermopower is that of Ashcroft and Mermin (1976), where the coefficient multiplying L_{12}/L_{11} is positive for negatively charged carriers. This leads to the situation where electron-like transport has a positive thermopower, and hole-like transport has a negative thermopower at low temperature. (The sign of the thermopower varies depending on what convention is used for the definition of S in terms of the transport coefficients.) A theorem by Jonson and Mahan (1980, 1990) says that even in a correlated system, there is a simple relation between these different transport coefficients [that they reproduce the so-called Mott noninteracting form (Chester and Thellung, 1961)]

$$L_{ij} = \frac{\sigma_0}{e^2} \int_{-\infty}^{\infty} d\omega \left(-\frac{df(\omega)}{d\omega} \right) \sum_{\sigma=1}^{2s+1} \tau_{\sigma}(\omega) \omega^{i+j-2}. \quad (99)$$

What is remarkable, is that in the case of the FK model, one can explicitly calculate the relevant correlation functions and verify directly the Jonson-Mahan theorem (Freericks and Zlatić, 2001b, 2002a). The derivation is too long to reproduce here. Note that we have taken the more modern definitions of the L_{ij} coefficients here, which has one less power of T than the normalization used by Freericks and Zlatić (2001b, 2002a); Jonson and Mahan (1980, 1990).

The final transport property we determine is the scattering of inelastic light. When optical photons are used, this corresponds to conventional electronic Raman scattering: inelastic light scattering off of the charge excitations of the many-body system. When higher-energy (X-rays) are employed, one scatters the photon off of the momentum and frequency-dependent charge excitations of the system. The Raman scattering limit results in the limit $\mathbf{q} \rightarrow 0$. For simplicity, we consider only the spinless case, with $H = 0$.

Inelastic light scattering depends on the polarizations of the incident and outgoing light. As such, it provides some additional symmetry resolution over and above the elastic scattering of an optical conductivity measurement. There are traditionally three main symmetries considered in Raman scattering experiments: (i) A_{1g} which has the full symmetry of the lattice; (ii) B_{1g} which has a d-wave symmetry and (iii) B_{2g} which is another d-wave symmetry. Each symmetry is chosen by different polarizations for the incident and scattered light. Here we concentrate on nonresonant Raman scattering, where the vertex functions are not functions of the photon energies. If we sum over the d pairs of polarizations, where $e^I = e^O$ and each vector points along each of the different Cartesian axes, then we have the A_{1g} sector. If we choose $e^I = (1, 1, 1, \dots)$ and $e^O = (1, -1, 1, -1, \dots)$, then we have the B_{1g} sector. And if we choose $e^I = (1, 0, 1, 0, \dots)$ and $e^O = (0, -1, 0, -1, \dots)$ then we have the B_{2g} sector. If we have just nearest-neighbor hopping, then the B_{2g} response vanishes because $\gamma_{B_{2g}} = 0$. Following the form given in Table V, we find $\gamma_{A_{1g}}(\mathbf{q}) = -\epsilon(\mathbf{q})$ and $\gamma_{B_{1g}}(\mathbf{q}) = t^* \sum_{j=1}^{\infty} \cos \mathbf{q}_j (-1)^j / \sqrt{d}$.

A straightforward calculation, using Eq. (85), shows that the B_{1g} response has no vertex corrections on the zone diagonal $\mathbf{q} = (q, q, q, q, \dots)$. Hence, the zone-diagonal B_{1g} response is the bare bubble. The A_{1g} response (and the B_{1g} off of the zone diagonal), on the other hand, does have vertex corrections, and is more complicated. The calculation of each response function is straightforward, but tedious. One needs to first solve the coupled equations depicted in Fig. 2 on the imaginary axis and then perform the analytic continuation as we have done previously for other response functions. The end result is quite long and is summarized in Tables VI and VII.

It is interesting to take the limit of conventional Raman scattering with optical photons, where $\mathbf{q} \rightarrow 0$ ($X \rightarrow 1$). In this case, one finds $\chi_0 = -\int d\epsilon \rho(\epsilon) / [\omega + \mu - \Sigma(\omega) - \epsilon]$ and the B_{1g} response simplifies to

$$\begin{aligned} \chi_{B_{1g}}(\nu) &= \frac{i}{4\pi} \int_{-\infty}^{\infty} d\omega \int_{-\infty}^{\infty} d\epsilon \rho(\epsilon) \\ &\times \left\{ f(\omega) \frac{1}{\omega + \nu + \mu - \Sigma(\omega + \nu) - \epsilon} \right. \\ &\times \left. \left[\frac{1}{\omega + \mu - \Sigma(\omega) - \epsilon} - \frac{1}{\omega + \mu - \Sigma^*(\omega) - \epsilon} \right] \right\} \end{aligned}$$

$$\begin{aligned} &- f(\omega + \nu) \frac{1}{\omega + \mu - \Sigma^*(\omega) - \epsilon} \\ &\times \left[\frac{1}{\omega + \nu + \mu - \Sigma^*(\omega + \nu) - \epsilon} \right. \\ &\left. - \frac{1}{\omega + \nu + \mu - \Sigma(\omega + \nu) - \epsilon} \right] \Bigg\}. \end{aligned} \quad (100)$$

Now using the definition of the spectral function in Eq. (36), and taking the imaginary part of Eq. (100) produces the so-called Shastry-Shraiman relation (Shastry and Shraiman, 1990, 1991) which relates the imaginary part of the nonresonant B_{1g} Raman response function to the optical conductivity

$$\text{Im} \chi_{B_{1g}}(\nu) \propto \nu \sigma(\nu), \quad (101)$$

which was first proved in Freericks and Devereaux (2001b).

Another interesting limit is the $\mathbf{q} = (\pi, \pi, \pi, \dots)$ ($X = -1$) limit, where we find $\chi'_0 = \tilde{\chi}'_0 = 0$, $\tilde{\chi}_0 = \chi_0/2$, and $\tilde{\tilde{\chi}}_0 = \tilde{\chi}_0/2$. In this case, the renormalization due to the dynamical charge vertex exactly cancels in the numerator and denominator, and one finds *the same result* for the inelastic X-ray scattering in the A_{1g} and B_{1g} sectors. Hence, a polarized measurement of the inelastic X-ray scattering at the zone boundary determines the relative importance of nonlocal charge fluctuations to the strongly correlated system. This is quantified by comparing the scattering in the two different symmetry sectors; the difference in the results is a measure of the nonlocal correlations.

We have produced results for inelastic X-ray scattering only along the zone diagonal. One could choose other directions as well. In general, we find that the symmetries from different channels then mix, and both A_{1g} and B_{1g} channels are renormalized by the irreducible dynamic charge vertex. The formulas in that case are complicated and will not be presented here.

One could also study resonant (or mixed) Raman response functions. The formalism is similar to the nonresonant case, except it is better to work directly on the real axis. These calculations have not yet been completed by anyone. But a simple power-counting analysis of the different symmetry sectors can be performed (Freericks and Devereaux, 2001b). What is found is that the A_{1g} sector has contributions from the nonresonant, the mixed diagrams, and the resonant diagrams. The B_{1g} sector is either nonresonant or resonant, but the mixed contributions disappear as $1/d$. The B_{2g} response is purely resonant.

F. Single-Particle Properties (Localized Electrons)

We now study f -electron properties. Since the local f -electron number is conserved, one might believe that the localized particle dynamics are trivial. Indeed, this is true for the particle number, but the *fermionic* electron degrees of freedom are nontrivial, even if they are

TABLE VI Response functions for inelastic X-ray scattering by a photon of momentum $\mathbf{q} = (q, q, q, \dots)$ along the zone diagonal described by the parameter $X(\mathbf{q}) = \cos q$ for the A_{1g} and B_{1g} sectors. The symbols with χ_0 appear in Table VII and * denotes complex conjugation.

Scattering response function
$\chi_{A_{1g}}(\mathbf{q}, \nu) = \frac{i}{2\pi} \int_{-\infty}^{\infty} d\omega$ $\left\{ f(\omega) \frac{\bar{\chi}_0(\omega; X, \nu) + \frac{\Sigma(\omega) - \Sigma(\omega + \nu)}{G(\omega) - G(\omega + \nu)} [\chi_0(\omega; X, \nu) \bar{\chi}_0(\omega; X, \nu) - \chi_0'^2(\omega; X, \nu)]}{1 + \frac{\Sigma(\omega) - \Sigma(\omega + \nu)}{G(\omega) - G(\omega + \nu)} \chi_0(\omega; X, \nu)} - f(\omega + \nu) \frac{\bar{\chi}_0^*(\omega; X, \nu) + \frac{\Sigma^*(\omega) - \Sigma^*(\omega + \nu)}{G^*(\omega) - G^*(\omega + \nu)} [\chi_0^*(\omega; X, \nu) \bar{\chi}_0^*(\omega; X, \nu) - \chi_0'^{*2}(\omega; X, \nu)]}{1 + \frac{\Sigma^*(\omega) - \Sigma^*(\omega + \nu)}{G^*(\omega) - G^*(\omega + \nu)} \chi_0^*(\omega; X, \nu)} \right.$ $\left. - [f(\omega) - f(\omega + \nu)] \frac{\bar{\chi}_0(\omega; X, \nu) + \frac{\Sigma(\omega) - \Sigma(\omega + \nu)}{G(\omega) - G(\omega + \nu)} [\bar{\chi}_0(\omega; X, \nu) \bar{\chi}_0(\omega; X, \nu) - \bar{\chi}_0'^2(\omega; X, \nu)]}{1 + \frac{\Sigma(\omega) - \Sigma(\omega + \nu)}{G(\omega) - G(\omega + \nu)} \bar{\chi}_0(\omega; X, \nu)} \right\}$
$\chi_{B_{1g}}(\mathbf{q}, \nu) = \frac{i}{4\pi} \int_{-\infty}^{\infty} d\omega \{ f(\omega) \chi_0(\omega; X, \nu) - f(\omega + \nu) \chi_0^*(\omega; X, \nu) - [f(\omega) - f(\omega + \nu)] \bar{\chi}_0(\omega; X, \nu) \}$

TABLE VII Symbols χ_0 , χ_0' , $\bar{\chi}_0$, $\bar{\chi}_0'$, and $\tilde{\chi}_0$ that appear in Table VI

Symbol
$\chi_0(\omega; X, \nu) = - \int_{-\infty}^{\infty} d\epsilon \rho(\epsilon) \frac{1}{\omega + \mu - \Sigma(\omega) - \epsilon} \frac{1}{\sqrt{1 - X^2}} F_{\infty} \left(\frac{\omega + \nu + \mu - \Sigma(\omega + \nu) - X\epsilon}{\sqrt{1 - X^2}} \right)$
$\bar{\chi}_0(\omega; X, \nu) = - \int_{-\infty}^{\infty} d\epsilon \rho(\epsilon) \frac{1}{\omega + \mu - \Sigma^*(\omega) - \epsilon} \frac{1}{\sqrt{1 - X^2}} F_{\infty} \left(\frac{\omega + \nu + \mu - \Sigma(\omega + \nu) - X\epsilon}{\sqrt{1 - X^2}} \right)$
$\chi_0'(\omega; X, \nu) = - \sqrt{\frac{1+X}{8}} \int_{-\infty}^{\infty} d\epsilon \rho(\epsilon) \left\{ \frac{1}{[\omega + \mu - \Sigma(\omega) - \epsilon]^2} \frac{1}{\sqrt{1 - X^2}} F_{\infty} \left(\frac{\omega + \nu + \mu - \Sigma(\omega + \nu) - X\epsilon}{\sqrt{1 - X^2}} \right) \right.$ $\left. + \frac{1}{\omega + \mu - \Sigma(\omega) - \epsilon} \frac{2}{1 - X^2} \left[-1 + \frac{\omega + \nu + \mu - \Sigma(\omega + \nu)}{\sqrt{1 - X^2}} F_{\infty} \left(\frac{\omega + \nu + \mu - \Sigma(\omega + \nu) - X\epsilon}{\sqrt{1 - X^2}} \right) \right] \right\}$
$\bar{\chi}_0'(\omega; X, \nu) = - \sqrt{\frac{1+X}{8}} \int_{-\infty}^{\infty} d\epsilon \rho(\epsilon) \left\{ \frac{1}{[\omega + \mu - \Sigma^*(\omega) - \epsilon]^2} \frac{1}{\sqrt{1 - X^2}} F_{\infty} \left(\frac{\omega + \nu + \mu - \Sigma(\omega + \nu) - X\epsilon}{\sqrt{1 - X^2}} \right) \right.$ $\left. + \frac{1}{\omega + \mu - \Sigma^*(\omega) - \epsilon} \frac{2}{1 - X^2} \left[-1 + \frac{\omega + \nu + \mu - \Sigma(\omega + \nu)}{\sqrt{1 - X^2}} F_{\infty} \left(\frac{\omega + \nu + \mu - \Sigma(\omega + \nu) - X\epsilon}{\sqrt{1 - X^2}} \right) \right] \right\}$
$\bar{\chi}_0(\omega; X, \nu) = \frac{1}{2} \chi_0(\omega; X, \nu) - \frac{1+X}{4} \int_{-\infty}^{\infty} d\epsilon \rho(\epsilon) \left\{ \frac{1}{[\omega + \mu - \Sigma(\omega) - \epsilon]^3} \frac{1}{\sqrt{1 - X^2}} F_{\infty} \left(\frac{\omega + \nu + \mu - \Sigma(\omega + \nu) - X\epsilon}{\sqrt{1 - X^2}} \right) \right.$ $\left. + \frac{1}{[\omega + \mu - \Sigma(\omega) - \epsilon]^2} \frac{2}{1 - X^2} \left[-1 + \frac{\omega + \nu + \mu - \Sigma(\omega + \nu)}{\sqrt{1 - X^2}} F_{\infty} \left(\frac{\omega + \nu + \mu - \Sigma(\omega + \nu) - X\epsilon}{\sqrt{1 - X^2}} \right) \right] \right.$ $\left. + \frac{1}{\omega + \mu - \Sigma(\omega) - \epsilon} \frac{1}{(1 - X^2)^{3/2}} \left[-F_{\infty} \left(\frac{\omega + \nu + \mu - \Sigma(\omega + \nu) - X\epsilon}{\sqrt{1 - X^2}} \right) + \frac{2\{\omega + \nu - \Sigma(\omega + \nu) - X\epsilon\}}{\sqrt{1 - X^2}} \left\{ -1 + \frac{\omega + \nu + \mu - \Sigma(\omega + \nu)}{\sqrt{1 - X^2}} F_{\infty} \left(\frac{\omega + \nu + \mu - \Sigma(\omega + \nu) - X\epsilon}{\sqrt{1 - X^2}} \right) \right\} \right] \right\}$
$\tilde{\chi}_0(\omega; X, \nu) = \frac{1}{2} \bar{\chi}_0(\omega; X, \nu) - \frac{1+X}{4} \int_{-\infty}^{\infty} d\epsilon \rho(\epsilon) \left\{ \frac{1}{[\omega + \mu - \Sigma^*(\omega) - \epsilon]^3} \frac{1}{\sqrt{1 - X^2}} F_{\infty} \left(\frac{\omega + \nu + \mu - \Sigma(\omega + \nu) - X\epsilon}{\sqrt{1 - X^2}} \right) \right.$ $\left. + \frac{1}{[\omega + \mu - \Sigma^*(\omega) - \epsilon]^2} \frac{2}{1 - X^2} \left[-1 + \frac{\omega + \nu + \mu - \Sigma(\omega + \nu)}{\sqrt{1 - X^2}} F_{\infty} \left(\frac{\omega + \nu + \mu - \Sigma(\omega + \nu) - X\epsilon}{\sqrt{1 - X^2}} \right) \right] \right.$ $\left. + \frac{1}{\omega + \mu - \Sigma^*(\omega) - \epsilon} \frac{1}{(1 - X^2)^{3/2}} \left[-F_{\infty} \left(\frac{\omega + \nu + \mu - \Sigma(\omega + \nu) - X\epsilon}{\sqrt{1 - X^2}} \right) + \frac{2\{\omega + \nu - \Sigma(\omega + \nu) - X\epsilon\}}{\sqrt{1 - X^2}} \left\{ -1 + \frac{\omega + \nu + \mu - \Sigma(\omega + \nu)}{\sqrt{1 - X^2}} F_{\infty} \left(\frac{\omega + \nu + \mu - \Sigma(\omega + \nu) - X\epsilon}{\sqrt{1 - X^2}} \right) \right\} \right] \right\}$

restricted to be local. As a first step in our analysis, we can imagine writing the statistical factor for the f -occupancy in terms of an effective f -level E_f^* (Czychoł, 1999)

$$w_1 = \frac{1}{1 + \exp[-\beta(E_f^* - \mu_f)]} \quad (102)$$

which we have written explicitly for the spinless case, with suitable generalizations for higher-spin cases. Notice that in many cases, either w_1 changes as a function of T , or μ_f changes as a function of T , or both. Hence, E_f^* typically has temperature dependence. If we view this energy as the centroid of the f -spectral function, we can immediately learn about how the f -spectral function may change as a function of T . Of course one can only learn so much from a single number.

What is more interesting is to evaluate the local f -electron Green's function following the work of Brandt and Urbanek (1992) and Zlatić *et al.* (2001) [see also Janis (1994) which examined the corresponding X-ray edge problem]. The local f -electron Green's function on the imaginary axis is defined by

$$F_{\eta}(\tau) = -\text{Tr}_{cf} \frac{\langle e^{-\beta \mathcal{H}_{imp}} S(\lambda) f_{\eta}(\tau) f_{\eta}^{\dagger}(0) \rangle}{\mathcal{Z}_{imp}}, \quad (103)$$

for $\tau > 0$ in the interaction representation [\mathcal{Z}_{imp} is given by Eq. (26) with $H = 0$]. The impurity Hamiltonian in zero magnetic field is $\mathcal{H}_{imp} = -\mu n^c + \sum_{\eta} (E_{f\eta} - \mu_f) n_{\eta}^f +$

$Un^c n^f$ and the evolution operator satisfies

$$S(\lambda) = \mathcal{T}_\tau \exp \left[- \int_0^\beta d\tau \int_0^\beta d\tau' \sum_\sigma c_\sigma^\dagger(\tau) \lambda_\sigma(\tau - \tau') c_\sigma(\tau') \right], \quad (104)$$

with $\lambda_\sigma(\tau) = T \sum_n \exp(-i\omega_n \tau) \lambda_{n\sigma}$. The field $\lambda_{n\sigma}$ is the discrete function that satisfies Eqs. (27–32). Since $f_\eta(\tau) = \exp(\tau \mathcal{H}_{imp}) f_\eta(0) \exp(-\tau \mathcal{H}_{imp})$, we find

$$\frac{d}{d\tau} f_\eta(\tau) = \left[-(E_{f\eta} - \mu_f) - U \sum_\sigma c_\sigma^\dagger(\tau) c_\sigma(\tau) \right] f_\eta(\tau), \quad (105)$$

which can be integrated to yield

$$f_\eta(\tau) = e^{-(E_{f\eta} - \mu_f)\tau} \times \mathcal{T}_\tau \exp \left(-U \sum_\sigma \int_0^\tau d\tau' c_\sigma^\dagger(\tau') c_\sigma(\tau') \right) f_\eta(0). \quad (106)$$

If we define a time-dependent field

$$\chi_\tau(\tau', \tau'') = -U\theta(\tau - \tau')\delta(\tau' - \tau''), \quad (107)$$

then the f -electron Green's function becomes

$$F_\eta(\tau) = -\frac{1}{\mathcal{Z}_{imp}} e^{-(E_{f\eta} - \mu_f)\tau} \text{Tr}_c \mathcal{T}_\tau \langle e^{-\beta \mathcal{H}_0} S(\lambda - \chi_\tau) \rangle, \quad (108)$$

with $\mathcal{H}_0 = -\mu n^c$, because the trace over f states is restricted to $n^f = 0$ for $\tau > 0$ propagation [the operator $f(0)f^\dagger(0)$ projects onto $n^f = 0$ and all of the remaining operators are composed of $f^\dagger f$ pairs which do not change the total f -electron number].

The strategy for evaluating the trace over itinerant-electron states is the same as in Section II.D. The trace involves operator averages that are not time-translation invariant because the χ_τ field is not a function of $\tau' - \tau''$ only. We start with the auxiliary Green's function in Eq. (69) and note that the double Fourier transform of the χ_τ field [analogous to Eq. (68)] becomes

$$\begin{aligned} \chi_\tau(i\nu_l) &= T \int_0^\beta d\tau' e^{i\nu_l \tau'} \chi_\tau(\tau') \\ &= \begin{cases} \frac{U}{i\nu_l \beta} (1 - e^{i\nu_l \tau}), & l \neq 0; \\ -\frac{U\tau}{\beta}, & l = 0, \end{cases} \end{aligned} \quad (109)$$

where our choice for normalizing the Fourier transform has an extra factor of T for convenience here [in other words $\chi_\tau(i\nu_l)$ has dimensions of energy] and the bosonic Matsubara frequency arises from the difference of two fermionic Matsubara frequencies. Since $\chi_\tau(i\nu_0) \neq 0$, we now have $\mathcal{Z}^{aux}(-\chi_\tau) = [1 + \exp(\beta\mu - U\tau)]^{2s+1}$. The partition function can also be expressed as the determinant of the matrix that appears in the exponent in Eq. (69). In the general case, we can write the partition function as an infinite product

$$\mathcal{Z}^{aux}(-\chi_\tau) = \left[2e^{\beta(\mu + \chi_0)/2} \prod_{n=-\infty}^{\infty} \frac{i\omega_n + \mu + \chi_0}{i\omega_n} \right]^{2s+1}, \quad (110)$$

which is equal to the product of the diagonal elements of the corresponding matrix

$$M_{mn} = (i\omega_m + \mu)\delta_{mn} + \chi_{m-n}, \quad (111)$$

up to an overall normalization factor. *Hence, the determinant of the matrix in Eq. (111) is simply a product of the diagonal elements!* This is surprising, since one would naively expect that the determinant depended on the higher Fourier modes of χ . We can show this result explicitly, by checking that

$$\phi_m^{(m')} = T \int_0^\beta d\tau e^{(i\omega_m - i\omega_{m'})\tau} \exp \left\{ \int_0^\tau d\tau' [\chi(\tau') - \chi_0] \right\} \quad (112)$$

is the m' -th eigenvector, with eigenvalue $i\omega_{m'} + \mu + \chi_0$. The verification, is straightforward, provided one first writes χ_{m-n} in terms of the integral over τ , and notes that $\chi(\tau) - \chi_0$ times the last exponential factor in Eq. (112) is equal to the negative τ derivative of the exponential factor. The eigenvalue can then be determined by evaluating the integral by parts; we need to subtract the χ_0 factor from the exponent in order for the boundary terms to vanish when one performs the integration by parts.

Knowing an explicit form for the eigenvectors then allows us to determine the auxiliary Green's function in the general case. As before, we imagine adding an infinitesimal field $\bar{\chi}_{mn} = \bar{\chi} \delta_{mm_0} \delta_{nn_0}$ to the matrix M_{mn} . The auxiliary Green's function is determined by taking the logarithmic derivative of the partition function with respect to $\bar{\chi}$: $g_\sigma^{aux}(i\omega_{n_0}, i\omega_{m_0}) = \partial \ln \mathcal{Z}^{aux}(-\chi_\tau) / \partial \bar{\chi}$. This derivative is easy to calculate, because it says we need only determine the shift in each of the eigenvalues for $\mathcal{Z}^{aux}(-\chi_\tau)$ to first order in $\bar{\chi}$. In the presence of $\bar{\chi}$, it is easy to show that

$$E^{(m')} = i\omega_{m'} + \mu + \chi_0 + \bar{\chi} \phi_{m_0}^{(m')*} \phi_{n_0}^{(m')} + O(\bar{\chi}^2), \quad (113)$$

which leads then to

$$\begin{aligned} g_\sigma^{aux}(i\omega_n, i\omega_m) &= \sum_{m'=-\infty}^{\infty} \frac{\phi_m^{(m')*} \phi_n^{(m')}}{i\omega_{m'} + \mu + \chi_0} \\ &= T \int_0^\beta d\tau \int_0^\beta d\tau' e^{i\omega_n \tau - i\omega_m \tau'} \\ &\quad \times e^{\int_0^\tau d\bar{\tau} [\chi(\bar{\tau}) - \chi_0]} e^{\int_0^{\tau'} d\bar{\tau} [\chi^*(\bar{\tau}) - \chi_0^*]} \\ &\quad \times T \sum_{m'=-\infty}^{\infty} \frac{e^{-i\omega_{m'}(\tau - \tau')}}{i\omega_{m'} + \mu + \chi_0}. \end{aligned} \quad (114)$$

Note that if we choose $\chi(\tau) = \chi(i\nu_l) \exp(-i\nu_l \tau)$, with $\chi(i\nu_l)$ real, then evaluating Eq. (114) to first order in $\chi(i\nu_l)$ reproduces Eq. (71) as it must. For our case, we are interested in the real χ field of Eq. (107). Substituting this field into Eq. (114) and performing some tedious algebra, then yields the results for the diagonal and off-diagonal auxiliary Green's function shown in Table VIII. These results generalize those

TABLE VIII Auxiliary Green's function $g_\sigma^{aux}(i\omega_n, i\omega_m) = T\xi_0 A_{nm} + T(\xi_0 - 1)B_{nm}$ for $n \neq m$ and $g_\sigma^{aux}(i\omega_n, i\omega_n) = T\xi_0 C_{nn} + T(\xi_0 - 1)D_{nn}$ for $n = m$. Here $\xi_0 = 1/[1 + \exp(U\tau - \beta\mu)]$.

A_{nm}	$\frac{1}{i(\omega_m - \omega_n)(i\omega_m + \mu - U) - \frac{e^{i(\omega_n + \mu)\tau - \beta\mu}}{(i\omega_m + \mu)(i\omega_n + \mu)} + \frac{(e^{-i(\omega_m + \mu)\tau} + e^{-\beta\mu})(e^{i(\omega_n + \mu)\tau} - e^{U\tau})}{(i\omega_m + \mu)(i\omega_n + \mu - U)}} + \frac{e^{-i(\omega_m - \omega_n)\tau}}{i(\omega_m - \omega_n)(i\omega_n + \mu)} + \frac{e^{-i(\omega_m - \omega_n)\tau}}{i(\omega_m - \omega_n)(i\omega_m + \mu)}$
B_{nm}	$\frac{-1}{i(\omega_m - \omega_n)(i\omega_m + \mu - U) - \frac{e^{i(\omega_n + \mu)\tau - \beta\mu}}{(i\omega_m + \mu)(i\omega_n + \mu)} + \frac{(e^{-i(\omega_m + \mu)\tau} + e^{-\beta\mu})(e^{i(\omega_n + \mu)\tau} - e^{U\tau})}{(i\omega_m + \mu)(i\omega_n + \mu - U)}} + \frac{e^{-i(\omega_m - \omega_n)\tau}}{i(\omega_m - \omega_n)(i\omega_m + \mu - U)} - \frac{-e^{i\omega_n\tau}(e^{-i\omega_m\tau} - e^{-(\mu - U)\tau}) - e^{\beta\mu}(e^{-i(\omega_m + \mu)\tau} - e^{-U\tau})}{(i\omega_m + \mu - U)(i\omega_n + \mu)} + \frac{i\omega_n + \mu - i(\omega_m - \omega_n)e^{\beta\mu - (i\omega_m + \mu)\tau}}{i(\omega_m - \omega_n)(i\omega_m + \mu)(i\omega_n + \mu)}$
C_{nn}	$\frac{(i\omega_n + \mu - U)\tau - 1 + e^{-i(\omega_n + \mu - U)\tau}}{(i\omega_n + \mu - U)^2} + \frac{1 - e^{-i(\omega_n + \mu - U)\tau} + e^{-\beta\mu}(e^{i(\omega_n + \mu)\tau} - e^{U\tau})}{1 - e^{-i(\omega_n + \mu - U)\tau} + e^{-\beta\mu}(e^{i(\omega_n + \mu)\tau} - e^{U\tau})}} + \frac{(i\omega_n + \mu)(\beta - \tau) - 1 - e^{-\beta\mu + (i\omega_n + \mu)\tau}}{(i\omega_n + \mu)^2}$
D_{nn}	$\frac{-i(\omega_n + \mu - U)\tau - 1 + e^{i(\omega_n + \mu - U)\tau}}{(i\omega_n + \mu - U)^2} + \frac{1 - e^{i(\omega_n + \mu - U)\tau} + e^{\beta\mu}(e^{-i(\omega_n + \mu)\tau} - e^{-U\tau})}{1 - e^{i(\omega_n + \mu - U)\tau} + e^{\beta\mu}(e^{-i(\omega_n + \mu)\tau} - e^{-U\tau})}} + \frac{(i\omega_n + \mu)(\tau - \beta) - 1 - e^{\beta\mu - (i\omega_n + \mu)\tau}}{(i\omega_n + \mu)^2}$

of Brandt and Urbanek (1992) off of half filling and correct some typos in Zlatić *et al.* (2001).

Once g_σ^{aux} is known, then we follow the same procedure as before to calculate the relevant averages. The object of interest is $\text{Tr}_c \mathcal{T}_\tau \langle \exp(-\beta\mathcal{H}_0) S(\lambda - \chi_\tau) \rangle$, which can be viewed as the partition function corresponding to a particle moving in both the λ and χ_τ fields. Since the partition function is the determinant of the inverse of the Green's function, and since the Green's function $g_\sigma(i\omega_n, i\omega_m)$ associated with the $\lambda - \chi_\tau$ field is related to the auxiliary Green's function via

$$[g_\sigma]^{-1} = [g_\sigma^{aux}]^{-1} - \lambda_{n\sigma} \delta_{nm}, \quad (115)$$

we immediately conclude that

$$\begin{aligned} & \text{Tr}_c \mathcal{T}_\tau \langle \exp(-\beta\mathcal{H}_0) S(\lambda - \chi_\tau) \rangle \\ &= \mathcal{Z}^{aux}(-\chi_\tau) \prod_{\sigma=1}^{2s+1} \text{Det}[\delta_{nm} - g_\sigma^{aux}(i\omega_n, i\omega_m) \lambda_{n\sigma}] \end{aligned} \quad (116)$$

Substituting into Eq. (108) yields our final result for the f -electron Green's function

$$F_\eta(\tau) = -\frac{1}{\mathcal{Z}_{imp}} e^{-(E_{f\eta} - \mu_f)\tau} \mathcal{Z}^{aux}(-\chi_\tau) \prod_{\sigma=1}^{2s+1} \text{Det}[\delta_{nm} - g_\sigma^{aux}(i\omega_n, i\omega_m) \lambda_{m\sigma}]. \quad (117)$$

One needs to recall that $\mathcal{Z}^{aux}(-\chi_\tau)$ changes with τ because the χ_τ field depends on τ . One can easily verify in the case where $E_{f\eta}$ has no η dependence, and in the limit where $\tau \rightarrow 0^+$, then $g_\sigma^{aux} \rightarrow \delta_{nm}/(i\omega_n + \mu)$ and the f -electron Green's function can be evaluated explicitly, producing $F_\eta(0^+) = -w_0$ as it must. Similarly, for $\tau \rightarrow \beta^-$ one finds $g_\sigma^{aux} \rightarrow \delta_{nm}/(i\omega_n + \mu - U)$ and $F_\eta(\beta^-) = -w_1$.

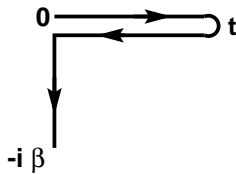


FIG. 3 Contour c used in integrating the action in the Keldysh formalism.

One is also interested in the f -electron Green's function on the real axis. Unfortunately, there is no obvious way to analytically continue Eq. (117) from the imaginary to the real axis. Instead, one is forced to re-evaluate the f -electron Green's function directly on the real axis. Since there is no time-translation invariance to the effective fields, it is most convenient to employ a Keldysh formalism, even though the f -electron is in equilibrium. In the Keldysh formalism, we need to perform the path integral in the time domain over the contour illustrated in Fig. 3 to determine the contour-ordered Green's function. The Keldysh (greater) Green's function for real time t becomes

$$F_\eta^>(t) = -\text{Tr}_{cf} \frac{\langle e^{-\beta\mathcal{H}_{imp}} S_c(\lambda) f_\eta(t) f_\eta^\dagger(0) \rangle}{\mathcal{Z}_{imp}} \quad (118)$$

with $f_\eta(t) = \exp(it\mathcal{H}_{imp}) f_\eta(0) \exp(-it\mathcal{H}_{imp})$ and

$$S_c(\lambda) = \mathcal{T}_c \exp \left[\int_c d\bar{t} \int_c d\bar{t}' \sum_\sigma c_\sigma^\dagger(\bar{t}) \lambda(\bar{t}, \bar{t}') c_\sigma(\bar{t}') \right]. \quad (119)$$

One can directly determine $\lambda(\omega)$ on the real axis. Using this function one then finds

$$\begin{aligned} \lambda(\bar{t}, \bar{t}') &= -\frac{1}{\pi} \int_{-\infty}^{\infty} d\omega \text{Im} \lambda(\omega) \exp[-i\omega(\bar{t} - \bar{t}')] \\ &\times [f(\omega) - \theta_c(\bar{t} - \bar{t}')] \end{aligned} \quad (120)$$

where $\theta_c(\bar{t} - \bar{t}') = 0$ if \bar{t}' is in front of \bar{t} on the contour c and 1 if it is behind.

Using an equation of motion, similar to Eq. (105), leads us to introduce a time-dependent field

$$\chi_t(\bar{t}, \bar{t}') = -iU\theta_c(t - \bar{t})\delta_c(\bar{t} - \bar{t}'). \quad (121)$$

The derivation of the Green's function follows as before resulting in the analogue of Eq. (117)

$$\begin{aligned} F_\eta^>(t) &= -\frac{1}{\mathcal{Z}_{imp}} e^{-i(E_{f\eta} - \mu)t} \mathcal{Z}^{aux}(-\chi_t) \\ &\times \prod_{\sigma=1}^{2s+1} \text{Det}[\delta(\bar{t} - \bar{t}')] \\ &+ \int_c d\bar{t}' g_\sigma^{aux}(\bar{t}, \bar{t}') \lambda_\sigma(\bar{t}', \bar{t}'), \end{aligned} \quad (122)$$

TABLE IX $g_{\sigma}^{aux}(\bar{t}, \bar{t}')$ for different orderings of t , \bar{t} , and \bar{t}' along the contour c . The symbol ξ_0 satisfies $\xi_0 = 1/[1 + \exp(iUt - \beta\mu)]$.

$\xi_0 \exp[i\mu(\bar{t} - \bar{t}')] $	$t < \bar{t} < \bar{t}'$
$\xi_0 \exp[iUt + i(\mu - U)\bar{t} - i\mu\bar{t}']$	$\bar{t} < t < \bar{t}'$
$\xi_0 \exp[i(\mu - U)(\bar{t} - \bar{t}')] $	$\bar{t} < \bar{t}' < t$
$(\xi_0 - 1) \exp[i\mu(\bar{t} - \bar{t}')] $	$t < \bar{t}' < \bar{t}$
$(\xi_0 - 1) \exp[-iUt + i\mu\bar{t} - i(\mu - U)\bar{t}']$	$\bar{t}' < t < \bar{t}$
$(\xi_0 - 1) \exp[i(\mu - U)(\bar{t} - \bar{t}')] $	$\bar{t}' < \bar{t} < t$

except now, the determinant is of a *continuous* matrix operator.

The function $g_{\sigma}^{aux}(\bar{t}, \bar{t}')$ can be found directly from its operator definition

$$g_{\sigma}^{aux}(\bar{t}, \bar{t}') = -\frac{1}{\mathcal{Z}^{aux}(-\chi_t)} \text{Tr}_c \langle \mathcal{T}_c e^{-\beta\mathcal{H}_0} S_c(-\chi_t) c_{\sigma}(\bar{t}) c_{\sigma}^{\dagger}(\bar{t}') \rangle \quad (123)$$

noting that we order the times along the contour c and that $\mathcal{Z}^{aux}(-\chi_t) = [1 + \exp(\beta\mu - iUt)]^{2s+1}$. The result is shown in Table IX for the six different possible orderings of t , \bar{t} , and \bar{t}' along the contour c . Brandt and Urbanek (1992) show how to calculate the discretized determinant in an efficient manner. If we use a quadrature rule

$$\int_c dt I(t) = \sum_i W_i I(t_i) \quad (124)$$

with weights W_i for the discrete set of times $\{t_i\}$ on the contour c , then the continuous determinant can be approximated by the discrete determinant

$$\text{Det}[W_i \{ \frac{\delta_{ij}}{\Delta t_c} + \sum_k g_{\sigma}^{aux}(t_i, t_k) W_k \lambda_{\sigma}(t_k, t_j) \}] \quad (125)$$

for each σ ($1/\Delta t_c$ is the approximation to the delta function on contour c with Δt_c the width of the interval that includes the delta function; for a (midpoint) rectangular quadrature rule, one takes $\Delta t_c = 1/W_i$).

Now the Keldysh Green's function satisfies the following spectral formula

$$F_{\eta}^{>}(t) = \int_{-\infty}^{\infty} d\omega e^{-i\omega t} [f(\omega) - 1] A_{\eta}^f(\omega) \quad (126)$$

because it involves the product of the spectral function $A_{\eta}^f(\omega)$ with the relevant distribution function $[f(\omega) - 1]$. The (greater) Green's function obviously satisfies

$$F_{\eta}^{>}(t) = F_{\eta}^{>*-}(-t). \quad (127)$$

We break the spectral density into its even and odd pieces: $A_{\eta}^{fe}(\omega) = [A_{\eta}^f(\omega) + A_{\eta}^f(-\omega)]/2$ and $A_{\eta}^{fo}(\omega) = [A_{\eta}^f(\omega) - A_{\eta}^f(-\omega)]/2$. Then we use Eq. (127) to show that

$$A_{\eta}^{fe}(\omega) = -\frac{1}{\pi} \int_0^{\infty} dt [(\cosh\beta\omega + 1) \text{Re}\{F_{\eta}^{>}(t)\}] \cos(\omega t)$$

$$- \sinh(\beta\omega) \text{Im}\{F_{\eta}^{>}(t)\} \sin(\omega t)] \quad (128)$$

and

$$A_{\eta}^{fo}(\omega) = -\frac{1}{\pi} \int_0^{\infty} dt [-\sinh(\beta\omega) \text{Re}\{F_{\eta}^{>}(t)\} \cos(\omega t) + (\cosh\beta\omega + 1) \text{Im}\{F_{\eta}^{>}(t)\} \sin(\omega t)]. \quad (129)$$

At half filling, we have that $A_{\eta}^{fo}(\omega) = 0$, so that Eqs. (128) and (129) reduce to

$$A_{\eta}^f(\omega) = -\frac{2}{\pi} \int_0^{\infty} dt \text{Re}\{F_{\eta}^{>}(t)\} \cos(\omega t). \quad (130)$$

This then determines the localized electron spectral function on the real axis.

G. Spontaneous Hybridization

Sham and coworkers proposed that correlations can lead to a spontaneous ferroelectricity via the creation of a dynamically correlated hybridization in the FK model (Portengen *et al.*, 1996a,b). Such an effect is necessarily a subtle one, because it is well known that Elitzur's theorem (Elitzur, 1975) applies to the FK model (Subrahmanyam and Barma, 1988) and no such spontaneous hybridization can occur at any finite temperature. Numerical and analytical calculations in finite-dimensions (Farkasovský, 1997, 1999, 2002) and in infinite-dimensions (Czycholl, 1999) indicated that such spontaneous hybridization did not occur in the FK model, but they did not cover all of the available parameter space. An alternate way to test these ideas is to directly calculate the susceptibility toward spontaneous hybridization formation (Zlatić *et al.*, 2001).

Because the f -electron dynamics are local, only the local susceptibility toward spontaneous hybridization is relevant. We will restrict ourselves to the spinless case for simplicity. The local spontaneous hybridization susceptibility is defined by

$$\chi_{hyb} = -\int_0^{\beta} d\tau \frac{1}{\mathcal{Z}_{imp}} \times \text{Tr}_{cf} \langle \mathcal{T}_{\tau} \exp(-\beta\mathcal{H}_{imp}) S(\lambda) f(\tau) d^{\dagger}(\tau) d(0) f^{\dagger}(0) \rangle. \quad (131)$$

If we introduce the time-dependent field $\lambda(\tau, \tau')$ that couples the itinerant electron at τ' to its Hermitian conjugate at time τ [in equilibrium, we have $\lambda(\tau, \tau') = \lambda(\tau - \tau')$], then we can express the susceptibility in terms of a functional derivative

$$\begin{aligned} \chi_{hyb} &= -\int_0^{\beta} d\tau \frac{\delta F(\tau)}{\delta \lambda(\tau, 0)} \\ &= \int_0^{\beta} d\tau \frac{e^{-(E_f - \mu_f - U)\tau} \mathcal{Z}^{aux}(-\chi_{\tau}) \delta \text{Det}[1 - g^{aux} \lambda]}{\mathcal{Z}_{imp} \delta \lambda(\tau, 0)}. \end{aligned} \quad (132)$$

Noting that $\text{Det}A = \exp[\text{Tr}(\ln A)]$, allows us to immediately compute

$$\frac{\delta \text{Det}[1 - g^{aux} \lambda]}{\delta \lambda(\tau, 0)} = -\text{Det}[1 - g^{aux} \lambda] [(1 - g^{aux} \lambda)^{-1} g^{aux}]_{0\tau}, \quad (133)$$

where matrix multiplication is understood. Substituting Eq. (133) into Eq. (132) then immediately yields

$$\chi_{hyb} = \int_0^\beta d\tau \int_0^\beta d\tau' F(\tau) (1 - g^{aux} \lambda)_{0\tau'}^{-1} g^{aux}_{\tau'\tau}, \quad (134)$$

where one must recall that g^{aux} must be recomputed for each τ value, since it depends explicitly on χ_τ . Reexpressing Eq. (134) in terms of Fourier transformed quantities produces

$$\chi_{hyb} = \int_0^\beta d\tau F(\tau) T \sum_{mn} (1 - g^{aux} \lambda)_{mn}^{-1} g^{aux}(i\omega_n, \tau), \quad (135)$$

where the partial Fourier transform of the auxiliary Green's function satisfies

$$g^{aux}(i\omega_n, \tau) = T \sum_m g^{aux}(i\omega_n, i\omega_m) e^{i\omega_m \tau}. \quad (136)$$

Note that this final result for the spontaneous hybridization susceptibility in Eq. (135) requires the matrix inverse of $[1 - g^{aux} \lambda]$ which is straightforward to compute numerically for a finite truncation of the matrix.

III. ANALYSIS OF SOLUTIONS

A. Charge-Density-Wave Order and Phase Separation

The first problem examined in the FK model with DMFT was the problem of ordering into a two-sublattice charge density wave (CDW) at half filling on a hypercubic lattice (Brandt and Mielsch, 1989). Because the hypercubic lattice is bipartite, we expect a transition at finite temperature for all U (Kennedy and Lieb, 1986) and indeed this is true. Since the original work, a number of other studies of CDW order and phase separation followed (Brandt and Mielsch, 1990, 1991; van Dongen, 1992; van Dongen and Vollhardt, 1990; Freericks, 1993a,b; Freericks *et al.*, 1999; Freericks and Lemański, 2000; Gruber *et al.*, 2001; Letfulov, 1999) on both the hypercubic and the Bethe lattices. We concentrate on the spinless FK model here.

Since the DMFT is in the thermodynamic limit, we can determine the transition temperature for a continuous transition by simply finding the temperature at which the susceptibility diverges. Using the results of Table I, we find that the susceptibility diverges whenever the denominator of $\gamma(\mathbf{q})$ vanishes. In Fig. 4, we plot the T_c for checkerboard CDW order ($X = -1$) and the spinodal temperature for phase separation ($X = 1$) near half filling (a) and near the band edge (b). Note that the transition temperature has a maximum that is about 1/40th

of the effective bandwidth ($\approx 4t^*$) and at half filling for large U it behaves like $T_c \approx t^{*2}/4U$ [as expected for the equivalent (Ising) spin model] and for small U it appears to grow like $T_c \approx U^2 |\ln U|$ [which is different from the expected exponentially growing behavior that occurs in most nested systems at weak coupling] (van Dongen, 1992; van Dongen and Vollhardt, 1990). As we move away from half filling, the checkerboard phase is suppressed (disappearing at small and large U) and the phase separation is enhanced (especially at large U). Near the band edge [panel (b)], there is no checkerboard instability, but the phase separation becomes even stronger. We see that the spinodal temperature for phase separation does not depend too strongly on the electron filling, and surprisingly, the curves cross as a function of U .

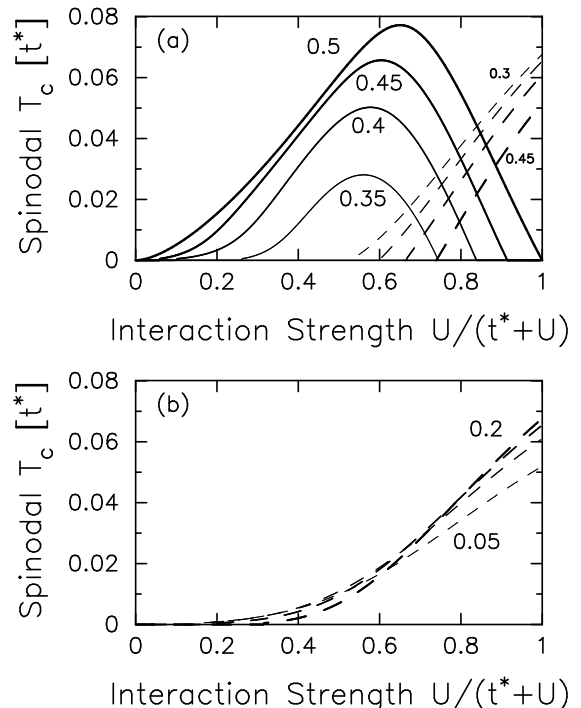


FIG. 4 T_c for CDW order in the spinless FK model (a) near half filling and (b) near the band edge. The solid lines denote checkerboard order and the dashed lines denote the spinodal decomposition temperature for phase separation (the true first-order transition temperature is always higher than the spinodal temperature). The labels denote the electron filling ρ_e [which runs from top to bottom for the dashed lines in panel (a) as 0.3, 0.35, 0.4, and 0.45, the spinodal temperature for 0.5 vanishes; in panel (b) the lines are for 0.05, 0.1, 0.15, and 0.2—note how the curves cross as a function of U]; the ion filling is fixed at $\rho_f = 0.5$.

We can also examine the transition temperature for fixed U as a function of electron concentration (with $\rho_f = 0.5$ again) as shown in Fig. 5. For small U [panel (a)], we see that the region of the checkerboard phase increases as U increases, as does the region of phase separation. For large U [panel (b)], we see that the T_c curve

for the checkerboard phase develops a cusp at half filling (Freericks and Lemański, 2000), and that the region of stability shrinks as U increases further. Phase separation dominates for large U , as expected.

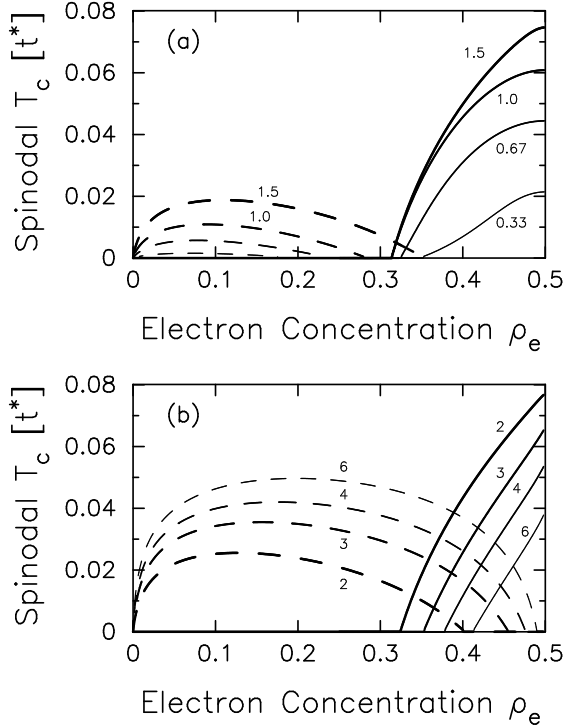


FIG. 5 T_c for CDW order in the spinless FK model (a) for small U and (b) for large U . The solid lines denote checkerboard order and the dashed lines denote the spinodal decomposition temperature for phase separation (the true first-order transition temperature is always higher than the spinodal temperature). The labels denote the value of U ; the ion filling is fixed at $\rho_f = 0.5$.

It turns out, that for small U , the system also has instabilities to CDW phases with incommensurate values of X (i.e., X changes continuously with the electron concentration). These results are summarized with a projected phase diagram (Freericks, 1993a) in Fig. 6, which plots the regions of stability for different CDW phases as determined by the ordering wavevector of the *initial ordered phase* as T is lowered to the first (continuous) instability at T_c (as determined by the divergence of the relevant susceptibility). This is an approximation of the zero-temperature phase diagram—the phase boundaries may change as one reduces the temperature from T_c to zero, but we are not able to study the ordered phase of incommensurate states. They may also change if there are first-order phase transitions. Note how the system segregates at large U for all fillings except $\rho_e = 0.5$ where it degenerates with the checkerboard phase.

In order to understand the incommensurate order better, we plot $T_c(X)$ for different electron fillings at $U = 0.5$ in Fig. 7. Near half filling, these curves are peaked at $X = -1$, but as the system is doped sufficiently far from

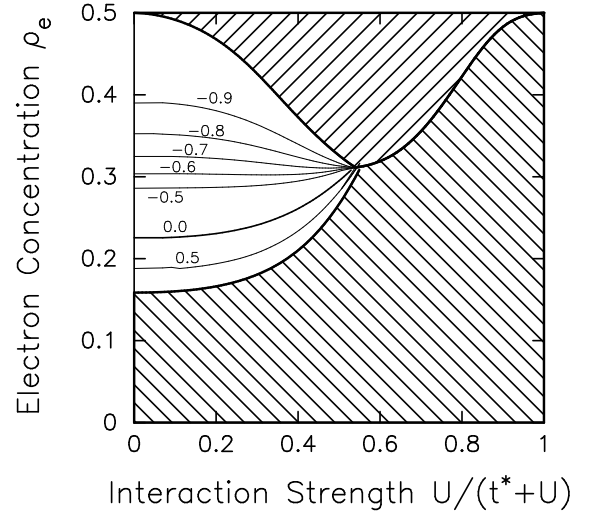


FIG. 6 Projected phase diagram for the spinless FK model with $\rho_f = 0.5$. The shaded region near half filling denotes the region of stability of the checkerboard phase ($X = -1$), the shaded region near the band edge denotes the region of stability for the segregated phase (as determined by the spinodal decomposition temperature), and the white region shows the incommensurate phases at small U (the solid lines are lines of constant X).

half filling, the curves develop a peak at an intermediate value of X which evolves towards $X = 0$ as $T_c \rightarrow 0$ ($\rho_e = 0.35$ and 0.3). Then, if doped further from half filling, T_c rises again and the ordering wavevector evolves smoothly toward $X = 1$ ($\rho_e = 0.2$ and 0.15). Note that the region of stability for positive (incommensurate) X is much smaller than that of negative (incommensurate) X . In the large U case, the maximum always appears at $X = -1$ or $X = 1$ and the incommensurate order disappears (see Fig. 6).

It is interesting to also examine the dynamical charge susceptibility (Freericks and Miller, 2000; Shvaika, 2000, 2001). We don't expect the dynamical susceptibility to show any signs of the CDW instability because it is an isolated susceptibility, and the divergence of the static susceptibility arises solely from the coupling to the static electrons which produced an additional contribution to the (isothermal) static susceptibility. Indeed this is the case, as can be seen for the checkerboard ($X = -1$) dynamical charge susceptibility at $U = 4$ shown in Fig. 8. We plot the imaginary part of the susceptibility only. Note how at high temperature there is a low-energy peak and a charge-transfer peak (centered at $\nu \approx U = 4$), but as the temperature is lowered, the low-energy peak rapidly disappears and the susceptibility has little further temperature dependence in the homogeneous phase (even though we have passed through T_c which occurs at 0.0547). We also find that as we move from the zone corner toward the zone center, the higher-energy (charge-transfer peak) loses spectral weight but does not have much dispersion or peak narrowing, while the low-energy

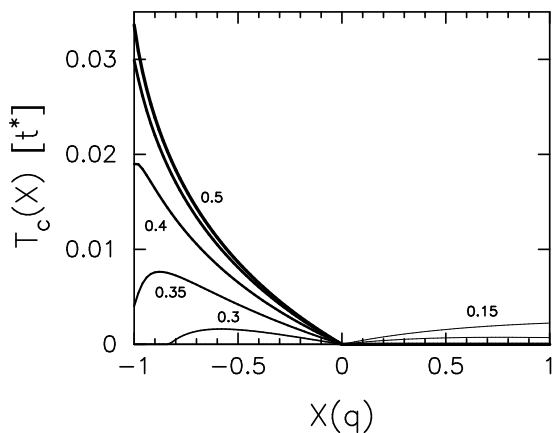


FIG. 7 CDW transition temperature as a function of the ordering wavevector described by X . The numbers label the electron filling with the filling changing in steps of 0.05 ($U = 0.5$ and $\rho_f = 0.5$). The results for $\rho_e = 0.25$ are too low to be seen on this figure.

peak shows an appreciable dispersion toward lower energy and narrows as we approach the zone center (not shown). At the zone center, the dynamical charge susceptibility vanishes.

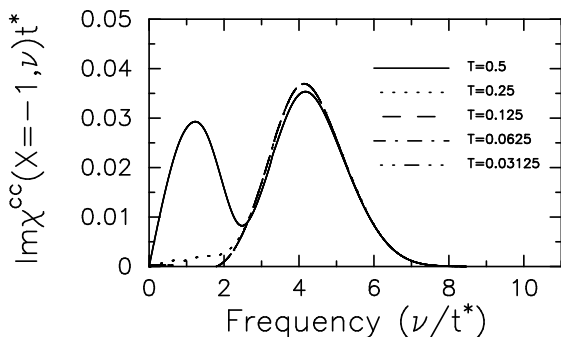


FIG. 8 Imaginary part of the dynamical charge susceptibility at $X = -1$ and $U = 4$. Note the low-energy spectral weight which rapidly disappears as T is lowered, and note further that there is no signal of the CDW order (which sets in at $T_c = 0.0547$) in the isolated susceptibility.

The results on the Bethe lattice are similar to those on the hypercubic lattice except for the incommensurate order. We will concentrate on discussing the Bethe lattice case for the remainder of this section. We begin by examining the ordered checkerboard phase at half filling. In Fig. 9, we plot the electronic density of states for $U = 1$ above T_c , and below T_c in steps down to $T = 0$. Inset in the figure is a plot of the “normalized” order parameter $w_1^A - w_1^B$ as a function of temperature. The order parameter takes a BCS-like form, being flat for low temperatures and having a square-root dependence as T_c is approached [this behavior changes as $U \rightarrow 0$, see van Dongen (1992)]. The density of states evolves with

temperature in the ordered phase because of this temperature dependence in the order parameter. Each sublattice has a sharp peak in the density of states (which becomes singular at $T = 0$) as expected. Note the interesting behavior of the subgap states, which split into two subbands then shrink and disappear as T is reduced. In the limit as $U \rightarrow \infty$, the bandwidth of the subbands goes to zero, and the density of states becomes a delta function on each sublattice (van Dongen, 1992).

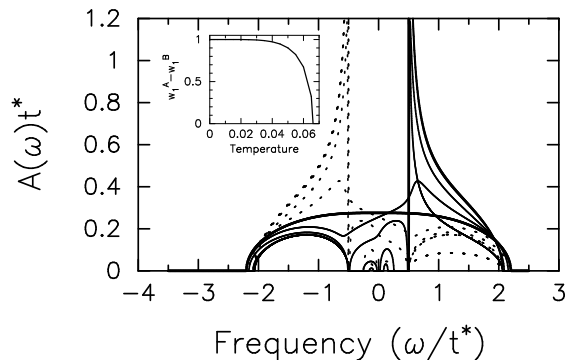


FIG. 9 Density of states above and below $T_c = 0.06614$ in the spinless FK model at half filling on a Bethe lattice with $U = 1$. The DOS is plotted for $T = 0.07$, $T = 0.065$, $T = 0.06$, $T = 0.045$, $T = 0.03$, and $T = 0$. Note that in the ordered phase, there are two DOS plots, one for each sublattice (solid and dotted lines); these DOS are mirror images of each other. The inset plots the “normalized” order parameter as a function of temperature, which has a BCS-like shape. The exact form is known for $U \rightarrow \infty$ and $U \rightarrow 0$ (van Dongen, 1992), and one expects, for smaller U , that the shape will change dramatically since the order parameter becomes very small in the range $0.5T_c < T < T_c$.

In addition to the checkerboard phase, we can also examine the phase-separated (segregated) phase, where the itinerant electrons avoid the localized ions. If we take the limit $U \rightarrow \infty$, where the phase separation is the strongest, we find the plot projected onto the $w_1 = (1 - \rho_e)/2$ plane (which corresponds to relative half filling of the lower Hubbard band) shown in Fig. 10. The solid line denotes the first-order phase transition line calculated by performing a Maxwell construction on the free energy (Freericks *et al.*, 1999). The dotted line is the spinodal decomposition temperature calculated from the divergence of the susceptibility. Note how the two temperatures track well with one another and how they meet at the maximal T_c as they must because that is the temperature where the first-order phase transition becomes second order.

Finally, we examine higher-period ordered phases on the Bethe lattice (Gruber *et al.*, 2001). Since the Bethe lattice does not have the same periodicity properties of regular lattices, one must construct higher-period ordered phases with care. This is done by working directly in real space and repeating quasi-one-dimensional patterns of charge density waves according to the different

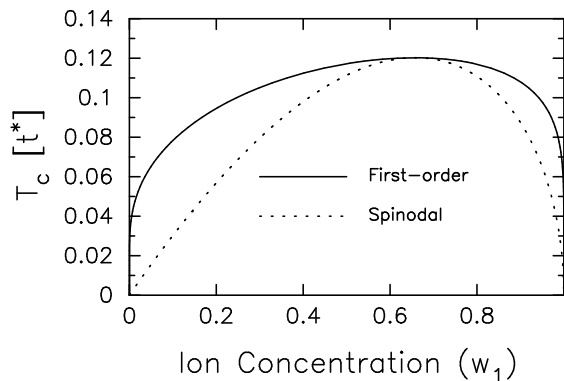


FIG. 10 Phase diagram for the first-order phase separation transition on a Bethe lattice with $w_1 = (1 - \rho_e)/2$ and $U \rightarrow \infty$. The solid line is the first-order transition temperature and the dotted line is the spinodal temperature.

levels of the tree that forms the Bethe lattice. A period-two phase is the conventional checkerboard phase with alternating charge densities on each level. There is a region of parameter space where the period-three phase has been shown to be stable. This is illustrated in Fig. 11 (a), which is a restricted phase diagram at $T = 0$ that compares the ground-state energy of the segregated phase, the period-two phase, the period-three phase and the homogeneous phase. Note the wide region of stability for the period-three phase (this region can shrink as additional phases are added to the phase diagram; in particular, we conjecture that the homogeneous phase stability will disappear as higher-period phases are added to the diagram). To examine in more detail, we plot the free energy of the homogeneous phase, the period-two phase, and the period three phase for $U = 3$, $\rho_f = 2/3$, and $\mu = 0.84861$ ($\rho_e \approx 0.332$). Note how at low temperature the period-three phase is lowest in energy, but how there must be a higher-period phase that intervenes between the period-two and period three phases for the free energy to be continuous. We expect the phase transition from the period-three phase to be first order. Note further how the period-two phase free energy smoothly joins the homogeneous-phase free energy, as expected for a continuous (second-order) phase transition.

B. Mott-like Metal-Insulator Transitions

The FK model is not a fermi liquid (Si *et al.*, 1992) whenever ρ_f is not equal to 0 or 1 (when $\rho_f = 0$ or 1, the FK model is a noninteracting fermi gas). This is because the f -electrons appear like disorder scatterers (with an annealed averaging rather than the conventional quenched averaging). These scatterers always produce a finite lifetime at the fermi surface, so rigorously quasiparticles do not exist and the system is a non-fermi-liquid. If U is small, one can still view the system as a “dirty fermi liquid”, but the system rapidly changes character

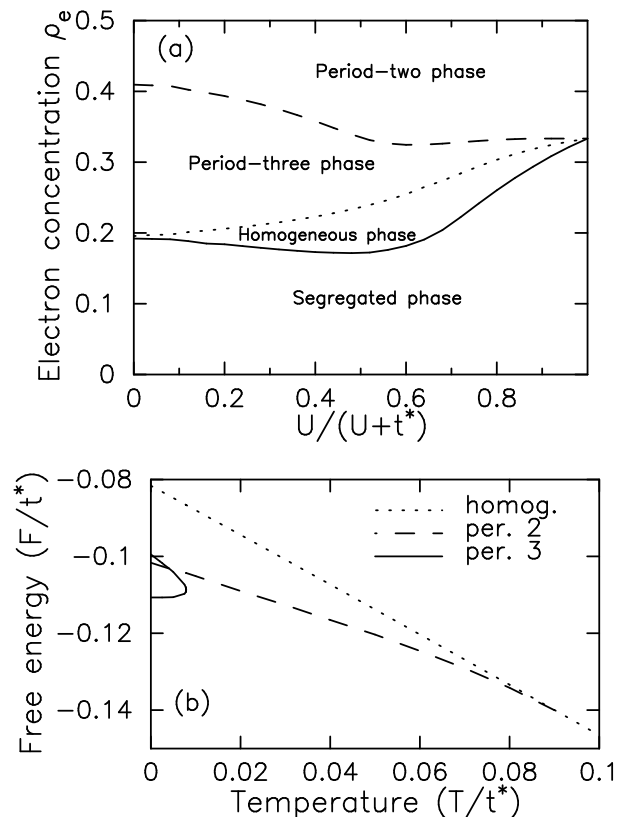


FIG. 11 (a) Restricted phase diagram on the Bethe lattice for $\rho_f = 2/3$ and (b) free energy versus temperature for $\mu = 0.84861$. Note the large region of stability of the period-three phase in (a) and how the shape of the free-energy curves in (b) suggest that phase transitions to higher-period phases will be *first order*.

as U increases further. The non-fermi-liquid character can also be seen in the self energy on the real axis. The imaginary part does have a quadratic behavior, but the curvature is the *wrong sign* and the intercept at $\omega = 0$ *does not go to zero* as $T \rightarrow 0$ as it must in a fermi liquid. Similarly, the real part of the self energy is linear, but the slope *has the wrong sign* near $\omega = 0$.

It is known in a fermi liquid with a local self energy that the fermi surface and the DOS at the fermi level (at $T = 0$) are unchanged as the correlations increase (Müller-Hartmann, 1989b). But because the FK model is not a fermi liquid there is no restriction on the DOS. van Dongen and Leinung (1997) studied the Mott-like metal-insulator transition on the Bethe lattice in detail; in this study, one continues the homogeneous phase down to $T = 0$, ignoring any possible CDW phases. They found a simple cubic equation for the interacting DOS on the Bethe lattice which produces the results shown in Fig. 12. One can see that for weak coupling, the DOS is essentially unchanged from the noninteracting case, but as U is increased further, the DOS first develops a pseudogap, where spectral weight is depleted near the chemical potential, and then it gets fully reduced to zero. As U

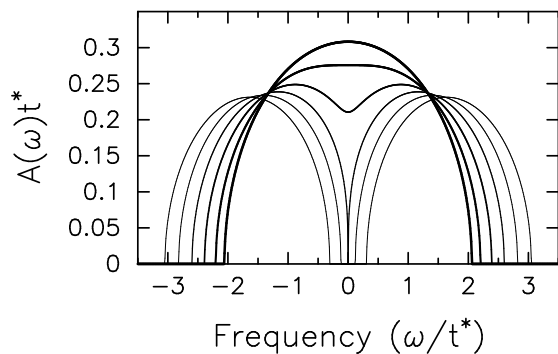


FIG. 12 Itinerant electron DOS for the spinless FK model on the Bethe lattice for different values of U ranging from 0.5 to 3.0 in steps of 0.5 ($\rho_e = \rho_f = 0.5$). The metal-insulator transition occurs at $U=2$. It is preceded by a pseudogap phase for ($1 < U < 2$).

is increased further, the system splits into lower and upper Hubbard bands, and the bandwidth of each subband decreases as U increases, while the separation increases between the two bands. This is precisely the kind of metal-insulator transition that Mott envisioned, where the DOS within a single band is suppressed to zero, but unlike Mott’s prediction that the transition would generically be a discontinuous first-order transition, here it is a continuous second-order transition.

The metal-insulator transition occurs precisely at the point where the self energy develops a pole and diverges at $\omega = 0$. This forces the DOS at the chemical potential to equal 0 on any lattice. On lattices where the noninteracting DOS has band edges, the interacting DOS can remain zero within a correlation-induced gap. But on the hypercubic lattice, which has an infinite bandwidth, with an exponentially small DOS for large frequency, there is no precise gap, rather the DOS is exponentially small in the “gap region” and then becomes of order one within the Hubbard subbands. Indeed, on the hypercubic lattice, the DOS looks much like that in Fig. 12, but the metal-insulator transition occurs at $U \approx 1.5$ for $\rho_e = \rho_f = 0.5$.

The DOS of the FK model does have a curious property—it is independent of temperature in the homogeneous phase (van Dongen, 1992) (which was proved by mapping the FK model onto a coordination-three noninteracting Bethe lattice problem, which then has a temperature-independent DOS). The temperature-independence holds only in canonical formulations, where both ρ_e and ρ_f are separately fixed as functions of T [ignoring the trivial shift of the DOS with $\mu(T)$]. In cases where the total electron concentration is fixed, but can vary between itinerant and localized electrons, the DOS will vary with T since ρ_f generally varies with T .

One can also examine the spectral function of the localized electrons (Brandt and Urbanek, 1992), which is temperature dependent! The DOS shares similar behavior with the conduction-electron DOS, having a gap

when the correlation energy is large. We plot results for $U = 2.5$ where the localized electron DOS develops a pseudogap and then a gap region as T is lowered. Note how the gap develops as T is reduced below 0.4.

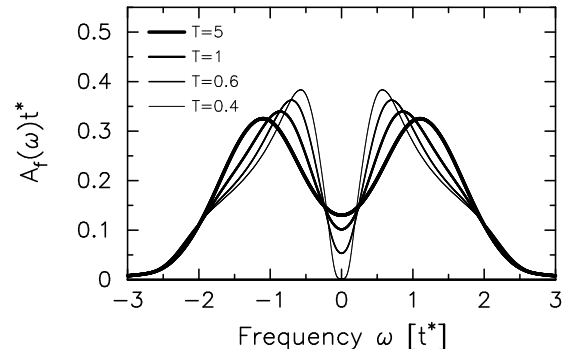


FIG. 13 Single particle DOS of the f -electrons for the spinless FK model at half filling on a Bethe lattice with $U = 2.5$. Note how the gap opens up as T is reduced even though the calculations are above the CDW transition temperature (which occurs at $T = 0.113746$). The DOS is symmetric due to particle-hole symmetry.

C. Falicov-Kimball-like Metal-Insulator Transitions

The original work of Falicov, Kimball, and Ramirez (Falicov and Kimball, 1969; Ramirez *et al.*, 1970) studied a different type of metal-insulator transition—one where the character of the electronic states was unchanged, but their statistical occupancy fluctuated with temperature or pressure. As occupancy shifted from the itinerant to localized bands, the system underwent a charge-transfer metal-insulator transition. One of the main points of interest of this model was that the presence of a Coulomb interaction U between the two types of electrons could make the transition become discontinuous (first-order). The original approximations used a mean-field theory which showed these first-order transitions. Later, Plischke (1972) proposed that when the coherent-potential approximation was applied to the FK model, the first-order transitions disappeared. This was refuted by Gonçalves da Silva and Falicov (1972).

In the Falicov and Kimball approach to the metal-insulator transition, one works with spin-one-half electrons and fixes the total electron concentration (usually at $\rho_{total} = \rho_e + \rho_f = 1$). Alternatively, one can perform a partial particle-hole transformation on the f -electrons, and have a system where $\rho_e = \rho_f$ and U is negative (attractive). There is a gap Δ to creating an electron-hole pair. We will concentrate on the electronic picture here (where one has $E_f = U - \Delta - 2t^*$) and the choice $\Delta = t^*$ which most closely represents the original FK problem. We work on an infinite-coordination Bethe lattice.

This model for metal-insulator transitions was solved in infinite dimensions by Chung and Freericks (1998). It

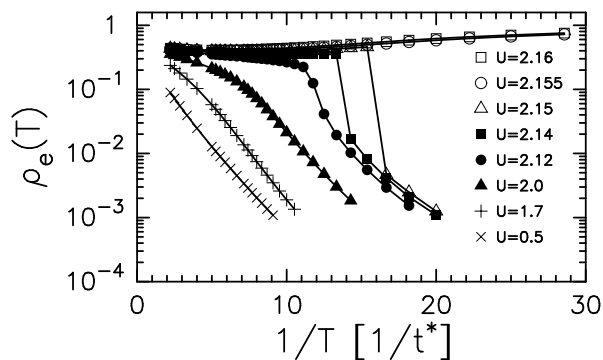


FIG. 14 Conduction electron density as a function of $1/T$ for the spin-one-half FK model on a Bethe lattice with $\Delta = 1$. The different curves correspond to different values of U .

requires a fine tuning of the Coulomb interaction in order to have a first-order phase transition. This is illustrated in Fig. 14, where we plot the conduction electron density ρ_e versus inverse temperature $1/T$ for different values of U (recall E_f also varies with U , since Δ is fixed at 1). The states that have $\rho_e \rightarrow 0$ as $T \rightarrow 0$ are insulators, while those with finite ρ_e are metallic. We say a metal-insulator transition occurs when there is a discontinuous jump in the electron density, which goes from the metallic phase at high temperature to the insulating phase at low T . This occurs for $2.12 < U < 2.155$ when $\Delta = 1$. The shape of these curves is remarkably similar to those found in the mean-field-theory solution of Ramirez *et al.* (1970) and verifies that first-order metal-insulator transition do occur within the CPA.

The interacting electronic DOS is plotted in Fig. 15 for four different values of U (Chung and Freericks, 1998). In panel (a) we show the metallic case $U = 2.16$, where the DOS is large at the chemical potential ($\omega = 0$) and does not depend strongly on T . As U is reduced to 2.15, where there is a discontinuous metal-insulator phase transition, we see a huge reconstruction of the DOS at the transition, where the DOS at the chemical potential becomes small and decreases to zero as $T \rightarrow 0$. In panel (c), we see the evolution of the insulating phase for the strongly correlated insulator $U = 2.12$. Here the conduction electron occupation does not evolve in a simple exponential fashion, but has a much sharper increase as T increases. The DOS has upper and lower Hubbard bands, with the lower band losing spectral weight as $T \rightarrow 0$. Finally, in panel (d), we show the DOS for a weakly correlated insulator. Here the conduction electron density evolves in an exponential fashion and there is no DOS at the chemical potential, since all of the electronic occupation is thermally activated.

D. Intermediate-Valence

The FK model does not have any hybridization between the itinerant and localized electrons, so it can-

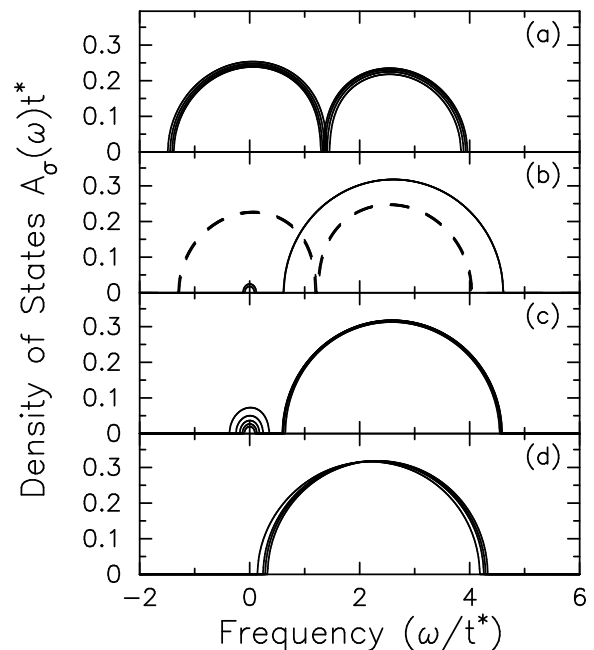


FIG. 15 Conduction-electron DOS for the spin-one-half FK model on a Bethe lattice with $\Delta = 1$. The different panels are for different values of U , and the results are plotted for a number of different temperatures [the dashed lines are used in panel (b) for clarity]. The DOS has T dependence because ρ_f varies with T .

not have any quantum-mechanical mixed valence at finite temperature (Subrahmanyam and Barma, 1988) which is quantified by having a nonzero average $\langle c^\dagger f \rangle$. Nevertheless, one can have a *classical* intermediate-valence state, where the average f -electron occupancy lies between 0 and 1 for $T \rightarrow 0$. In many such cases, one would expect CDW order (or phase separation) to take over in the ground state, but there are regions of parameter space where the system appears to remain in a homogeneous classical intermediate-valence state all the way to $T = 0$. We study such systems here.

The intermediate-valence problem, and the possibility of the FK model having an instability to a spontaneously generated hybridization, was first proposed by Portengen *et al.* (1996a,b). Calculations in infinite-dimensions (Czychołł, 1999) and one dimension (Farkasovský, 1997, 1999) showed that a spontaneously generated hybridization was unlikely over a wide range of parameter space, but they did not rule out the possibility everywhere.

The first step to examining the intermediate-valence problem is to study the phase diagram of the FK model to see what different types of phases occur. We pick the spin-one-half model on the Bethe lattice again. We also pick $\rho_e + \rho_f = 1$ for the total electron concentration. Since the conduction electron fermi level is at 0 when there are no f -electrons, if we pick $-2 < E_f < 0$, then the fermi level is pinned to E_f at $U = 0$, and one of two

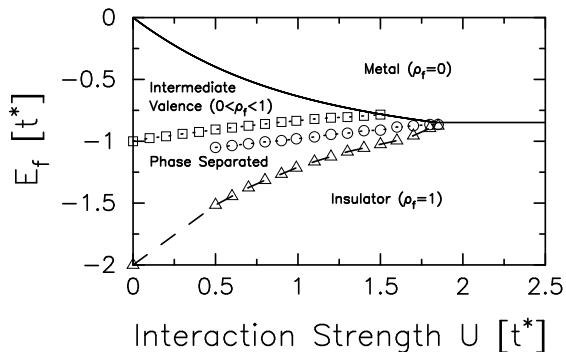


FIG. 16 Intermediate-valence phase diagram for the spin-one-half FK model on a Bethe lattice with $\rho_e + \rho_f = 1$. Note how the classical intermediate valence state occupies only a small part of the phase diagram, being taken over by phase-separated, metallic, and insulating phases over most of the phase diagram.

things can occur as U is increased: (i) either the classical intermediate-valence state survives, or (ii) it phase separates into a mixture of a state with $\rho_f = 0$ and $\rho_f = 1$. The former occurs for $E_f > -1$ and the latter for $E_f < -1$. As the interaction strength is increased further, then we find only two different stable solutions, a metallic phase, where $\rho_f = 0$ and an insulating phase where $\rho_f = 1$. The zero-temperature phase diagram is summarized in Fig. 16 (Chung and Freericks, 2000). In the phase-separated region, there are more possibilities: either the system remains phase separated in mixtures of two integer-valent states, or the phase separation has at least one intermediate-valence state in its mixture. The line of circles represents an approximate crossover line between these two possibilities (the intermediate-valence mixtures lie above the circles). Note how the metallic and insulator phases take over the phase diagram as U increases. In fact, the classical intermediate-valence state only occupies a small region of phase space, because it is unstable to phase separation over a wide region. This could explain why there are not too many classical intermediate-valence states seen in real materials.

We conclude this section with a discussion about the possibility for spontaneous hybridization (Zlatić *et al.*, 2001). We confine our discussion to the spinless model with $\rho_e + \rho_f = 0.5$ for simplicity. If we repeat the above analysis, then the region of stability for intermediate valence at small U is the same as above $-1 < E_f < 0$. But as U is increased, it appears that the intermediate-valence state should be stable for all U when $E_f = -0.75$ (but we have not performed a free-energy analysis to rule out the possibility of phase separation). We plot the inverse of the hybridization susceptibility from Eq. (135) in Fig. 17. Note that it remains finite for all T . But we can get an analytic form when $U = 0$ (Zlatić *et al.*, 2001), which says that the susceptibility has a term proportional to $|\ln T|$, which does diverge at $T = 0$. But this divergence does not guarantee that the ground state

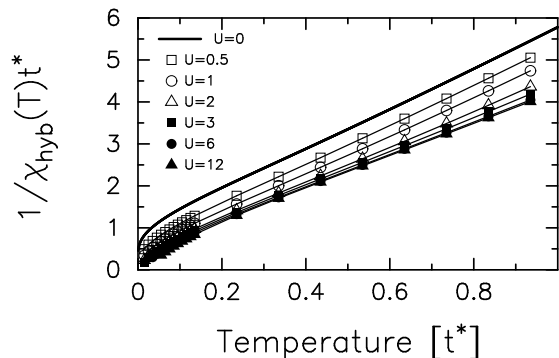


FIG. 17 Inverse of the hybridization susceptibility for the spinless FK model on a Bethe lattice with $\rho_e + \rho_f = 0.5$ and $E_f = -0.75$. Note how the susceptibility monotonically increases with increasing U which suggests that it continues to diverge at $T = 0$.

has spontaneous hybridization, in fact, it is known in this case that the ground state has $\langle c^\dagger f \rangle = 0$ (Farkasovský, 2002), even though the susceptibility diverges. Here we find, down to the lowest temperature that we can calculate, that the hybridization susceptibility increases with U , which would imply that it continues to diverge at $T = 0$ for all U . In this case, we do not know whether the ground state would possess a spontaneous hybridization, or not, but the results of Si *et al.* (1992) suggest that spontaneous hybridization is indeed possible. In any case, since a real material will always have a nonzero hybridization (although it may be quite small), one could expect a quantum-mechanical intermediate valence transition to occur at low temperature in regions of parameter space where the hybridization susceptibility is large for the FK model. Alternatively, spontaneous hybridization may also occur if the f -electrons are allowed to hop (Batista, 2002).

E. Transport Properties

The optical conductivity, calculated from Eq. (89), is plotted in Fig. 18, for the spinless FK model on the hypercubic lattice with $w_1 = 0.5$. Panel (a) is the half-filled case ($\rho_e = 0.5$) and panel (b) shows the behavior for doping away from half filling. Both calculations are at low temperature $T = 0.005$ in the homogeneous phase (ignoring any possible CDW phases).

At half filling, the data behaves as expected. For small U , the system has a Drude like peak, whose width is determined by the scattering rate at low temperature (note the scattering rate does not vanish even at $T = 0$ because the FK model is not a fermi liquid). As U increases, we see a charge-transfer peak develop, centered at $\nu \approx U$, and the low-energy spectral weight is suppressed because the system becomes a correlated (Mott-like) insulator (the metal-insulator transition occurs at $U \approx 1.5$ here). One can see that the transition is continuous, with σ_{dc}

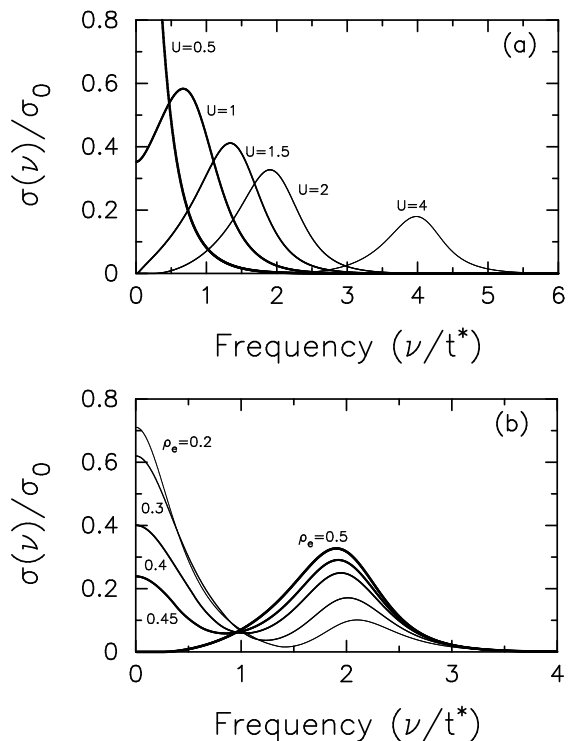


FIG. 18 Optical conductivity of the spinless FK model with $w_1 = 0.5$ on a hypercubic lattice at $T = 0.005$: panel (a) is the half filling case ($\rho_e = 0.5$) with different values of U and panel (b) is the $U = 2$ case doped away from half filling. The numbers in panel (a) label the value of U , while the numbers in panel (b) show ρ_e .

smoothly approaching zero as the correlations increase.

We concentrate on the $U = 2$ case as we dope away from half filling. One can see that as the system is doped, it becomes metallic, because the chemical potential now lies within the lower Hubbard band. As a result there is a transfer of spectral weight from the charge-transfer peak down to a Drude-like feature as the system is doped. What is remarkable, is that there is an isosbestic point present (which is defined to be a point where the optical conductivity is independent of doping and all the curves cross and typically occurs at $\nu \approx U/2$). The occurrence of such isosbestic points is present in a wide variety of models, but its origin is not well understood.

We also plot the dc-conductivity, thermopower, and electronic contribution to the thermal conductivity, as derived in Eqs. (93–98) for a correlated system ($U = 2$, solid line) with $\rho_e = 1 - w_1$ and five different w_1 values (Freericks and Zlatić, 2002b). For these parameters, there is always a region of exponentially small DOS near the chemical potential at low temperature [but in this region $\tau(\omega)$ decreases only as a power law]. As the localized electron concentration w_1 moves away from 0.5, the high-temperature thermopower increases in magnitude due to the asymmetry in the DOS (it must vanish at 0.5 due to particle-hole symmetry) and the low-temperature ther-

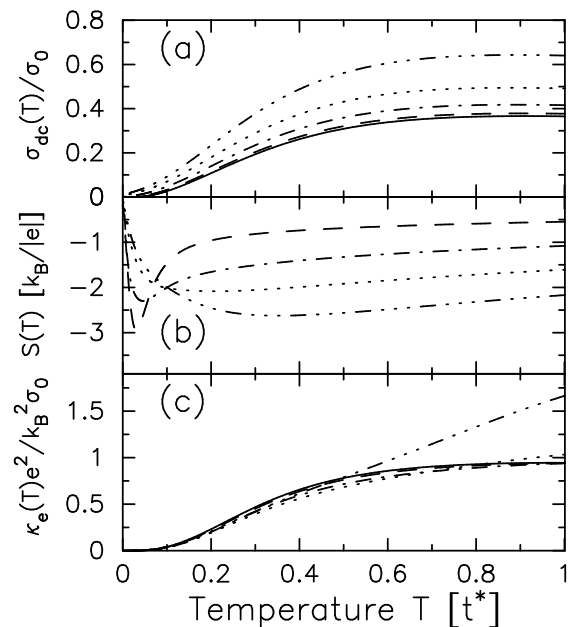


FIG. 19 (a) DC conductivity, (b) thermopower, and (c) electronic contribution to the thermal conductivity, for the spinless FK model with $\rho_e = 1 - w_1$ and $U = 2$. Five fillings are shown: (i) $w_1 = 0.5$ (solid line); (ii) $w_1 = 0.4$ (dashed line); (iii) $w_1 = 0.3$ (chain-dotted); (iv) $w_1 = 0.2$ (dotted); and (v) $w_1 = 0.1$ (chain-triple-dotted).

mopower shows a sharp peak for fillings close to half filling (the sign is hole-like, because the DOS from the lower Hubbard band dominates the transport coefficients at low temperature); the dc conductivity and thermal conductivity both vanish at low T due to the “gap” as well. The thermoelectric figure-of-merit $ZT = T\sigma_{dc}S^2/\kappa_{el}$ is plotted in Fig. 20—we find it is larger than one at high T for $w_1 < 0.22$, and for fillings close to half filling, there is a low-temperature spike in ZT that can become larger than one over a narrow temperature range. The spike at low T is due to the large peak in S and the small thermal conductivity; but the phonon contribution to the thermal conductivity can sharply reduce ZT if the phonon thermal conductivity is much larger than the electronic thermal conductivity (this all electronic calculation provides only an upper bound to ZT). The Lorenz number is also plotted in Fig. 20. It gets huge at half filling, but becomes more metallic ($\approx \pi^2/3$) as the filling moves further away from half filling. It is not a constant even at low temperature because the system is not a fermi liquid.

F. Magnetic-Field Effects

The magnetic field brings new features to the solution, which we illustrate for the model with a fixed total number of particles and relatively large Falicov-Kimball interaction on a hypercubic lattice. We restrict the number of f -particles per site to less than one, taking the

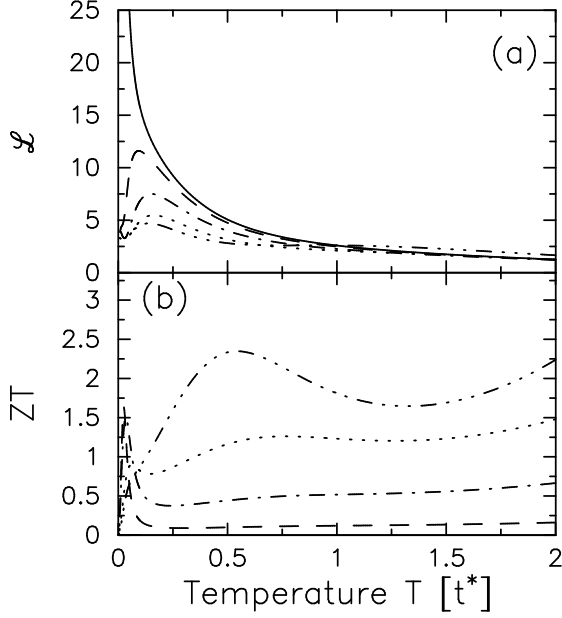


FIG. 20 (a) Lorenz number $\mathcal{L}k_B^2/e^2 = \kappa_{el}/\sigma_{dc}T$ and (b) electronic thermoelectric figure of merit $ZT = T\sigma_{dc}S^2/\kappa_{el}$ for the spinless FK model with $\rho_e = 1 - w_1$ and $U = 2$. Five fillings are shown: (i) $w_1 = 0.5$ (solid line); (ii) $w_1 = 0.4$ (dashed line); (iii) $w_1 = 0.3$ (chain-dotted); (iv) $w_1 = 0.2$ (dotted); and (v) $w_1 = 0.1$ (chain-triple-dotted).

limit $U^{ff} \rightarrow \infty$, and choose the position of the f -level such that there is a rather sharp crossover from the high-temperature state with a large concentration of f -electrons and a gap in the single particle DOS to the low-temperature state with a metallic conduction band (i.e., a fermi gas) and no f -electrons. That is, model parameters are such that the renormalized f -electron level is slightly above the chemical potential at $T = 0$. This is the regime that yields an anomalous magnetic response (Freericks and Zlatić, 1998) and is closely related to experimental materials like YbInCu_4 which exhibit a valence-change transition.

The average of the z-component of the f -electron magnetization is

$$\langle m_f^z \rangle = \text{Tr}_{cf} \frac{(e^{-\beta[\mathcal{H} - \mu N - \mu_f N_f]} m_f^z)}{\mathcal{Z}_L} \quad (137)$$

where only the states with one f -electron in the presence of the magnetic field are considered. This lattice trace can be evaluated by using the cavity method again, where the lattice trace becomes equal to an impurity trace in the presence of an additional time-dependent dynamical mean field

$$\langle m_f^z \rangle = \frac{\mathcal{Z}_{\text{cavity}}}{\mathcal{Z}_L} \text{Tr}_{cf} (e^{-\beta[\mathcal{H}_{\text{imp}} - \mu N - \mu_f N_f]} S(\lambda) m_f^z) \quad (138)$$

where $S(\lambda)$ is defined in Eq. (104). The trace is performed by using the basis set $|\eta\rangle$ which diagonalizes simultaneously \mathcal{H}_{imp} and m_f^z . Since m_f^z has no matrix

elements in the subspace without the f -particles and $\mathcal{Z}_{\text{imp}} = \mathcal{Z}_L/\mathcal{Z}_{\text{cavity}}$, we obtain

$$\begin{aligned} \langle m_f^z \rangle &= \frac{\prod_{\sigma=1}^2 \mathcal{Z}_{0\sigma}(\mu + g\mu_B H - U)}{\mathcal{Z}_{\text{imp}}} \\ &\times \sum_{\eta} \langle \eta | m_f^z | \eta \rangle e^{-\beta(E_{f\eta}(H) - \mu_f)} \\ &= \frac{\rho_f}{\mathcal{Z}_f} \sum_{\eta} \langle \eta | m_f^z | \eta \rangle e^{-\beta(E_{f\eta}(H) - \mu_f)}, \quad (139) \end{aligned}$$

where $\mathcal{Z}_f = \sum_{\eta} \exp[-\beta\{E_{f\eta}(H) - \mu_f\}]$ is the partition function of an isolated f -ion, $E_{f\eta}(H)$ are the field-dependent eigenstates, and $\mu_f = \mu$ is the common chemical potential for the itinerant and localized electrons. The average magnetization is the product of a single-ion response and the average f -filling $0 \leq \rho_f \leq 1$, i.e., the magnetic response of independent f -ions (Dzero, 2002; Dzero *et al.*, 2000, 2002) is modified by the interaction between the f -electrons and the conduction sea. This reduces the high-temperature Curie constant and introduces additional temperature and field dependences.

We illustrate these features for the spin-1/2 model ($s = S = 1/2$) and plot in Fig. 21 the temperature dependence of ρ_f as a function of various parameters (including the magnetic field). The results can be explained

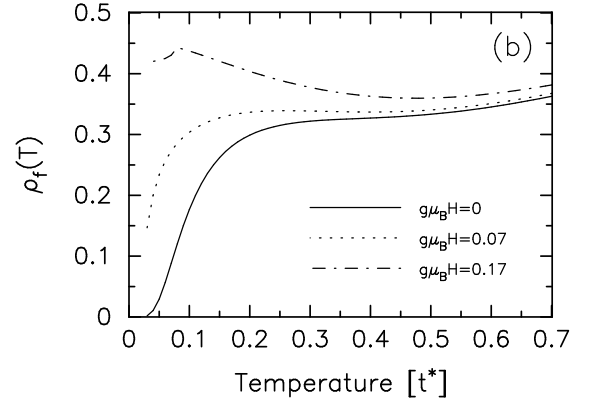


FIG. 21 The effect of the magnetic field on the f -electron concentration is shown for the spin 1/2 FK model with $\rho_{\text{total}} = 1.5$, $U = 3$, and $E_f = -0.5$, with $g\mu_B H = 0.07$ (dotted line) and $g\mu_B H = 0.17$ (chain-dotted line).

by noting that the renormalized f -level is just above the chemical potential and that a finite temperature induces an entropy driven “transition” (or crossover) into the magnetically degenerate state (the crossover temperature is denoted T_v). The field pushes the renormalized f -level closer to the chemical potential, which enhances the f -occupation, reduces the cross-over temperature and makes the transition sharper. For large enough fields, the concentration of f -electrons remains finite down to $T=0$, i.e., the system goes through a field-induced metamagnetic transition. This is shown in Fig. 22 where the magnetization obtained from Eq. (139) is plotted versus magnetic field for various temperatures. Below the

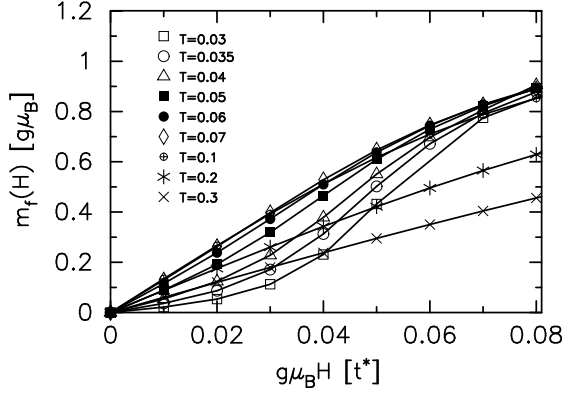


FIG. 22 Localized electron magnetization for the spin 1/2 FK model with $\rho_{total} = 1.5$, $U = 4$ and $E_f = -0.5$ plotted as a function of magnetic field for various values of temperature, as indicated in the figure.

crossover temperature, the low-field response is negligibly small (the Pauli susceptibility of the conduction electrons is neglected) but at large enough fields the magnetization curves go through an inflection point, which indicates a crossover to a magnetic state (and is a metamagnetic transition). Above the crossover, the curvature of the magnetization is positive and typical of a well-defined local moment. The effect of the magnetic field on transport properties is equally drastic. The magnetoresistance is plotted as a function of field in Fig. 23 and it shows that the low-temperature metallic state is destroyed above some critical field H_c . Thus, the metamagnetic transition in the f -subsystem is accompanied by metal-insulator transition in the conduction band. Taking the inflection point of the magnetization or the

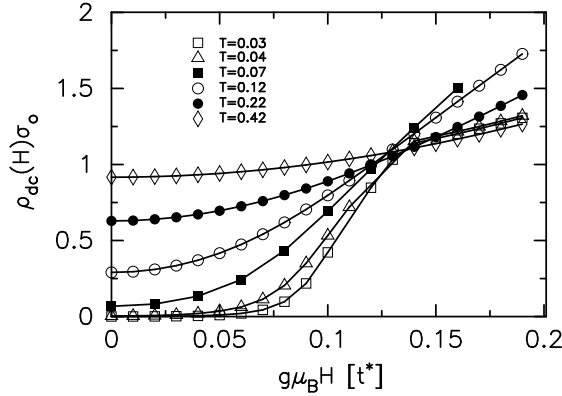


FIG. 23 Magnetoresistance as a function of magnetic field plotted for several values of temperature.

magnetoresistance, calculated for several values of U and E_f as an estimate of $H_c(T)$, we obtain the phase boundary which is shown in Fig. 24, together with the analytic form $H_c(T)/H_c(0) = \sqrt{1 - (T/T_v^*)^2}$. The crossover temperature is renormalized by $T_v^* = T_v/2$. Note that

the T_v^* values in Fig. 24 differ by more than an order of magnitude, while the ratio $k_B T_v^*/\mu_B H_c(0)$ is only weakly parameter dependent.

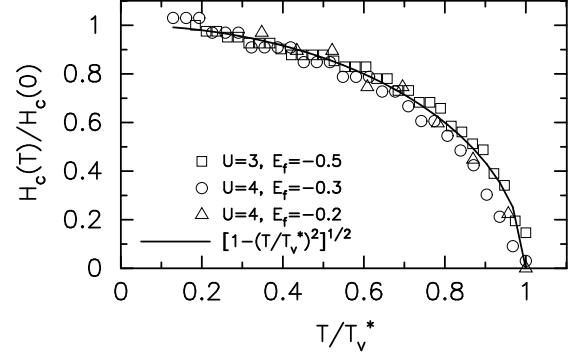


FIG. 24 Normalized critical field plotted as a function of reduced temperature T/T_v^* for several values of E_f and U . The solid line represents the analytic form $\sqrt{1 - (T/T_v^*)^2}$ with $T_v^* = T_v/2$.

G. Static Holstein Model

The static Holstein model (Holstein, 1959; Millis *et al.*, 1995, 1996) can be viewed as a generalization of the FK model to the continuous-spin case. Like the FK model, it also displays metal-insulator transitions and CDW order phase transitions. We discuss both possibilities here.

The phonon distribution function $w(x)$ in Eq. (39) becomes sharply peaked as $T \rightarrow 0$. If g_{ep} is small enough, it approaches $\delta(x)$, and the ground state is a noninteracting fermi gas (at half filling, the critical g_{ep} is 0.8432 on the hypercubic lattice and 1.0854 on the Bethe lattice). Beyond this critical value of g_{ep} , the phonon distribution function shows a double-peaked structure (becoming two delta functions at $T = 0$), and the “quasiparticles” scatter off of the local phonon even at $T = 0$. This creates a non-fermi-liquid state, and the DOS develops a pseudogap. As g_{ep} is increased further, the pseudogap phase becomes fully gapped (when the self energy develops a pole), and a metal-insulator transition takes place. These results are illustrated for the spin-one-half model on the hypercubic lattice in Fig. 25 [similar to what was done in Millis *et al.* (1996)].

The other area of interest is the CDW ordered phase at half filling. Since a static model does not superconduct, we need not worry about that order at all. One interesting puzzle in real materials is that the ratio of twice the CDW gap to the transition temperature is surprisingly large, usually much larger than the BCS prediction of 3.5 (Blawid and Millis, 2001). The CDW transition temperature can be calculated by performing ordered-phase calculations and extrapolating them to the point where the order disappears to produce T_c (Ciuchi and de Pasquale, 1999). These calculations

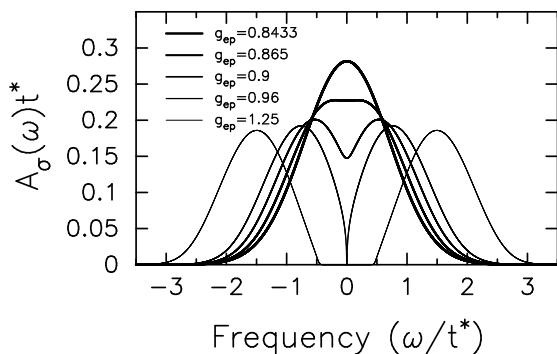


FIG. 25 Plot of the electronic DOS (per spin) for the harmonic static Holstein model at half filling on the hypercubic lattice at $T = 0$. Different values of g_{ep} have different thicknesses of the lines. Note how the metal-insulator transition is continuous here too.

show that even in the weak coupling limit, one finds a large ratio of $2\Delta/k_B T_c$. Since CDW systems involve a distortion of the lattice to produce the ordered phase, one expects that anharmonic terms may play an important role in describing the physics behind them. So it is important to also examine what happens in the presence of anharmonic interactions.

A surprising result was found when this system was analyzed on the hypercubic lattice. There was a universal scaling law for the transition temperature, when T_c was plotted against an extrapolated approximation to the wavefunction renormalization parameter (also called the quasiparticle Z factor, when one is in a fermi liquid), which is defined on the imaginary axis by

$$Z(0) = 1 - \frac{3}{2} \frac{\text{Im}\Sigma(i\pi T)}{\pi T} + \frac{1}{2} \frac{\text{Im}\Sigma(3i\pi T)}{3\pi T}. \quad (140)$$

The scaling law is plotted in Fig. 26 (a) (Freericks *et al.*, 2000). The results for T_c for a variety of coupling strengths and even for the case of quantum-mechanical phonons, all collapse onto the same curve. The results for an attractive Hubbard model (X symbols) do not, indicating that this scaling curve breaks down when the phonon frequency is made large enough.

The other quantity of interest to examine is the ratio of the CDW order parameter at $T = 0$ to the transition temperature. Since one might have expected the scaling theory for T_c would have produced a universal plot there, that result might not have been so surprising. But, when anharmonicity is included, its effects should be stronger at low temperature, since the phonon distortion won't be allowed to be as large in the anharmonic case, and hence one would naively expect a smaller order parameter. But, as shown in panel (b), we see that the ratio of $2\Delta/k_B T_c$ still satisfies an approximate scaling law when anharmonicity is included (Freericks and Zlatic, 2001a). Hence, one should expect, generically, that this ratio will be much larger than 3.5 except in extremely weak coupling cases (since it does approach 3.5 as $g_{ep} \rightarrow 0$).

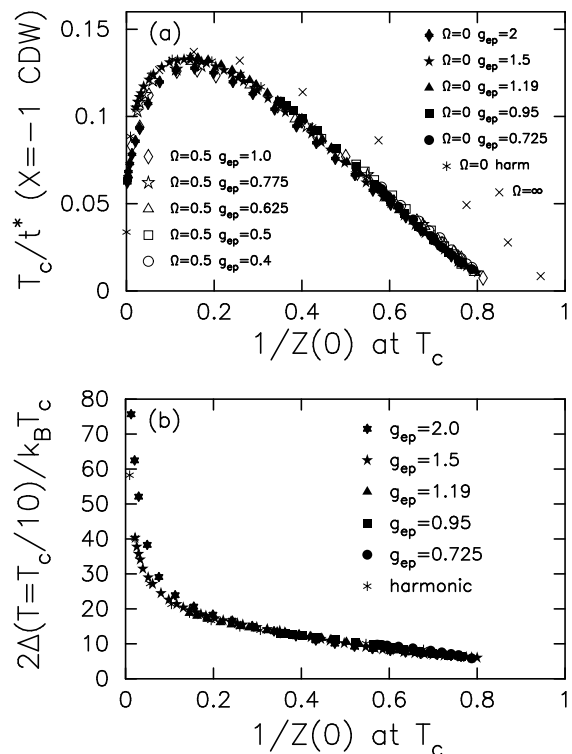


FIG. 26 Scaling plot of (a) the CDW transition temperature and (b) the CDW gap ratio versus the wavefunction renormalization extrapolated at T_c for the static Holstein model at half filling on the hypercubic lattice. In panel (a), we have also included some results for a quantum Holstein model, with a phonon frequency equal to 0.5, and for the attractive Hubbard model (which is the infinite-phonon-frequency limit).

IV. COMPARISON WITH EXPERIMENT

A. Valence-Change Materials

The FK model can be used to describe the anomalous features of rare earth intermetallic compounds that have an isostructural valence-change transition, as observed in the YbInCu_4 and $\text{EuNi}_2(\text{Si}_{1-x}\text{Ge}_x)_2$ family of compounds. These intermetallics have been attracting a lot of attention recently (Felner and Novik, 1986; Figueroa *et al.*, 1998; Garner *et al.*, 2000; Levin *et al.*, 1990; Sarrao, 1999; Wada *et al.*, 1997; Zhang *et al.*, 2002) and we describe the most typical features briefly.

The temperature-dependent properties of YbInCu_4 , which have been studied most thoroughly and which we take as our example, are dominated at ambient pressure by a first-order valence-change transition at about 40 K. The valence of Yb ions changes abruptly from Yb^{3+} above the transition temperature, T_v , to $\text{Yb}^{2.85+}$ below T_v (Dallera *et al.*, 2002; Felner and Novik, 1986). The specific heat data shows at T_v a first-order transition with an entropy change of about $\Delta S \simeq R \ln 8$ corresponding to a complete loss of magnetic degeneracy in the ground state (Sarrao, 1999). Neutron scattering

does not provide any evidence for long-range order below T_v (Lawrence *et al.*, 1997). At the transition, the f -occupation becomes non-integral (Dallera *et al.*, 2002) and the lattice expands by about 5%. The crystal structure remains in the C15(b) class and the volume expansion estimated from the known atomic radii of Yb^{3+} and Yb^{2+} ions is compatible with the valence change estimated from the L_{III} -edge data (Cornelius *et al.*, 1997; Felner and Novik, 1986).

The low-temperature phase shows anomalies typical of a valence-fluctuating intermetallic compound. The electronic specific heat and the susceptibility are enhanced (Sarraf, 1999), the electrical resistance and the Hall constant are small and metallic, and the low-temperature slope of the thermoelectric power is large (Očko and Sarraf, 2002). The optical conductivity is Drude like, with an additional structure in the mid-infrared range which appears quite suddenly at T_v (Garner *et al.*, 2000). The ESR data (Rettori *et al.*, 1997) indicate a large density of states at the Fermi level E_F . Neither the susceptibility, nor the resistivity, nor the Hall constant show any temperature dependence below T_v , i.e., the system behaves as a Fermi liquid with a characteristic energy scale $T_{FL} \gg T_v$. The magnetic moment of the rare earth ions is quenched in the ground state by the $f-d$ hybridization but the onset of the high-entropy phase cannot be explained by the usual Anderson model in which the low- and high-temperature scales are the same and the spin degeneracy is not expected to be recovered below T_{FL} . The valence-change systems, however, recover the f -moment at T_v which is a much lower temperature than T_{FL} .

The high- T phase of YbInCu_4 sets in at T_v and is also anomalous. The Yb ions are in the stable 3+ configuration with one f -hole and with the magnetic moment close to the free ion value $g_L \sqrt{J(J+1)} \mu_B = 4.53 \mu_B$ ($g_L = 8/7$ is the Landé factor and $J = 7/2$ is the total angular momentum of the $4f^{13}$ hole). The magnetic response is Curie-Weiss like with a small Curie-Weiss temperature Θ , which does not seem to be connected with T_v in any simple way (Felner and Novik, 1986; Sarraf, 1999) (of course one does not expect a first-order transition temperature to be related to the Curie-Weiss temperature, but this observation shows that the two phenomena are not governed by the same microscopic physics). The dynamical susceptibility obtained from neutron scattering data (Goremychkin and Osborn, 1993) is typical of isolated local moments, with well resolved crystal-field excitations (Murani *et al.*, 2002). However, neither the line shape of the dynamical response nor the temperature dependence of the static susceptibility can be explained by the Kondo model assuming $T_K \simeq T_v$. The Hall constant is large and negative, typical of a semi-metal (Figueroa *et al.*, 1998), the electrical resistance is also very large and not changed much by magnetic field up to 30 T (Immer *et al.*, 1997). In typical Kondo systems, on the other hand, one expects a logarithmic behavior on the scale T/T_K and large negative mag-

netoresistance. The high temperature optical conductivity (Garner *et al.*, 2000) shows a pronounced maximum of the optical spectral weight at a charge-transfer peak near 1 eV and a strongly suppressed Drude peak. The high-temperature ESR data for Gd^{3+} embedded in YbInCu_4 resemble those found in integer-valence semi-metallic or insulating hosts (Altshuler *et al.*, 1995).

The anomalous properties of the high-temperature phase become most transparent if the valence-fluctuating phase is suppressed completely by pressure or doping as in $\text{Yb}_{1-x}\text{Y}_x\text{InCu}_4$, where a substitution of 15% Y ions stabilizes the high-temperature phase down to $T=0$ K (Mitsuda *et al.*, 2002; Očko and Sarraf, 2002; Zhang *et al.*, 2002). The experimental results for the resistivity, susceptibility and the thermopower (Očko and Sarraf, 2002) are shown in Fig. 27. The susceptibility data show that the Curie-Weiss temperature for all the samples is about the same and much less than T_v , i.e., the magnetic response of the high-temperature phase can be represented by a single universal curve, provided one scales the data by an effective concentration of magnetic f -ions, ρ_f , which is always smaller than the nominal concentration of f -ions. The functional form of the susceptibility above 10 K agrees well with the “single-ion” crystal field (CF) theory. At lower temperatures the susceptibility deviates appreciably from the CF theory and shows a significant reduction of the Curie constant ρ_f which is not of the Kondo type.

The resistivity in the high-temperature phase of $\text{Yb}_{1-x}\text{Y}_x\text{InCu}_4$ exhibits a weak maximum and the thermopower has a minimum above 100 K but neither quantity shows much structure at low temperatures, where the susceptibility drops below the single-ion CF values. That is, despite the presence of the well-defined local moments, there are no Kondo-like anomalies in transport or thermodynamic properties of the high-temperature phase. On general grounds, one can argue that the discontinuity of the thermoelectric power at the valence transition is a trivial consequence of the different thermoelectric properties of the two phases: the thermopower of the valence-fluctuating phase has an enhanced slope and grows rapidly up to T_v , where it suddenly drops to the values characteristic of the high-temperature phase.

The hydrostatic pressure, doping and the magnetic field also have, like the temperature, a strong effect on the properties of the valence-change materials. The critical temperature of YbInCu_4 decreases with pressure (Immer *et al.*, 1997) but the data are difficult to explain with the Kondo volume collapse model (Sarraf, 1999). Doping the Yb sites with Y^{3+} or Lu^{3+} ions reduces T_v despite the fact that Y has a bigger and Lu a smaller ionic radius (Zhang *et al.*, 2002); doping the In sites by smaller Ag ions enhances T_v as in $\text{YbIn}_{1-x}\text{Ag}_x\text{Cu}_4$ for $x \leq 0.3$ (Cornelius *et al.*, 1997; Lawrence *et al.*, 1999). Thus, doping cannot be explained in terms of a chemical pressure. The low-temperature phase is easily destabilized by an external magnetic field: a critical field $H_c(T)$ induces a meta-

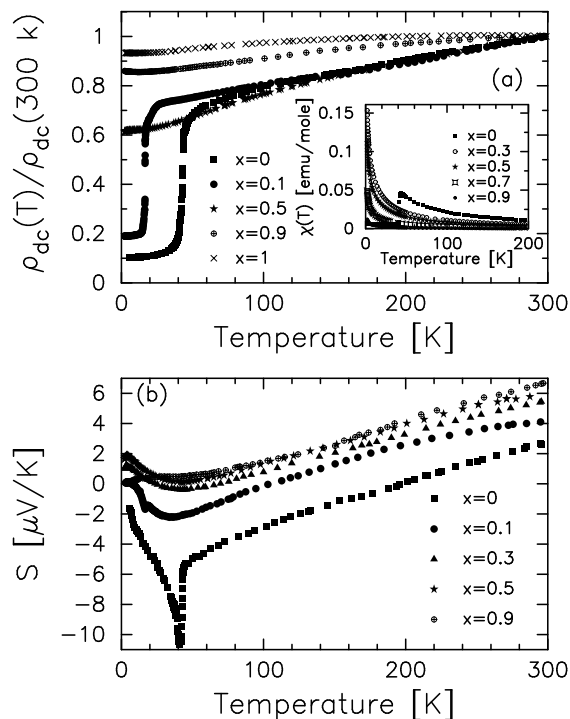


FIG. 27 Panel (a) shows the resistivity and the magnetic susceptibility of $\text{Yb}_{1-x}\text{Y}_x\text{InCu}_4$ as functions of temperature for various concentrations of Y ions (Očko and Sarrao, 2002). Note, all the “high-temperature” data can be collapsed onto a single universal curve, by normalizing the susceptibility with respect to an effective Yb-concentration (not shown). Panel (b) shows the thermopower of $\text{Yb}_{1-x}\text{Y}_x\text{InCu}_4$ as a function of temperature for various concentrations of Y ions (Očko and Sarrao, 2002).

magnetic transition which is clearly seen in the magnetoresistance and the magnetization data. The experimental values of $H_c(T)$ define the $H - T$ phase boundary and the analysis of many systems with different T_v^0 (zero-field transition temperature) and $H_c(0)$ (zero-temperature critical field) reveal the following universal behavior: $H_c(T) = H_c(0)\sqrt{1 - (2T/T_v^0)^2}$. Despite the differences in T_v and H_c , the data give a constant ratio $k_B T_v^0 / \mu_B H_c(0) = 1.8$.

In summary, the Yb systems switch at the valence-change transition from a low-entropy valence-fluctuating phase to a high-entropy magnetic semi-metallic phase. The transition is accompanied by the transfer of holes from the conduction band to the 4f shell and a metal-insulator transition (or crossover). The high-temperature phase has degenerate local moments which interact with the conduction band (and, hence, get reduced) but the interaction is not of the usual Kondo type and no logarithmic anomalies are seen. Such a behavior can be qualitatively understood by assuming that (i) the chemical potential of the metallic phase is close to the location of the dip or gap in the DOS, which arises from many-body interactions, and that (ii) the energy of the localized

magnetic configuration is above the non-magnetic one as $T \rightarrow 0$. The metallic phase is destabilized by magnetic fluctuations when the entropy gain due to additional (localized) magnetic states overcomes the energy loss due to the change of the ionic configuration and the entropy loss due to the reduction of the number of holes in the conduction band. Once the chemical potential is brought close enough to the band edge, by doping, pressure, temperature or magnetic field, the entropy of the band states is suppressed and the magnetic entropy of the localized states becomes sufficient to compensate the energy loss and destabilize the metallic phase. This behavior is observed in many systems and it is not likely to be due to band-structure effects alone. Rather, the gap or pseudo-gap which is a necessary ingredient of the above scenario seems to be due to many-body interactions.

The valence-change transition is also found in many Eu-based systems, and $\text{EuNi}_2(\text{Si}_{1-x}\text{Ge}_x)_2$ (Wada *et al.*, 1997) provides a typical and well-studied example. The thermodynamic anomalies are similar as in Yb systems but the transition temperature is higher and Eu ions undergo an almost complete valence change between the high-temperature, f^7 and the low-temperature f^6 configuration. That is, the transition is from a free-spin system at high temperatures to a simple metal at low temperatures. The electron transport is similar as in YbInCu_4 but the intrinsic data are more difficult to measure because the volume change at the transition is large and samples typically crack when thermally cycled. In $\text{EuNi}_2(\text{Si}_{1-x}\text{Ge}_x)_2$ (Sakurai *et al.*, 2000) the sign of the thermopower is reversed with respect to Yb systems, which indicates an electron-like rather than hole-like transport.

The high-temperature behavior of YbInCu_4 and $\text{EuNi}_2(\text{Si}_{1-x}\text{Ge}_x)_2$ -like compounds can be well described by the FK model (Freericks and Zlatić, 1998; Zlatić and Freericks, 2001b, 2003; Zlatić *et al.*, 2001). We describe the f -ions by two energetically close configurations which differ in their f -count by one, we take a common chemical potential for the conduction and localized electrons (which is adjusted at each temperature to conserve the total number of electrons), we take the FK Coulomb repulsion between the conduction electrons (or holes) and the additional f -electron (or hole) large enough to open a gap in the conduction band. For realistic modeling we should also take into account the actual crystal-field structure including the splittings and the degeneracy of the ionic energy levels. For Yb ions, the state with no f -holes has unit degeneracy, while the single-hole case has a degeneracy of 8 (corresponding to $J = 7/2$). The two-hole case is forbidden due to the mutual repulsion of two holes being too large. The 8-fold degeneracy of a single f -hole is further reduced by CF splittings and in a cubic environment we expect 4 doublets (unless there is some accidental degeneracy). The external field further splits these CF states. For Eu ions, we take into consideration the $4f^6$ (3^+) configuration with a non-magnetic ground state and two excited magnetic states, and the

magnetic $4f^7$ (2^+) configurations. Since these states are pure spins states, there are Zeeman splittings but no CF splittings. All other states of Eu ions are higher in energy and neglected.

To find the thermodynamic and transport properties we need the weights of the ionic $4f$ configurations, i.e. we need the partition function of a more general FK model. Since the trace over f states still separates into a sum over the states which differ by one f -electron, the end result can be written as,

$$\mathcal{Z}_{imp} = \mathcal{Z}_{n_f^0} \prod_{\sigma} \mathcal{Z}_{0\sigma}(\mu) + \mathcal{Z}_{n_f^0 \pm 1} \prod_{\sigma} \mathcal{Z}_{0\sigma}(\mu - U) \quad (141)$$

where $\mathcal{Z}_{0\sigma}(\mu)$ is defined by Eq. (24) and $\mathcal{Z}_{n_f^0}$ and $\mathcal{Z}_{n_f^0 \pm 1}$ are the partition functions of an isolated f -ion with n_f^0 and $n_f^0 \pm 1$ f -electrons, respectively. In the case of Yb ions, the $n_f^0 = 14$ configuration is non-magnetic, such that $\mathcal{Z}_{n_f^0=14} = 1$, and the $n_f^0 - 1$ configuration has one magnetic hole in the $J = 7/2$ spin-orbit state, such that the partition function becomes,

$$\mathcal{Z}_{n_f^0=13} = \sum_{\eta=1}^8 e^{-\beta[E_{f\eta}(H) - \mu_f]}. \quad (142)$$

The excitation energies $E_{f\eta}(H)$ of a single magnetic hole are split into multiplets belonging to different irreducible representations of the crystal.

In the case of Eu ions, the f^6 configuration has a non-magnetic ground state and two magnetic $S = 1$ and $S = 2$ excitations. Assuming the usual Zeeman coupling with the magnetic field gives the ionic partition function,

$$\begin{aligned} \mathcal{Z}_{n_f^0=6} = & 1 + e^{-\beta E_{S=1}} \sum_{m=-1}^1 e^{-\beta g\mu_B H m} \\ & + e^{-\beta E_{S=2}} \sum_{m=-2}^2 e^{-\beta g\mu_B H m}. \end{aligned} \quad (143)$$

The f^7 configuration is the magnetic Hund's rule state ($S = 7/2$) and its partition function is simply

$$\mathcal{Z}_{n_f^0=7} = e^{-\beta E_{S=7/2}} \sum_{m_s=-7/2}^{7/2} e^{-\beta[g\mu_B H m_s - \mu_f]}. \quad (144)$$

The weights of the two ionic configurations are given by

$$w_0 = \frac{\mathcal{Z}_{n_f^0}}{\mathcal{Z}_{imp}} \prod_{\sigma} \mathcal{Z}_{0\sigma}(\mu) \quad (145)$$

and

$$w_1 = \frac{\mathcal{Z}_{n_f^0 \pm 1}}{\mathcal{Z}_{imp}} \prod_{\sigma} \mathcal{Z}_{0\sigma}(\mu - U) \quad (146)$$

which enter the Green's function formalism.

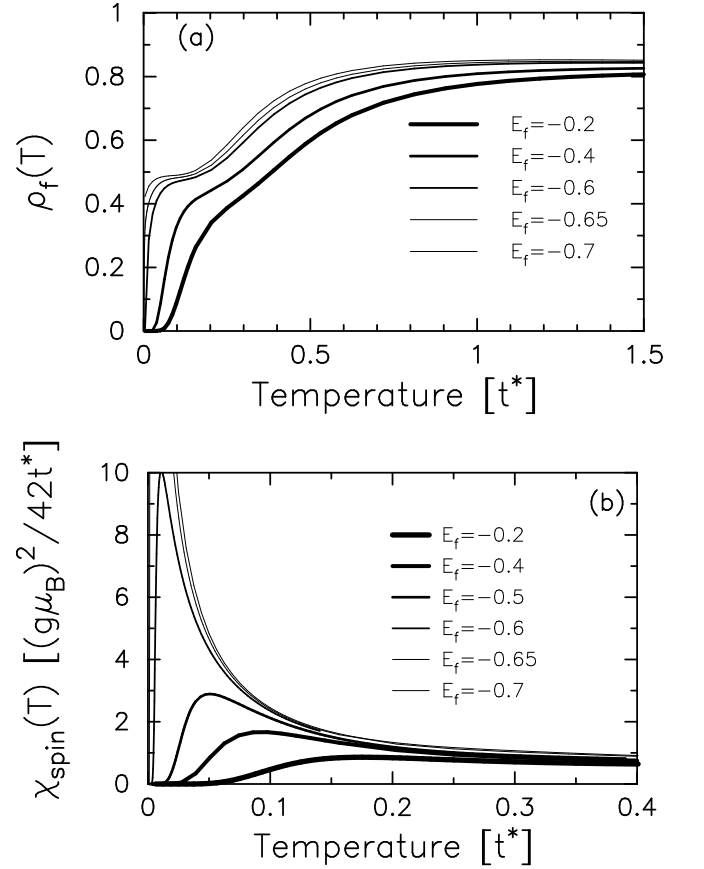


FIG. 28 (a) Localized electron filling and (b) normalized spin susceptibility for eightfold degenerate ($S = 7/2$) Falicov-Kimball model with $\rho_{total} = 1.5$, $U = 2$, and various E_f .

In what follows, we discuss a case that is similar to that of Yb: the case of an $S = 7/2$ magnetic particle in the high-temperature phase and of a magnetically inert unoccupied state in the low-temperature phase; we neglect CF splitting but do consider Zeeman splitting. The generalization to Yb ions with the magnetic f^{13} states split by the cubic CF, or to Eu ions with excited magnetic states in the low-temperature f^6 configuration, is straightforward. We choose the Coulomb repulsion to be $U = 2$, which is large enough to open a small gap in the interaction DOS (see below) and we tune the bare f -level to bring the renormalized f -level slightly above the chemical potential. Thus, at $T = 0$, there are no f -electrons in the ground state but as T increases, the f -occupancy increases, producing a local-moment response. Since the filling of the f electrons is entropically driven, the filling increases rapidly with T as the degeneracy increases. In Fig. 28, we plot the average f -occupation and the spin susceptibility (normalized by the total m_z^2 which equals 42 for spin-seven-halves). Panel (a) of Fig. 28 shows that as E_f is reduced, the high temperature value of ρ_f increases, the “transition temperature” decreases, and the transition becomes sharper. Panel (b) shows the spin sus-

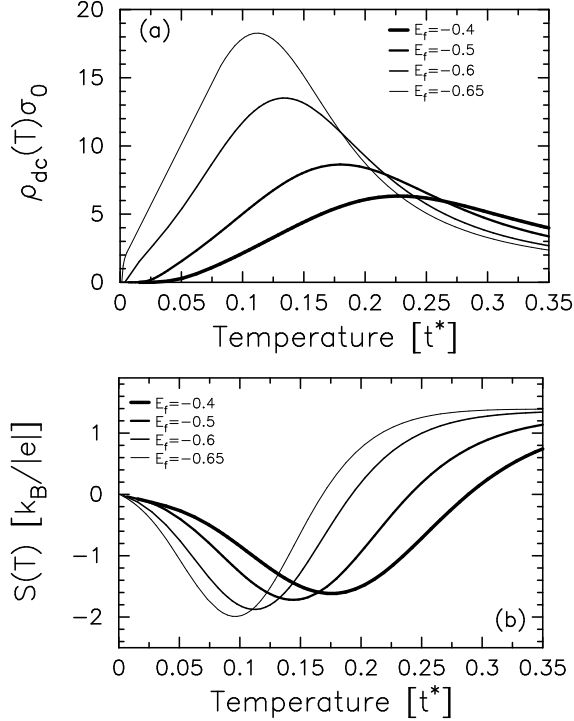


FIG. 29 (a) DC resistivity and (b) thermopower for the ($S = 7/2$) Falicov-Kimball model with $\rho_{\text{total}} = 1.5$ and $U = 2$. The different curves correspond to different values of E_f .

ceptibility, which is Curie-like but with a temperature-dependent concentration of local f -moments. Hence it has a peaked form, with a sharp reduction of the magnetic response as $T \rightarrow 0$. Defining T_v as the temperature at which the spin susceptibility drops to half of the maximum value, we find $T_v = 0.05, 0.03, 0.007$ and 0.001 for $E_f = -0.4, -0.5, -0.6$, and -0.65 , respectively. In all these cases we are dealing with a crossover rather than a sharp phase transition. In the case $E_f = -0.2$ the peak is too broad for the transition to be defined, and for $E_f = -0.7$ the occupation of f -states remains finite down to lowest temperatures. A first-order phase transition is possible for E_f between -0.65 and -0.7 but details of this transition cannot be obtained by the iterative numerical procedure, which becomes unstable. The effect of the f -level position on transport properties is shown in Fig. 29. Panel (a) shows that the resistivity has a maximum at an effective temperature T^* which is much larger than T_v and that the peak sharpens and moves to somewhat lower temperatures as E_f is reduced. Effects at T_v are not visible, except for $E_f = -0.65$, which lies close to the first-order transition. The thermopower results shown in panel (b) are somewhat similar, except that the transition at T_v cannot be detected. In addition, there is a sign change in S that occurs at higher temperature. The transport anomalies are due to the development of a gap and the renormalization of the single-particle DOS at high temperature, driven by the increased f -electron

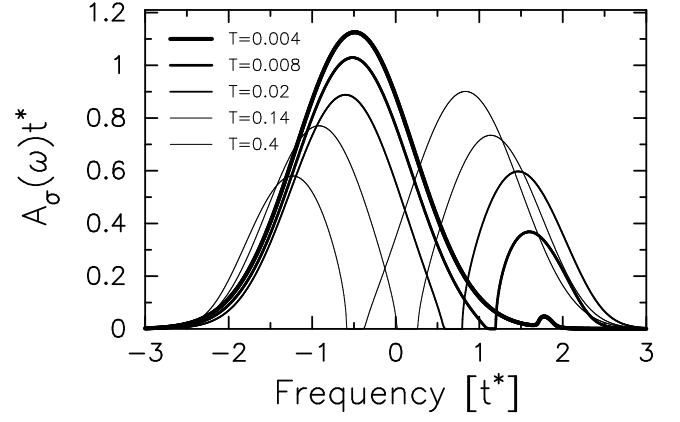


FIG. 30 Interacting DOS for the ($S = 7/2$) Falicov-Kimball model with $\rho_{\text{total}} = 1.5$, $U = 2$, $E_f = -0.6$ and for various temperatures.

occupation and the Falicov-Kimball interaction.

The theoretical results shown in Figs. 28 and 29, obtained for $\rho_{\text{total}} = 1.5$, $U = 2$ and E_f close to -0.6 , exhibit most of the qualitative features seen in the experimental data. However, the model parameters and the absolute value of the temperature scale used for the static response functions cannot be determined unless one compares the dynamic properties of the model to experimental data.

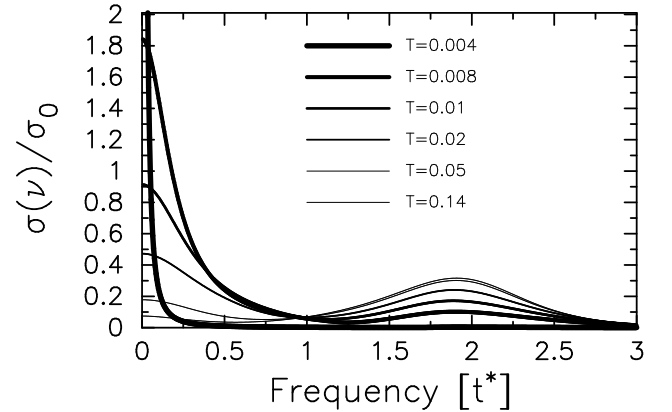


FIG. 31 Optical conductivity for the ($S = 7/2$) Falicov-Kimball model with $\rho_{\text{total}} = 1.5$, $U = 2$, $E_f = -0.6$, and for various temperatures.

The interacting conduction DOS is plotted in Fig. 30 as a function of frequency, for the case $\rho_{\text{total}} = 1.5$, $U = 2$, $E_f = -0.6$, and for various temperatures. Note, the temperature-induced shift in the chemical potential from the metallic region, with a high density of states, into the gap-region. Unfortunately, direct comparison with the photoemission spectra is not possible because the bulk and surface effects in valence-fluctuating systems are difficult to separate.

Fig. 31 shows the optical conductivity. We find a characteristic high-frequency hump at $\nu = U$, which is almost E_f -independent, and a temperature-induced transfer of spectral weight between the high- and low-frequency regions. A Drude peak grows as $\nu \rightarrow 0$ for $T \leq T_v$. Thus, while the static transport is dominated by a pseudo-gap on the order of T^* , the optical conductivity is sensitive to the valence-change transition. The high-frequency peak in $\sigma(\nu)$ allows an estimate of the value of the FK Coulomb interaction, yielding $U \approx 1$ eV (Garner *et al.*, 2000) for YbInCu₄. Using $T_v = 42$ K we find $U/T_v \approx 250$ which can be used to narrow the choice of the model parameters. The experimental features can be reproduced by taking the f -level position at $E_f = -0.6$ but the procedure is not completely unique, because U/T_v is not independent of the total number of particles. As an additional constraint on the parameters one should demand that the theory reproduces the peaks in the high-temperature transport properties in the right temperature range. Clearly, a proper quantitative description should also incorporate the CF splittings of $J=7/2$ Yb states, which would provide the field-induced anisotropies of the magnetization. This has not yet been worked out in detail for either the Yb or Eu compounds.

B. Electronic Raman Scattering

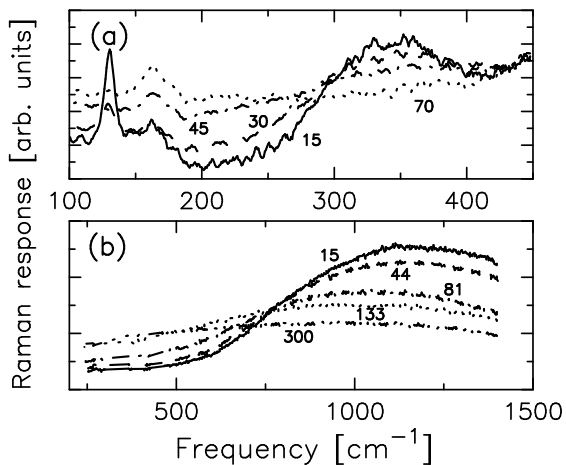


FIG. 32 Experimental Raman scattering results for (a) SmB₆ (Nyhus *et al.*, 1995b, 1997) and (b) FeSi (Nyhus *et al.*, 1995a). The labels mark the different temperatures.

Experimental Raman scattering data on a wide variety of different correlated insulators shows three distinctive features: (i) as the temperature increases, there is a sudden transfer of spectral weight from a high-energy charge-transfer peak to lower energies; (ii) there is an isosbestic point, where the Raman response is independent of temperature at a special frequency, and all Raman scattering curves cross; and (iii) if one takes the ratio of twice

the spectral range where spectral weight is depleted at low temperature (representative of the insulating gap) to the temperature at which the low-energy spectral weight is restored (representative of T_c), then $2\Delta/k_B T_c \gg 3.5$. These features are shown in Fig. 32 where we plot the Raman response for (a) SmB₆ (Nyhus *et al.*, 1995b, 1997) and (b) FeSi (Nyhus *et al.*, 1995a).

Using the results of Tables VI and VII at $X = 1$ allows us to calculate the Raman response in the A_{1g} and B_{1g} channels. Since the Raman response ultimately is a complicated functional of the interacting density of states, and since all insulators have the same qualitative feature of a gap near the chemical potential, we expect the Raman response to depend only weakly on the microscopic features of the insulating phase. Hence, we perform our calculations for the simplest possible system that goes through a Mott-like metal-insulator transition: the spinless FK model at half filling ($\rho_e = w_1 = 0.5$) on a hypercubic lattice (Freericks and Devereaux, 2001a,b; Freericks *et al.*, 2001a).

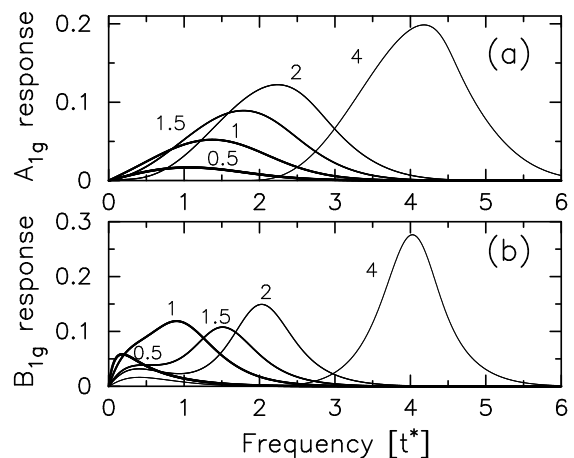


FIG. 33 Theoretical calculation of the nonresonant Raman response in the (a) A_{1g} channel and the (b) B_{1g} channel at $T = 0.5$ and for various values of U .

We begin with a plot of the Raman response at fixed temperature $T = 0.5$ and for a variety of values of U in the two symmetry channels (Fig. 33). Note how for weak correlations we have a linear onset, and a higher-energy cutoff (from the band) as expected. As the correlations increase, we see the response separates into a charge-transfer peak centered at U and a low-energy peak (in the B_{1g} sector only). The vertex corrections in the A_{1g} sector suppress the low-energy features and we simply see the evolution of the charge-transfer peak, which is more asymmetric in shape.

We choose to examine the inelastic light scattering for $U = 2$ in more detail, because it is a correlated insulator that lies close to the metal-insulator transition. We plot in Fig. 34 the inelastic X-ray scattering response function along the zone diagonal for a variety of different temperatures (Devereaux *et al.*, 2003). The response at

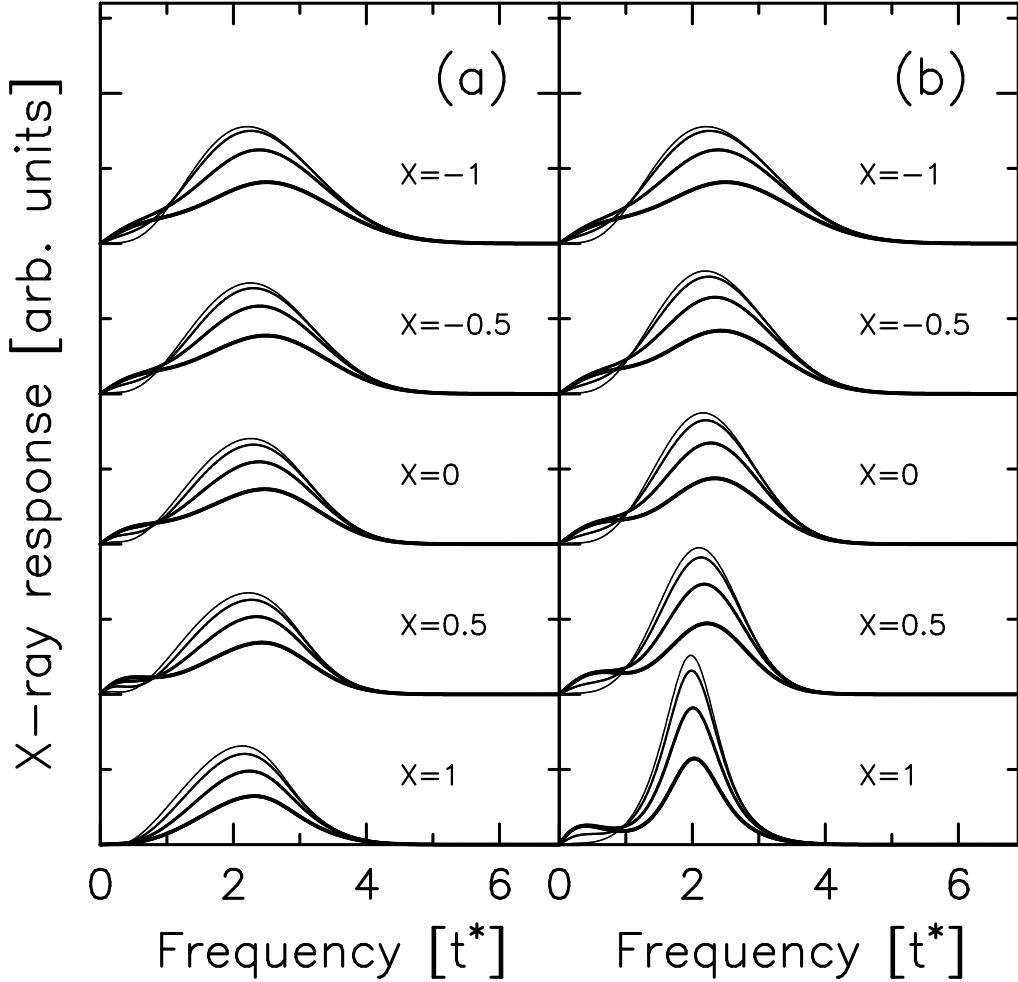


FIG. 34 Theoretical calculation of nonresonant inelastic X-ray scattering in the (a) A_{1g} channel and the (b) B_{1g} channel for $U = 2$ along the zone diagonal for a range of different temperatures. The thickness of the lines determines the temperature which ranges from 1.0 to 0.5 to 0.25 to 0.1. The individual curves for different X values have been shifted for clarity. The $X = 1$ curves correspond to conventional electronic Raman scattering.

the zone center is the Raman response. We find that it displays all of the three features seen in experiment: (i) there is a low-temperature depletion of low-energy spectral weight, (ii) there is an isosbestic point, and (iii) the ratio of $2\Delta/k_B T_c$ (as extracted from the Raman response curves) is on the order of 10–20. These three features are generic to the plots at all X , except for $X = 1$ in the A_{1g} sector, where the low-energy spectral weight disappears. This occurs because the finite- \mathbf{q} vector mixes the different symmetries and the low-energy spectral weight is seen in the other symmetries. Note that the results are independent of symmetry channel for $X = -1$, which makes for the possibility of an interesting experimental probe of nonlocal correlations. In general, we see a small amount of dispersion of the peaks and a generic broadening of the peaks as we move from zone center to zone boundary, but the isosbestic behavior remains for all \mathbf{q} . So far resonant inelastic X-ray scattering experiments have

been performed mainly at room temperature and with polarizers only on the incident beam of light, so direct comparison with theory is not yet feasible.

C. Josephson Junctions

Another area where the FK model has been applied to real materials is in the field of Josephson junctions [see Freericks *et al.* (2002c) for a review]. A Josephson junction is a sandwich of two superconductors surrounding a barrier material that can be a normal metal, an insulator, or something in between (Josephson, 1962). In rapid single flux quantum (RSFQ) logic (Likharev, 2000), one tries to maximize the switching speed of the Josephson junction, while maintaining a nonhysteretic (single-valued) $I - V$ characteristic. Since the integral of a voltage pulse over time is equal to a flux quantum for a Josephson junction, the height of the voltage pulse is in-

versely proportional to the width of the pulse; hence one wants to maximize the characteristic voltage to achieve the fastest switching speeds. The characteristic voltage is a product of the critical current at zero voltage I_c with the normal-state resistance R_n (slope of the $I - V$ characteristic at high voltage).

In conventional tunnel junctions, the barrier material is an insulator, so I_c is low and R_n is high; in proximity-effect junctions, the barrier material is a normal metal, so I_c is high and R_n is low. Is it possible that one can maximize the product of $I_c R_n$ by choosing a material to lie close to the metal-insulator transition, where both I_c and R_n can be large? We can examine this question by describing the barrier material with the spin-one-half FK model on a cubic lattice in the local approximation with $w_1 = 0.5$ and $\rho_e = 1$. This system has a metal-insulator transition in the bulk at $U \approx 4.9t$. To simulate the properties of a Josephson junction, we must solve an inhomogeneous DMFT problem as first done by Potthoff and Nolting (1999) and generalized to the superconducting state by Miller and Freericks (2001). Using the FK model to describe the barrier material was performed in Freericks *et al.* (2001b, 2003) and has been reviewed elsewhere (Freericks *et al.*, 2002c).

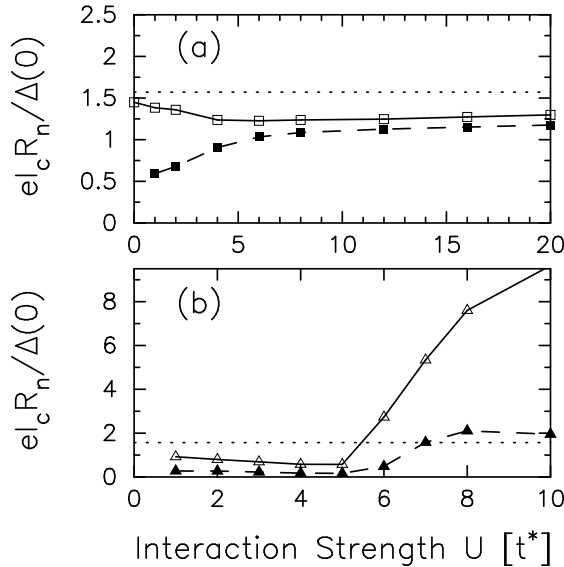


FIG. 35 Figure of merit as a function of the FK correlation strength in a Josephson junction with a barrier of (a) one and (b) five planes. The dotted line is the Ambegaokar-Baratoff prediction for an ideal tunnel junction. The plots are at two temperatures $T = T_c/11$ (open symbols) and $T = T_c/2$ (filled symbols). $\Delta(0)$ is the superconducting gap at $T = 0$.

In Fig. 35, we plot the figure of merit $I_c R_n$ versus U for two cases: (a) a single-plane barrier and (b) a five-plane barrier. Notice how the $I_c R_n$ is maximized in a ballistic metal for $N = 1$ at low T , but then is maximized in the tunnel junctions as T increases. The flatness of the curves in panel (a) for $U > 5$ is a verification of the Ambegaokar and Baratoff (1963) analysis which

says $I_c R_n$ is independent of the properties of the barrier for thin tunnel junctions. Our result is somewhat lower than the Ambegaokar-Baratoff prediction due to fermi-surface effects, proximity and inverse proximity effects, etc. What is interesting is that in panel (b) there is a marked increase in the figure of merit at low temperature near the metal-insulator transition. Indeed, we find $I_c R_n$ is maximized on the insulating side of the metal-insulator transition, and the optimization remains for a wide range of temperature (the reduction in $I_c R_n$ arises mainly from the temperature dependence of R_n for a correlated insulator). These results are consistent with experiments performed on junctions made out of NbTiN for the superconductor and Ta_xN for the barrier (Kaul *et al.*, 2001). As tantalum is removed from TaN, it creates tantalum vacancies, which are strongly interacting with the conduction electrons and can trap them at the vacancy site. Such physics is described well by the FK model, with the tantalum vacancy sites serving as the “ f -electrons” that scatter the conduction electrons.

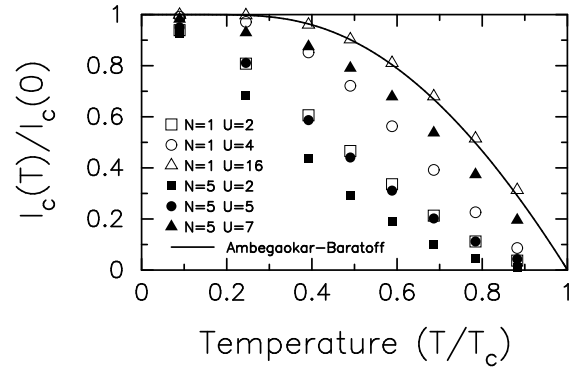


FIG. 36 Critical current as a function of temperature for a variety of different Josephson junctions. Note how the correlated insulator (solid triangles) is parallel to the thin insulator (solid line) for a wide range of T .

In Fig. 36, we plot the critical current as a function of temperature. Once again, our calculations produce the Ambegaokar and Baratoff (1963) results for thin tunnel junctions. As junctions are made more metallic, or thicker, the critical current drops more rapidly as a function of temperature. But the correlated barrier, just on the insulating side of the transition, has a thermal slope $dI_c(T)/dT$ that is essentially equal to that of the thin tunnel junction in the range $0.4T_c < T < 0.7T_c$ which is a typical operating range for a junction. Hence these correlated metal barriers (or SCmS junctions) may be the optimal choice for the barrier in a Josephson junction, enabling ultrafast superconductor-based digital electronics.

D. Resistivity Saturation

The semiclassical Boltzmann equation approach to transport indicates that the resistivity of a material should continue to rise as the temperature rises. However, the theory breaks down once the mean free path of the electrons becomes shorter than the interatomic spacing. Hence, there is an expectation for the resistivity to slow its increase once the mean free path becomes too small. An interesting set of materials that have been investigated a quarter century ago are the so-called A15 compounds such as V_3Si and Nb_3Ge (Fisk and Webb, 1976). These materials sparked much interest as being the highest temperature superconductors of their day, and they were widely studied, but a number of features about these materials remain unsolved.

In conventional electron-phonon scattering metals, the resistivity behaves like

$$\rho(T) = A_\rho T + B_\rho \quad (147)$$

at high temperature. Here A_ρ is proportional to the electron-phonon coupling strength and B_ρ is proportional to the impurity concentration. What was found in the A15 materials was that A_ρ was much smaller than expected, given the known strength of the electron-phonon coupling and B_ρ was sizable, even in very pure samples. This behavior was called resistivity saturation, since it implies a slow turnover of the high-temperature resistivity.

In 1999, Millis *et al.* (1999) solved an important puzzle in the resistivity saturation problem. They examined the static harmonic Holstein model at high temperature and saw the characteristic shape seen in resistivity saturation for strongly coupled systems. This analysis neglects the quantum-mechanical nature of the phonons, since their kinetic energy is neglected, but this should be a good approximation if the phonons are at a temperature much higher than the Einstein frequency of the Holstein model (estimated to be about the Debye frequency of a real material). Note that the resistivity formula used in Millis *et al.* (1999) does not properly have the velocity factors for the Bethe lattice. This does not change the results much near half filling, but would have a larger effect for fillings closer to the band edge.

We illustrate this phenomenon in Fig. 37, where we plot the resistivity at half filling $\rho_e = 1$ for the spin-one-half static harmonic Holstein model on the hypercubic lattice. We examine coupling strengths ranging from a weakly coupled system (that is a fermi gas at $T = 0$) to a strongly coupled insulator, that develops a gap in the conduction electron DOS (see Fig. 25).

The theory behind the resistivity form in Eq. (147) depends on three assumptions: (i) the temperature is much higher than the phonon energy scale, so the ions can be approximated by classical oscillators and the equipartition theorem says $\langle x_i^2 \rangle \approx T/\kappa$; (ii) the electron-phonon interaction can be treated in second-order perturbation theory so the scattering rate is $g_{ep}^2 \langle x_i^2 \rangle$; and (iii) Boltz-

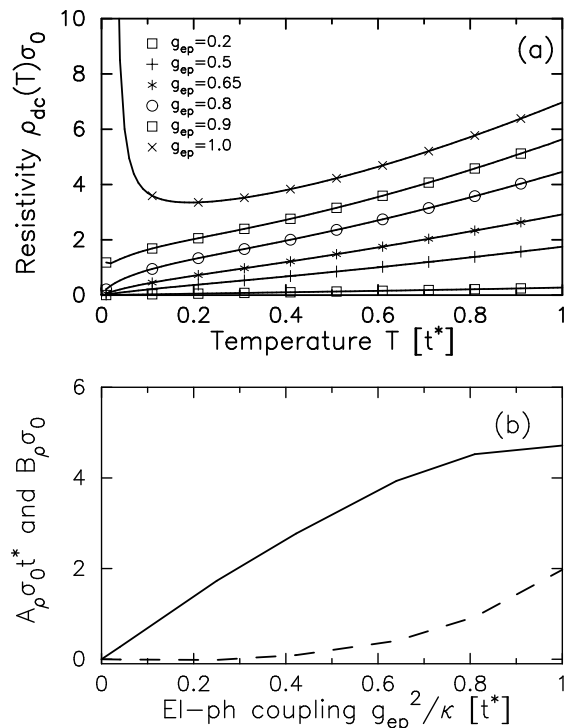


FIG. 37 (a) Resistivity as a function of temperature for the half filled static harmonic Holstein model on the hypercubic lattice and (b) parameters A_ρ (solid line) and B_ρ (dashed line) fit for the range of temperature $0.2 < T < 1$. Note how there is a wide range of temperature where the resistivity appears linear, but with a large intercept. Note further how A_ρ grows slower than $g_{ep}^2 \propto \lambda$.

mann transport theory can relate the scattering rate to the resistivity. Assumptions (i) and (ii) imply that the scattering rate is linear in temperature. Millis *et al.* (1999) find that the scattering rate actually increases like \sqrt{T} due to the breakdown of the second-order perturbation theory for strong coupling. This is the key to resistivity saturation, as can be seen in Fig. 37. Indeed, forcing the square root behavior to fit to a linear form necessarily produces all of the observed resistivity saturation phenomena. Note further that even for an insulating phase, we see the same kind of “resistivity saturation” at high enough temperatures.

It is interesting as well that there are a variety of materials (mainly the doped fullerenes and the high- T_c superconductors) where the resistivity obeys the linear form of Eq. (147) with small or vanishing B_ρ up to very high temperatures, where a naive estimate of the mean free path is much less than a lattice spacing. The DMFT analysis given here does not shed light onto that puzzle, but recent work using other techniques has made much progress (Calandra and Gunnarsson, 2001).

E. Pressure-Induced Metal-Insulator Transitions

Nickel iodide (NiI_2) is a transition-metal halide that undergoes an isostructural metal-insulator transition at room temperature as a function of pressure (Pasternak *et al.*, 1990). Nickel iodide crystallizes in the CdCl_2 structure, which consists of alternating hexagonal planes of nickel and iodine. The nickel ions have a $2+$ valence and the iodine ions have a $1-$ valence; the neutral sandwich $\text{I}^- \text{-Ni}^{++} \text{-I}^-$ is stacked vertically to form the crystal. In the insulating state, the $S = 1$ nickel spins order in a helical spin density wave, that is closely approximated by ferromagnetic nickel planes, stacked in an antiferromagnetic fashion. At ambient pressure $T_N = 75$ K, and T_N increases by a factor of four to 310 K at 19 GPa, where the system undergoes a metal-insulator transition and becomes metallic. The physical picture is as follows: the d -electrons in the nickel band are strongly correlated and form a Mott-like insulating state (which can be approximated by dispersionless localized electrons), and the iodine p -bands are completely filled by the transfer of an electron to each iodine. As pressure increases, the relative position of the iodine p -bands and the nickel d -bands changes, with the iodine p -bands moving closer to the fermi level. Once the p -bands reach the fermi level, electrons spill from the p -bands to the nickel d -bands, quenching the magnetic moment (changing Ni^{++} to Ni^+), stopping the antiferromagnetic transition, and allowing hole conduction within the p -bands. Hence there is a transfer of charge from the iodine to the nickel as the pressure increases causing a metal-insulator transition. This is precisely the kind of transition envisioned in the original Falicov-Kimball model and optical experiments confirm this picture (Chen *et al.*, 1993).

Indeed, one can add spin interaction terms to the FK model, to more accurately approximate this system, and perform an analysis of the thermodynamics and map out a phase diagram. This has already been done with a mean-field-theory calculation (Freericks and Falicov, 1992), which shows antiferromagnetic insulating phases, paramagnetic insulating phases, and metallic phases and is depicted in Fig. 38. The phase diagram also shows a classical critical point, where the first-order metal-insulator transition disappears. Unfortunately, the critical point is estimated to lie around 1400 K, which is beyond the disintegration temperature for NiI_2 . It would be interesting to repeat the analysis of NiI_2 with DMFT, to see if the estimate of the critical point is reduced in temperature and to examine properties like optical conductivity which have been measured.

V. NEW DIRECTIONS

A. $1/d$ Corrections

The dynamical mean field theory is exact in the infinite-dimensional limit. But the real world is finite

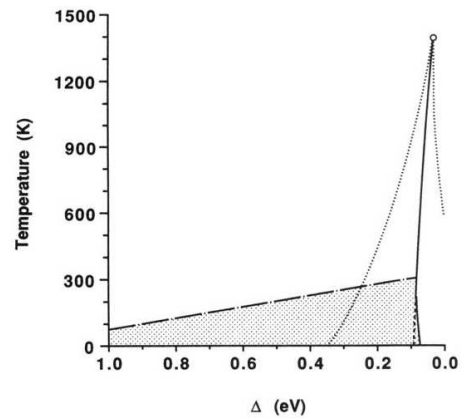


FIG. 38 Mean-field theory phase diagram for NiI_2 calculated within the Falicov-Kimball model picture (Freericks and Falicov, 1992). The shaded region is the antiferromagnetic insulator, the region above the chain-dotted line is the paramagnetic insulator. The paramagnetic metallic phase lies to the right of the nearly vertical solid line. The first order transition line from an insulator to a metal ends in a classical critical point (above that temperature, one can continuously crossover from the metal to the insulator). The symbol Δ denotes the difference in energy from the localized Ni electrons to the bottom of the I bands. It varies with an external parameter like pressure. The dotted lines denote the regions of phase space where three solutions of the mean-field theory equations are stabilized.

dimensional, and so it is important to understand how the infinite-dimensional limit relates to finite dimensions. The simplest approximation for finite dimensions that one can take is the so-called local approximation, where one performs the DMFT, but uses the correct finite-dimensional noninteracting DOS in the relevant Hilbert transform. Such an approach was adopted for the FK model by Freericks (1993b). Since we expect Hartree-Fock theory to be asymptotically exact in the limit as $U \rightarrow 0$ (for $d > 1$), and since the DMFT uses the correct noninteracting susceptibility in determining CDW order, the local approximation is asymptotically exact at weak coupling. Deviations are expected to be much stronger in the large coupling limit (where the model can be mapped onto an effective Ising model at half filling), due to the renormalization of T_c from spatial spin-wave fluctuations that are neglected in the local approximation. In fact, the situation at weak coupling is somewhat more complicated, because it is well known that the Hartree-Fock approximation to the Hubbard model is renormalized due to local quantum fluctuations by factors on the order of three to five (van Dongen, 1991b, 1994). The $1/d$ corrections to this renormalization are typically small for the Hubbard model (on the order of a few percent in two and three dimensions). This weak-coupling perturbative analysis has not been carried out for the FK model, and there may be surprises there, because the DMFT T_c at weak coupling does not take the conventional exponen-

tial form. But the general thrust of this analysis is that one expects DMFT and the local approximation to be reasonably good at weak coupling, with larger deviations as the coupling is made stronger.

The first attempt at a systematic expansion in $1/d$ that can include nonperturbative effects was made by Schiller and Ingersent (1995). They constructed a generic self-consistent two-site impurity problem, which had feedback into an auxiliary single-site impurity problem to calculate both the local and nearest-neighbor contributions to the self energy (i.e. the self energy is allowed to have an additional momentum dependence proportional to $\epsilon_{\mathbf{k}}$). This approach suffered from two difficulties. First, their self-consistent equations encountered convergence problems when U was made large, and they were only able to achieve converged results for small U (where one does not expect there to be large corrections). Second, one can immediately see that in regions where the local contribution to the self energy is small, one might lose causality (the imaginary part of the self energy can have the wrong sign) if the coefficient of the $\epsilon_{\mathbf{k}}$ term is too large. Indeed, the numerical calculations suffered from negative DOS at the band edges as well.

A number of different approximate methods were also attempted to improve upon the situation. The first method is called the dynamical cluster approximation (DCA) (Hettler *et al.*, 2000, 1998) and we will describe it in detail below. The second one is based on a truncation of a memory function expansion (which uses the Liouville operator space and continued-fraction techniques to determine Green's functions) (Minh-Tien, 1998; Tran, 1999). This technique is approximate and it includes static nonlocal correlations and dynamic local correlations, which results in some pathologic behavior, such as the interacting DOS remains temperature independent in the canonical ensemble, just like DMFT. The third method is based on a moment analysis of the Green's function and uses a self-consistent feedback of the f -electron charge susceptibility onto the conduction electron Green's function (Laad and van den Bossche, 2000). This technique also requires a number of uncontrolled approximations in order to have numerical tractability. One of the controversial predictions of the moment approach is that the FK model in two dimensions has the Mott-like metal-insulator transition occur at $U = 0$. The first two techniques predict that it occurs at a finite value of U on the order of half of the bandwidth.

We will concentrate our discussion here on the dynamical cluster approximation, which is a systematic technique in the thermodynamic limit for incorporating nonlocal correlations into the many-body problem. It is not a formal expansion in $1/d$, but rather is an expansion in $1/N_c$, where N_c is the size of the self-consistent cluster employed in the computational algorithm. From a physical point of view, one should view the DCA as an expansion in the spatial size over which spatial fluctuations are included, so it allows large momentum (short-range) spatial fluctuations, but does not properly describe long

wavelength fluctuations. The basic idea is to allow the self energy to have momentum dependence in a coarse-grained fashion. The Brillouin zone is divided into N_c equally sized regions, and the self energy assumes constant values within each of these regions (but can vary from region to region). It turns out that one can guarantee causality is preserved with this technique.

We now describe the DCA algorithm in detail. We begin by dividing the Brillouin zone into N_c coarse-grained cells, labeled by the central point of the cell \mathbf{K} . In this fashion, every wavevector in the Brillouin zone can be written as $\mathbf{k} = \mathbf{K} + \tilde{\mathbf{k}}$ with $\tilde{\mathbf{k}}$ ranging over the coarse-grained cell. The \mathbf{K} points are chosen to correspond to the wavevectors of the N_c -site cluster with periodic boundary conditions. The algorithm proceeds then as follows: (i) we choose our initial guess for the coarse-grained self energy $\Sigma(\mathbf{K}, \omega)$; (ii) we construct the coarse-grained Green's function via

$$\bar{G}(\mathbf{K}, \omega) = \frac{N_c}{N} \sum_{\tilde{\mathbf{k}}} \frac{1}{\omega + \mu - \Sigma(\mathbf{K}, \omega) - \epsilon_{\mathbf{K}+\tilde{\mathbf{k}}}}; \quad (148)$$

(iii) we extract the effective medium for the cluster $G_0^{-1}(\mathbf{K}, \omega) = \bar{G}^{-1}(\mathbf{K}, \omega) + \Sigma(\mathbf{K}, \omega)$; (iv) we solve the cluster problem for the cluster Green's functions G_c given the effective medium G_0 and determine the cluster self energy via $\Sigma_c(\mathbf{K}, \omega) = G_0^{-1}(\mathbf{K}, \omega) - G_c^{-1}(\mathbf{K}, \omega)$; (v) we equate the cluster self energy with the coarse-grained self energy $\Sigma(\mathbf{K}, \omega) = \Sigma_c(\mathbf{K}, \omega)$ and substitute into step (ii) to repeat the process. The algorithm is iterated until it converges. Once converged, one can then evaluate the irreducible vertex functions on the cluster using analogous Dyson equations; equating the cluster irreducible vertex functions to the coarse-grained irreducible vertex functions on the lattice then allows one to compute susceptibilities.

Under the assumption that the technique used to solve the cluster Green's functions given the effective medium G_0 is a causal procedure, then the cluster Green's functions and self energies are manifestly causal. Forming the coarse-grained Green's function on the lattice from the causal cluster self energy maintains the causality of the Green's function. The only place where noncausality could enter the algorithm is in the step where we extract the effective medium, if the imaginary part of \bar{G}^{-1} is smaller in magnitude than the imaginary part of the coarse-grained self energy. But one can prove that this never occurs, hence the algorithm is manifestly causal.

The DCA was applied to the FK model using two different techniques. When the cluster size was small enough ($N_c \leq 16$), one could use exact enumeration to determine the weights for every possible configuration of localized electrons on the lattice, and since the action is quadratic in the fermions, one can determine the partition function exactly. For larger clusters, one needs to determine the weights via a statistical sampling procedure, including the weights that are largest in the partition sums and neglecting those that are too small. We will describe the exact enumeration method only here.

We let f denote a configuration $\{n_1^f, n_2^f, \dots, n_{N_c}^f\}$ of the localized electrons (we consider only the spinless FK model for simplicity). Then, the partition function for the cluster becomes

$$\mathcal{Z}_c = \sum_{\{f\}} 2^{N_c} e^{\beta \mu N_c / 2} e^{-\beta(E_f - \mu_f) N_c} \times \prod_{n=-\infty}^{\infty} \frac{\text{Det}[G_0^{-1}(i, j, i\omega_n) - U n_i^f \delta_{ij}]}{[i\omega_n]^{N_c}} \quad (149)$$

where the symbol N_c^f denotes the total number of localized electrons in the configuration f and i and j are spatial indices on the cluster. The determinant is over the spatial indices i and j . The weight for the configuration f is the corresponding term in Eq. (149) divided by \mathcal{Z}_c ; we denote that weight by w_f . The cluster Green's function on the imaginary or real axis is then simply

$$G_c(i, j, z) = \sum_{\{f\}} w_f [G_0^{-1}(i, j, z) - U n_i^f \delta_{ij}]^{-1}. \quad (150)$$

The weights are determined solely from the Green's functions evaluated on the imaginary axis, while the Green's functions on the real axis are trivial to determine once the weights are known. The convergence of the iterative algorithm is much slower on the real axis though.

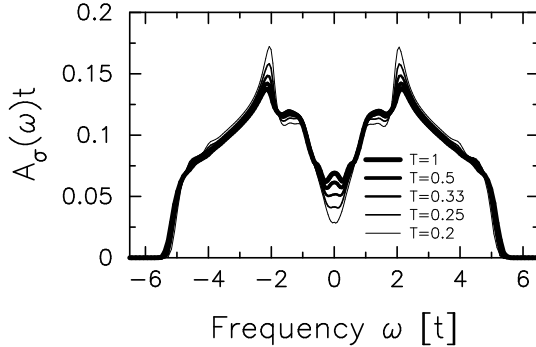


FIG. 39 Many-body density of states for the half-filled FK model on a square lattice using the DCA on a 4×4 cluster with $U = 4$ (Hettler *et al.*, 2000). Note how the DOS now has temperature dependence, and how a pseudogap develops and deepens as T is lowered. Once a CDW opens, the system will open a true gap.

One of the interesting features of the DCA is that it restores temperature dependence to the conduction-electron DOS. This is shown in Fig. 39 where we plot the DOS at five different temperatures (all above the CDW T_c) for an intermediate value of $U = 4t$ on a 4×4 square-lattice cluster at half filling (Hettler *et al.*, 2000). Note how the pseudogap deepens as the temperature is lowered. Of course a true gap will develop in the CDW phase at the lowest temperatures. There is no obvious way of “turning off” the CDW phase below T_c anymore, because the f configurations with the highest weight will be those that correspond to the CDW ordered state below T_c .

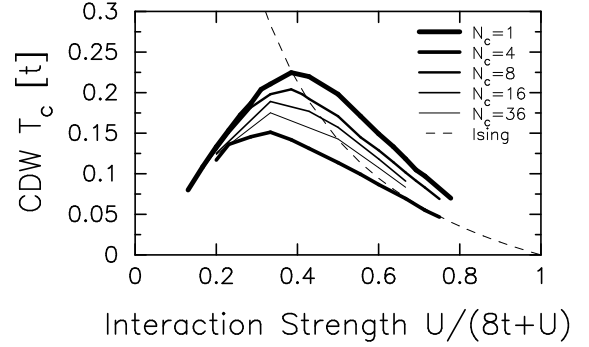


FIG. 40 Phase diagram for the half-filled FK model on a square lattice with the DCA (Hettler *et al.*, 2000). The different lines correspond to different size clusters. The 2×2 cluster determines T_c from the ordered phase, while the other clusters employ a susceptibility analysis. Also included in the figure is the Ising model T_c for the effective spin model with $J = t^2/2U$.

We also plot the phase diagram in Fig. 40 at half filling (Hettler *et al.*, 2000). Included in the plot are the local approximation, cluster calculations from susceptibilities on clusters up to $N_c = 36$, and an Ising model T_c for $J = 2t^2/U$ which the FK model maps onto at strong coupling; note that the 2×2 lattice result comes from an ordered-phase calculation with exact enumeration, rather than a susceptibility calculation. There are a number of interesting comments to make about this phase diagram. First, as expected we find the T_c is hardly changed on the weak-coupling side of the diagram, indicating that the local approximation determines the majority of the many-body correlations in this regime. In the large- U regime, one can see that the DCA does converge towards the correct Ising model result, albeit slowly. The 2×2 data is surprising, as it is much lower than the results for other clusters, but one can perhaps understand why this would be by realizing that a four-site square lattice cluster with periodic boundary conditions is identical to a four-site one-dimensional chain cluster, except for a change in the overall normalization of the hopping. Since the T_c for a one-dimensional chain is equal to zero, the suppression of T_c for the four-site cluster could be arising from the two possible interpretations of the cluster. Hettler *et al.* (2000) argue in a similar vein, where they observe that the fermi-surface points on a four-site cluster occur at the van-Hove singularities, which have uncommonly large scattering rates and hence are unfavorable for CDW order.

It is possible to explore dynamical susceptibilities within the DCA as well. One simply needs to extract the frequency and coarse-grained momentum irreducible susceptibilities and use the relevant Bethe-Salpeter equation to calculate the full susceptibility. Unlike in the DMFT, where the irreducible vertex only renormalizes symmetry channels that have the full symmetry of the lattice, the vertex now renormalizes all channels, because it contains

momentum dependence. This remains one of the open problems of interest for the DCA.

B. Hybridization and f -Electron Hopping

The FK model in infinite dimensions admits a simple solution, because the Hilbert space of the impurity problem generated by the DMFT mapping is a direct product of invariant subspaces with a fixed f -occupation. In each subspace we can easily find the itinerant electron Green's function and the generalized partition function [the generating functional of Kadanoff and Baym, $Z = \text{Det}(G_0^{-1})$]. In the absence of quantum fluctuations in the f -particle number each f -state has an infinite lifetime but the f -spectral function acquires a finite width due to the $f - c$ coupling which acts as an effective time-dependent potential for the f -electrons and the broadening is due to the statistical averaging over all possible states. In this respect the FK problem is a lattice generalization of the X-ray edge problem. Actually, as long as the coherent scattering of conduction electrons on f -electrons is neglected, we can drop the self-consistency condition Eq.(31) and use the X-ray edge model solution for the lattice problem (Si *et al.*, 1992). At lower temperatures, the system becomes coherent and the single-site X-ray solution has to be replaced by the DMFT self-consistency (effective medium), so as to keep track of all the other f -sites on the lattice. Despite its simplicity, the DMFT solution of the FK model has some interesting features and can be used to describe physical systems in which quantum fluctuations can be neglected, like the high-temperature phase of Yb- and Eu-compounds with a valence-change transition or the charge-transfer metal-insulator transition in NiI_2 .

However, if the f -particle dynamics are important, which is often the case at low enough temperature, one should consider a more general model. For example, in the Yb-systems discussed in Section IV.A, the valence of Yb ions below T_v is much larger than predicted by the FK model and the reduction of the local moment does not follow from $\rho_f(T)$ but is due to quantum fluctuations and lifetime effects. If the ground state is a mixture of 2+ and 3+ states one should not neglect the $f - c$ hybridization and a better description would be provided by a periodic Anderson model with an additional FK term. The actual situation pertaining to Yb ions is quite complicated, as one should consider an extremely asymmetric limit of the Anderson model, in which there is no Kondo resonance (the ground state is not Kondo-like) and there is no single universal energy scale which is relevant at all temperatures (Krishnamurty *et al.*, 1980). We believe such a generalized model would behave as the FK model at high temperatures and as a periodic Anderson model at low temperatures. Indeed, incoherent scattering of conduction electrons on the FK ions favors the gap opening even in the presence of hybridization; and if the width of the f -level is large due to the

FK interaction, the additional effects due to quantum mixing should be irrelevant. This is supported by the scaling arguments (Withoff and Fradkin, 1990) and the numerical renormalization group analysis of various impurity models (Vojta and Bulla, 2002) which show that, as long as the chemical potential is close to the gap and the hybridization is below some critical value, the f -level decouples from the conduction sea. On the other hand, at low temperature, the chemical potential shifts away from the gap in the DOS. For a flat conduction band and the f -level close to the chemical potential, the hybridization effects are important and they can drive the system towards a valence-fluctuating fixed point. The most likely effect of the FK correlation at low temperatures is to renormalize the parameters of the Anderson model.

A generalized FK model might also be needed to describe the electronic ferroelectrics proposed by Portengen *et al.* (1996a,b). The Bose-Einstein condensation (BEC) of $f - c$ excitons and a spontaneous polarization can be obtained by a mean-field treatment of the hybridized model. This picture is further supported by the examination of the spontaneous hybridization for the spinless FK model on the Bethe lattice, where it is found that as the temperature is lowered the system appears to have a logarithmic divergence in the spontaneous hybridization susceptibility at $T = 0$. Normally we cannot reach such a state because the system will have a phase transition to either a phase separated state or a charge-density wave, but we can tune the system so that it remains in a classical intermediate-valence state down to $T = 0$. When this occurs, effects of even a small hybridization will take the system away from the FK fixed point at low enough temperature.

Another generalization is obtained by allowing direct $f - f$ hopping, t_{ij}^f , which leads, for $t_{ij}^f = t_{ij}^c$, to the rich physics of the Hubbard model (Hubbard, 1963). The case $t_{ij}^f \ll t_{ij}^c$ is also interesting, because even a small $f - f$ hopping induces an $f - c$ coherence and gives a ground state (for large U) which is either a BEC of electron-hole pairs ($f - c$ excitons) or an orbitally ordered state (Batista, 2002). Unfortunately, as soon as the f -electron dynamics is restored, the evolution operator connects all sectors of the Hilbert space and the resulting DMFT equations describe a two-level system with each level coupled to an arbitrary external field. This problem (or the equivalent Anderson impurity problem) is much more difficult to solve than the FK impurity problem with a single external field coupled to an electron.

C. Nonequilibrium Effects

Equilibrium properties in the DMFT have been studied extensively. Much less effort has been placed on nonequilibrium calculations, where the correlated many-body system is driven away from equilibrium by large amplitude external fields or driving voltages. The formal-

ism for DMFT in a nonequilibrium situation has been addressed by Schmidt and Monien (2002). They considered the case of a Hubbard model that interacts with a large amplitude electromagnetic field with a constant driving frequency ω . The formalism employs Keldysh techniques to derive the three Green's functions of relevance: the advanced, retarded, and so-called lesser Green's function. They find that in the steady state, one can perform calculations in frequency space, if the driving frequency is uniform. They applied their calculations to the Hubbard model, and used the iterated perturbation theory to evaluate the impurity-problem dynamics. Nevertheless, their formalism is general, and can be used for FK model problems as well. In addition, one could choose to perform calculations purely in the time domain. This would allow one to calculate the response of the system to large amplitude, and fast (i.e. femtosecond) electromagnetic pulses. In this case, one would be interested in the transient response that brings the system back to the equilibrium state after being disturbed.

There is another class of problems that are ideal for being considered with Keldysh techniques. Namely, the problem of the steady-state current response to a voltage applied over an inhomogeneous device. One can imagine stacking correlated planes (described by the FK model) in between a semi-infinite number of noninteracting metallic planes (above and below) that form ballistic current leads for the device. One enforces current conservation from plane to plane, which then determines the change in the voltage from plane to plane in the device. In this fashion, one can calculate the self-consistent current-voltage characteristic of a nonlinear device that contains correlated materials (and also the voltage profile throughout the device). The leads can be described by a wide class of Hamiltonians, including the Hartree-Fock description of a ferromagnet, or a Bardeen-Cooper-Schrieffer superconductor, or a diffusive FK metal, and the barrier material (of arbitrary width) can be described by the FK model tuned through the metal-insulator transition. Then, since the total action is quadratic in the fermionic variables (although it is not time-translation-invariant) the path integral over the Keldysh contour can be evaluated by taking the determinant of the corresponding continuous (matrix) operator. Discretizing the operator as was done when we described the localized electron spectral function, will then allow for the response to be solved exactly. We believe this will be the first example of a correlated electronic system that can undergo a metal-insulator transition, and have its nonequilibrium response determined exactly. The calculation is nontrivial, but is likely to produce a series of interesting results. One can apply such a formalism to a wide variety of devices such as Josephson junctions, spin-valve transistors, ballistic spin filters, or thermoelectric coolers. The choices are endless, as long as one always restricts the effective actions to remain quadratic in the fermionic variables. Generalization to more complicated systems is also possible, but usually requires one to re-

sort to approximate methods to solve the corresponding impurity problems.

VI. CONCLUSIONS

It has been over thirty years since Falicov and Kimball introduced their model to describe the physics behind rare-earth and transition-metal metal-insulator transitions. The model has a rich history and much effort has been devoted to solving the model and illustrating its properties. The field was dramatically advanced fourteen years ago when Brandt and Mielsch showed that the model could be solved exactly in the limit of large dimensions. Since then much work has been done on investigating the solutions of the model.

In this review we have covered the exact solution of the Falicov-Kimball model (and the related static Holstein model) with dynamical mean-field theory. Our focus was on developing the formalism with a path-integral approach that concentrated on the Matsubara frequency representation of the fermions. Falicov-Kimball model physics is a mature field where nearly all thermodynamic properties of the solutions have been worked out in the limit of large spatial dimensions. This includes charge-density-wave transitions, metal-insulator transitions, phase separation, electrical and thermal transport, inelastic light scattering, and so on. The model has also been employed in more applied problems such as investigating thermodynamic properties of Josephson junctions.

These exact solutions are useful for two reasons. First, there is a growing list of materials that appear to be able to be described by FK model physics, including YbInCu_4 , $\text{EuNi}_2(\text{Si}_{1-x}\text{Ge}_x)_2$, Ta_xN , and NiI_2 . Similar models have been also applied to the doped manganites and to diluted magnetic semiconductors. Second, exact solutions are useful benchmarks for illustrating the phenomena associated with strong correlations and for testing different approximation methods for their accuracy.

The newer frontiers that will be examined in the future include a thorough investigation of equilibrium properties in finite-dimensional systems, the addition of hybridization or itineracy of the f -electrons and the examination of nonequilibrium effects in all dimensions. The success to date with this model, indicates that the time is ripe for more applications in the near future. It seems likely the FK model can be employed to determine a number of interesting applications in correlated devices, which can lay the groundwork for later efforts in more complicated correlated systems. We look forward to seeing how the field will develop in the ensuing years and hope that this review will encourage others to enter the field and rapidly contribute to its future development.

Acknowledgments

Our work on the Falicov-Kimball model and related models has been supported over the past few years by the National Science Foundation under grants DMR-9973225 and DMR-0210717 and by the Office of Naval Research under grants N00014-96-1-0828 and N00014-99-1-0328. V.Z. acknowledges support from the Swiss National Science Foundation grant no. 7KRPJ65554, the Alexander von Humboldt foundation and the Ministry of Science of Croatia. In addition, we are grateful to the many useful discussions and collaborations with colleagues on the properties of the Falicov-Kimball model. While we cannot list everyone who has influenced us, we especially would like to thank P. Anderson, J. Annett, I. Aviani, D. Belitz, U. Brandt, A. Chattopadhyay, A. Chen, W. Chung, S.L. Cooper, G. Czycholl, T. Devereaux, L. Falicov, P. Farsakovský, Z. Fisk, C. Geibel, A. Georges, Ch. Gruber, R. Hackl, Z. Hasan, M. Hettler, J. Hirsch, V. Janis, M. Jarrell, J. Jedrezejewski, T. Kirkpatrick, T. Klapwijk, M. Klein, G. Kotliar, R. Lemański, E. Lieb, N. Macris, G. Mahan, J. Mannhart, M. Mihjak, P. Miller, A. Millis, E. Müller-Hartmann, N. Newman, B. Nikolić, M. Očko, P. Nozières, Th. Pruschke, J. Rowell, J. Sarrao, D. Scalapino, J. Serene, L. Sham, S. Shastry, Z.-X. Shen, A. Schiller, A. Shvaika, F. Steglich, N. Tahvildar-Zadeh, D. Ueltschi, P. van Dongen, T. van Duzer, and D. Vollhardt. We also thank P. van Dongen for a critical reading of this manuscript.

List of Symbols

References

- Allen, J. W., and R. M. Martin, 1982, Phys. Rev. Lett. **49**, 1106.
 Allub, R., and B. Alascio, 1996, Solid St. Commun. **99**, 66.
 Allub, R., and B. Alascio, 1997, Phys. Rev. B **55**, 14113.
 Altshuler, T., M. Bresler, M. Schlott, B. Elschner, and E. Graty, 1995, Z. Phys. B **99**, 57.
 Ambegaokar, V., and A. Baratoff, 1963, Phys. Rev. Lett. **10**, 486.
 Anderson, P. W., 1959, J. Phys. Chem. Solids **11**, 26.
 Ashcroft, N. W., and N. D. Mermin, 1976, *Solid State Physics* (Holt, Rinehart and Winston, Philadelphia).
 Batista, C. D., 2002, Phys. Rev. Lett. **89**, 166403.
 Baym, G., 1962, Phys. Rev. **127**, 1391.
 Bergmann, G., and D. Rainer, 1974, Z. Phys. **174**, 445.
 Blawid, S., and A. J. Millis, 2000, Phys. Rev. B **62**, 2424.
 Blawid, S., and A. J. Millis, 2001, Phys. Rev. B **63**, 115114.
 Brandt, U., and A. Fledderjohann, 1992, Z. Phys. B **87**, 111.
 Brandt, U., A. Fledderjohann, and G. Hulsbeck, 1990, Z. Phys. B **81**, 409.
 Brandt, U., and C. Mielsch, 1989, Z. Phys. B **75**, 365.
 Brandt, U., and C. Mielsch, 1990, Z. Phys. B **79**, 295.
 Brandt, U., and C. Mielsch, 1991, Z. Phys. B **82**, 37.
 Brandt, U., and R. Schmidt, 1986, Z. Phys. B **63**, 45.
 Brandt, U., and R. Schmidt, 1987, Z. Phys. B **67**, 43.
 Brandt, U., and M. P. Urbanek, 1992, Z. Phys. B **89**, 297.

A_{1g}, B_{1g}, B_{2g}	symmetries for inelastic light scattering
A_ρ (B_ρ)	coefficients for resistivity saturation
$A_\sigma(\omega)$	interacting conduction electron DOS
$A_\sigma(\epsilon, \omega)$	spectral function
Det	determinant
$E_{f\eta}$	localized electron site energy
E_f^*	renormalized f -level
F^{Helm}	Helmholz free energy
$F_\eta(z)$	localized electron Green's function
$F_\infty(z)$	Hilbert transform
$G(z)$	local conduction electron Green's function
$G_0(z)$	effective medium
H	magnetic field
\bar{K}	cluster momentum
L_{ij}	transport coefficients
S	thermopower
$2S + 1$	number of η states
S_L (S_{imp})	lattice (impurity) action
T	temperature
T_v	valence-change transition temperature
T_τ	time-ordering operator
Tr	trace
U	FK interaction
$U_{\eta\eta'}^{ff}$	$f - f$ Coulomb interaction
V	number of lattice sites
W_i	integral weight factors
$X(\mathbf{q})$	momentum parameter
$Z_{n\sigma}$	argument ($i\omega_n + \mu - \Sigma_{n\sigma}$)
ZT	thermal transport figure-of-merit
$Z(0)$	wavefunction renormalization factor
$c_{i\sigma}^\dagger$ ($c_{i\sigma}$)	creation (annihilation) operator of itinerant electron at site i with spin σ
e	electric charge
exp	exponential
$f_{i\eta}^\dagger$ ($f_{i\eta}$)	creation (annihilation) operator of localized electron at site i with spin η
$f(\omega)$	Fermi-Dirac distribution
g	gyromagnetic ratio (conduction electrons)
g^{aux}	auxiliary Green's function
g_{ep}	electron-phonon coupling (deformation potential)
g_f	gyromagnetic ratio (itinerant electrons)
j_n (j_Q)	number (heat) current operator
k_B	Boltzmann constant
ln	natural logarithm

- Calandra, M., and O. Gunnarsson, 2001, Phys. Rev. Lett. **87**, 266601.
 Chattopadhyay, A., S. Das Sarma, and A. J. Millis, 2001, Phys. Rev. Lett. **87**, 227202.
 Chattopadhyay, A., A. J. Millis, and S. Das Sarma, 2000, Phys. Rev. B **61**, 10738.
 Chen, A. L., P. Y. Yu, and R. D. Talyor, 1993, Phys. Rev.

- Lett. **71**, 4011.
- Chester, G. V., and A. Thellung, 1961, Proc. Phys. Soc. London **77**, 1005.
- Chung, W., and J. K. Freericks, 1998, Phys. Rev. B **57**, 11955.
- Chung, W., and J. K. Freericks, 2000, Phys. Rev. Lett. **84**, 2461.
- Ciuchi, S., and F. de Pasquale, 1999, Phys. Rev. B **59**, 5431.
- Cornelius, A. L., J. M. Lawrence, J. Sarrao, Z. Fisk, M. F. Hundley, G. H. Kwei, J. D. Thompson, C. H. Booth, and F. Bridges, 1997, Phys. Rev. B **56**, 7993.
- Czycholl, G., 1999, Phys. Rev. B **59**, 2642.
- Dallera, C., M. Grioni, A. Shukla, G. Vankó, J. L. Sarrao, J. P. Rueff, and D. L. Cox, 2002, Phys. Rev. Lett. **88**, 196403.
- de Vries, P., K. Michielsen, and H. De Raedt, 1993, Phys. Rev. Lett. **70**, 2463.
- de Vries, P., K. Michielsen, and H. De Raedt, 1994, Z. Phys. B **95**, 475.
- Devereaux, T. P., G. E. D. McCormack, and J. K. Freericks, 2003, Phys. Rev. Lett. **90**, XXXXXX.
- van Dongen, P. G. J., 1991a, Mod. Phys. Lett. B **5**, 861.
- van Dongen, P. G. J., 1991b, Phys. Rev. Lett. **67**, 757.
- van Dongen, P. G. J., 1992, Phys. Rev. B **45**, 2267.
- van Dongen, P. G. J., 1994, Phys. Rev. B **50**, 14016.
- van Dongen, P. G. J., and N. Blümer, 2002, unpublished.
- van Dongen, P. G. J., and C. Leinung, 1997, Ann. Phys. (Leipzig) **6**, 45.
- van Dongen, P. G. J., and D. Vollhardt, 1990, Phys. Rev. Lett. **65**, 1663.
- Dzero, M. O., 2002, J. Phys.: Condens. Matter **14**, 631.
- Dzero, M. O., L. Gor'kov, and A. K. Zvezdin, 2000, J. Phys.: Condens. Matter **12**, L711.
- Dzero, M. O., L. Gor'kov, and A. K. Zvezdin, 2002, Physica B **312 & 313**, 321.
- Economou, E. N., 1983, *Green's Functions in Quantum Physics* (Springer-Verlag, Berlin).
- Elitzur, S., 1975, Phys. Rev. D **12**, 3978.
- Falicov, L. M., and J. C. Kimball, 1969, Phys. Rev. Lett. **22**, 997.
- Farkasovský, P., 1997, Z. Phys. B **104**, 553.
- Farkasovský, P., 1999, Phys. Rev. B **59**, 9707.
- Farkasovský, P., 2002, Phys. Rev. B **65**, 081102.
- Felner, I., and I. Novik, 1986, Phys. Rev. B **33**, 617.
- Fetter, A. L., and J. D. Walecka, 1971, *Quantum Theory of Many-Particle Systems* (McGraw-Hill, New York).
- Figuroa, E., J. M. Lawrence, J. Sarrao, Z. Fisk, M. F. Hundley, and J. D. Thompson, 1998, Solid State Commun. **106**, 347.
- Fisk, Z., and G. W. Webb, 1976, Phys. Rev. Lett. **36**, 1084.
- Freericks, J. K., 1993a, Phys. Rev. B **47**, 9263.
- Freericks, J. K., 1993b, Phys. Rev. B **48**, 14797.
- Freericks, J. K., and T. P. Devereaux, 2001a, Condens. Mat. Phys. **4**, 149.
- Freericks, J. K., and T. P. Devereaux, 2001b, Phys. Rev. B **64**, 125110.
- Freericks, J. K., T. P. Devereaux, and R. Bulla, 2001a, Acta Phys. Pol. B **32**, 3219.
- Freericks, J. K., and L. M. Falicov, 1990, Phys. Rev. B **41**, 2163.
- Freericks, J. K., and L. M. Falicov, 1992, Phys. Rev. B **45**, 1896.
- Freericks, J. K., C. Gruber, and N. Macris, 1996, Phys. Rev. B **53**, 16189.
- Freericks, J. K., C. Gruber, and N. Macris, 1999, Phys. Rev. B **60**, 1617.
- Freericks, J. K., and R. Lemański, 2000, Phys. Rev. B **61**, 13438.
- Freericks, J. K., E. H. Lieb, and D. Ueltschi, 2002a, Phys. Rev. Lett. **88**, 106401.
- Freericks, J. K., E. H. Lieb, and D. Ueltschi, 2002b, Commun. Math. Phys. **227**, 243.
- Freericks, J. K., and P. Miller, 2000, Phys. Rev. B **62**, 10022.
- Freericks, J. K., B. N. Nikolić, and P. Miller, 2001b, Phys. Rev. B **64**, 054511.
- Freericks, J. K., B. N. Nikolić, and P. Miller, 2002c, Int. J. Modern Phys. B **16**, 531.
- Freericks, J. K., B. N. Nikolić, and P. Miller, 2003, Appl. Phys. Lett. **XX**, XXXXX.
- Freericks, J. K., and V. Zlatić, 1998, Phys. Rev. B **58**, 322.
- Freericks, J. K., and V. Zlatić, 2001a, Phys. Rev. B **64**, 073109.
- Freericks, J. K., and V. Zlatić, 2001b, Phys. Rev. B **64**, 245118.
- Freericks, J. K., and V. Zlatić, 2002a, Phys. Rev. B **66**, 249901, erratum.
- Freericks, J. K., and V. Zlatić, 2002b, eprint cond-mat/0211385.
- Freericks, J. K., V. Zlatić, and M. Jarrell, 2000, Phys. Rev. B **61**, 838.
- Garner, S. R., J. Hancock, Y. Rodriguez, Z. Schlesinger, B. Bucher, Z. Fisk, and J. L. Sarrao, 2000, Phys. Rev. B **63**, R4778.
- Georges, A., G. Kotliar, W. Krauth, and M. J. Rozenberg, 1996, Rev. Mod. Phys. **68**, 13.
- Gonçalves da Silva, C. E. T., and L. M. Falicov, 1972, J. Phys. C: Solid State Phys. **5**, 906.
- Goremychkin, E. A., and R. Osborn, 1993, Phys. Rev. B **47**, 14280.
- Greenwood, D. A., 1958, Proc. Phys. Soc. (London) **71**, 585.
- Gruber, C., 1999, *Mathematical Results in Statistical Mechanics* (World Scientific, Singapore), p. 199.
- Gruber, C., and N. Macris, 1996, Helv. Phys. Acta **69**, 850.
- Gruber, C., N. Macris, P. Royer, and J. K. Freericks, 2001, Phys. Rev. B **63**, 165111.
- Gruber, C., D. Ueltschi, and J. Jędrzejewski, 1994, J. Stat. Phys. **76**, 125.
- Haller, K., 2000, Commun. Math. Phys. **210**, 703.
- Haller, K., and T. Kennedy, 2001, J. Stat. Phys. **102**, 15.
- Hettler, M. H., M. Mukherjee, M. Jarrell, and H. R. Krishnamurthy, 2000, Phys. Rev. B **61**, 12739.
- Hettler, M. H., N. Tahvildar-Zadeh, M. Jarrell, T. Pruschke, and H. R. Krishnamurthy, 1998, Phys. Rev. B **58**, R7475.
- Hirsch, J. E., 1993, Phys. Rev. B **47**, 5351.
- Holstein, T., 1959, Ann. Phys. (New York) **8**, 325.
- Hubbard, J., 1963, Proc. Roy. Soc. (London) **A276**, 238.
- Hwang, E. H., A. J. Millis, and S. Das Sarma, 2002, **65**, 233206.
- Immer, C. D., J. Sarrao, Z. Fisk, A. Lacerda, C. Mielke, and J. D. Thompson, 1997, Phys. Rev. B **56**, 71.
- Janis, V., 1994, Phys. Rev. B **49**, 1612.
- Jarrell, M., 1992, Phys. Rev. Lett. **69**, 168.
- Jonson, M., and G. D. Mahan, 1980, Phys. Rev. B **21**, 4223.
- Jonson, M., and G. D. Mahan, 1990, Phys. Rev. B **42**, 9350.
- Josephson, B. D., 1962, Phys. Lett. **1**, 251.
- Kaul, A., S. Whitely, T. van Duzer, L. Yu, N. Newman, and J. Rowell, 2001, Appl. Phys. Lett. **78**, 99.
- Kennedy, T., 1994, Rev. Math. Phys. **6**, 901.
- Kennedy, T., 1998, J. Stat. Phys. **91**, 829.

- Kennedy, T., and E. Lieb, 1986, *Physica* **138A**, 320.
- Khurana, A., 1990, *Phys. Rev. Lett.* **64**, 1990.
- Krishnamurty, H. B., J. W. Wilkins, and K. G. Wilson, 1980, *Phys. Rev. B* **21**, 1044.
- Kubo, R., 1957, *J. Phys. Soc. Japan* **12**, 570.
- Laad, M. S., and M. van den Bossche, 2000, *J. Phys.: Condens. Matter* **12**, 2209.
- Lawrence, J. M., R. Osborn, J. L. Sarrao, and Z. Fisk, 1999, *Phys. Rev.* **59**, 1134.
- Lawrence, J. M., S. M. Shapiro, J. L. Sarrao, and Z. Fisk, 1997, *Phys. Rev.* **55**, 14467.
- Lemberger, P., 1992, *J. Phys. A* **25**, 715.
- Letfulov, B. M., 1999, *Europhys. J.* **B11**, 423.
- Letfulov, B. M., and J. K. Freericks, 2001, *Phys. Rev. B* **64**, 174409.
- Levin, E., B. S. Kuzhel, O. Bodak, B. D. Belan, and I. Stets, 1990, *Phys. Stat. Sol. (b)* **161**, 783.
- Lieb, E., 1986, *Physica* **140A**, 240.
- Likharev, K., 2000, *Applications of Superconductivity* (Kluwer, Dordrecht), chapter 5.
- Luttinger, J. M., and J. C. Ward, 1960, *Phys. Rev.* **118**, 1417.
- Maldague, P. F., 1977, *Phys. Rev. B* **16**, 2437.
- Metzner, W., 1991, *Phys. Rev. B* **43**, 8549.
- Metzner, W., and D. Vollhardt, 1989, *Phys. Rev. Lett.* **62**, 324.
- Michielsen, K., 1993, *Int. J. Mod. Phys. B* **7**, 2571.
- Miller, P., and J. K. Freericks, 2001, *J. Phys.: Condens. Matter* **13**, 3187.
- Millis, A. J., J. Hu, and S. Das Sarma, 1999, *Phys. Rev. Lett.* **82**, 2354.
- Millis, A. J., P. B. Littlewood, and B. I. Shraiman, 1995, *Phys. Rev. Lett.* **74**, 5144.
- Millis, A. J., R. Mueller, and B. I. Shraiman, 1996, *Phys. Rev. B* **54**, 5389.
- Minh-Tien, T., 1998, *Phys. Rev. B* **58**, R15965.
- Mitsuda, A., T. Goto, K. Yoshimura, W. Zhang, N. Sato, K. Kosige, and H. Wada, 2002, *Phys. Rev. Lett.* **88**, 137204.
- Moeller, G., A. Ruckenstein, and S. Schmitt-Rink, 1992, *Phys. Rev. B* **46**, 7427.
- Müller-Hartmann, E., 1989a, *Z. Phys. B* **74**, 507.
- Müller-Hartmann, E., 1989b, *Int J. Mod. Phys. B* **3**, 2169.
- Murani, A., D. Richard, and R. Bewley, 2002, *Physica B* **312** & **313**, 346.
- Nyhus, P., S. Cooper, and Z. Fisk, 1995a, *Phys. Rev. B* **51**, R15626.
- Nyhus, P., S. Cooper, Z. Fisk, and J. Sarrao, 1995b, *Phys. Rev. B* **52**, R14308.
- Nyhus, P., S. Cooper, Z. Fisk, and J. Sarrao, 1997, *Phys. Rev. B* **55**, 12488.
- Očko, M., and J. L. Sarrao, 2002, *Physica B* **312** & **313**, 341.
- Pasternak, M. P., R. D. Taylor, A. Chen, C. Meade, L. M. Falicov, A. Giesekus, R. Jeanloz, and P. Y. Yu, 1990, *Phys. Rev. Lett.* **65**, 790.
- Plischke, M., 1972, *Phys. Rev. Lett.* **28**, 361.
- Portengen, T., T. Oestreich, and L. J. Sham, 1996a, *Phys. Rev. Lett.* **76**, 2284.
- Portengen, T., T. Oestreich, and L. J. Sham, 1996b, *Phys. Rev. B* **54**, 17452.
- Potthoff, M., and W. Nolting, 1999, *Phys. Rev. B* **59**, 2549.
- Pruschke, T., D. L. Cox, and M. Jarrell, 1993a, *Europhys. Lett.* **21**, 593.
- Pruschke, T., D. L. Cox, and M. Jarrell, 1993b, *Phys. Rev. B* **47**, 3553.
- Pruschke, T., M. Jarrell, and J. K. Freericks, 1995, *Adv. Phys.* **44**, 187.
- Ramakrishnan, T. V., 2003, *Concepts in Electron Correlation* (Kluwer, Dordrecht), volume XX of *Nato Science Series II. Mathematics, Physics, and Chemistry*, p. XXX.
- Ramirez, R., and L. M. Falicov, 1971, *Phys. Rev. B* **3**, 2425.
- Ramirez, R., L. M. Falicov, and J. C. Kimball, 1970, *Phys. Rev. B* **2**, 3383.
- Rettori, C., S. B. Oseroff, D. Rao, P. G. Pagliuso, G. E. Barberis, J. Sarrao, Z. Fisk, and M. F. Hundley, 1997, *Phys. Rev. B* **56**, 7993.
- Sakurai, J., S. Fukuda, A. Mitsuda, H. Wada, and M. Shiga, 2000, *Physica B* **281** & **282**, 134.
- Sarrao, J. L., 1999, *Physica B* **259** & **261**, 129.
- Schiller, A., 1999, *Phys. Rev. B* **60**, 15660.
- Schiller, A., and K. Ingersent, 1995, *Phys. Rev. Lett.* **75**, 113.
- Schmidt, P., and H. Monien, 2002, eprint cond-mat/0202046.
- Schwartz, L., and E. Siggia, 1972, *Phys. Rev. B* **5**, 383.
- Shastri, B. S., and B. I. Shraiman, 1990, *Phys. Rev. Lett.* **65**, 1068.
- Shastri, B. S., and B. I. Shraiman, 1991, *Int. J. Mod. Phys. B* **5**, 365.
- Shvaika, A. M., 2000, *Physica C* **341-348**, 177.
- Shvaika, A. M., 2001, *J. Phys. Stud.* **5**, 349.
- Shvaika, A. M., 2002, eprint cond-mat/0205322.
- Shvaika, A. M., and J. K. Freericks, 2002, eprint cond-mat/0211451.
- Si, Q., G. Kotliar, and A. Georges, 1992, *Phys. Rev. B* **46**, 1261.
- Soven, P., 1967, *Phys. Rev.* **156**, 809.
- Subrahmanyam, V., and M. Barma, 1988, *J. Phys. C* **21**, L19.
- Tran, M.-T., 1999, *Phys. Rev. B* **60**, 16371.
- Velický, B., 1969, *Phys. Rev.* **184**, 614.
- Velický, B., S. Kirkpatrick, and H. Ehrenreich, 1968, *Phys. Rev.* **175**, 747.
- Vojta, M., and R. Bulla, 2002, *Phys. Rev. B* **65**, 014511.
- Wada, H., A. Nakamura, A. Mitsuda, M. Shiga, T. Tanaka, H. Mitamura, and T. Goto, 1997, *J. Phys.: Condens. Matter* **9**, 7913.
- Watson, G., and R. Lemański, 1995, *J. Phys. Condens. Matter* **7**, 9521.
- Wilcox, R. M., 1968, *Phys. Rev.* **174**, 624.
- Withoff, D., and E. Fradkin, 1990, *Phys. Rev. Lett.* **64**, 1835.
- Zhang, W., N. Sato, K. Yoshimura, A. Mitsuda, T. Goto, and K. Kosige, 2002, *Phys. Rev. B* **66**, 024112.
- Zlatić, V., and J. K. Freericks, 2001a, *Acta Phys. Pol. B* **32**, 3253.
- Zlatić, V., and J. K. Freericks, 2001b, *Open Problems in Strongly Correlated Electron Systems* (Kluwer, Dordrecht), volume 15 of *Nato Science Series II. Mathematics, Physics, and Chemistry*, p. 371.
- Zlatić, V., and J. K. Freericks, 2003, *Concepts in Electron Correlation* (Kluwer, Dordrecht), volume XX of *Nato Science Series II. Mathematics, Physics, and Chemistry*, p. XXX.
- Zlatić, V., J. K. Freericks, R. Lemański, and G. Czycholl, 2001, *Phil. Mag. B* **81**, 1443.
- Zlatić, V., and B. Horvatić, 1990, *Solid State Commun.* **75**, 263.

m_σ (m_η)	z -component of spin of electrons
$2s + 1$	number of σ states
t	hopping
t^*	rescaled hopping
$v(\epsilon)$	velocity operator
$w(x)$	phonon distribution function
$w_0 = 1 - w_1$	empty site density
w_1	localized electron (ion) density
x_i	phonon coordinate at site i
Γ^{cc}	irreducible charge vertex
Δ	superconducting gap at $T = 0$
Σ	self energy
Ω_{uc}	unit cell volume
α_{an}	anharmonic phonon potential (quartic)
β	$1/T$
β_{an}	anharmonic phonon potential (cubic)
$\gamma(\mathbf{q})$	parameter in charge susceptibility
$\eta(\mathbf{q})$	deviation from local susceptibility
ξ_0 ($\bar{\xi}_0$)	parameters for F_η calculation
κ	spring constant
$\lambda(z)$	dynamical mean field
μ	chemical potential, conduction electrons
μ_B	Bohr magneton
μ_f	chemical potential, localized electrons
$i\nu_l = i\pi T 2l$	bosonic Matsubara frequency
ψ ($\bar{\psi}$)	fermionic Grassman variable
$\rho(\epsilon)$	bare conduction electron DOS
ρ_{dc}	dc resistivity
ρ_e	itinerant electron density
ρ_f	localized electron density
$\sigma(\nu)$	optical conductivity
σ_0	conductivity unit
σ_{dc}	dc conductivity
τ	imaginary time
$\tau_\sigma(\omega)$	relaxation time
χ'	spin susceptibility
χ^{cc}	conduction electron charge susceptibility
$\bar{\chi}^{cc}$	pair-field susceptibility
χ^{cf}	mixed charge susceptibility
χ^{ff}	localized electron charge susceptibility
χ_{hyb}	hybridization susceptibility
χ_0	bare susceptibility
χ_τ	time-dependent conduction electron field
$i\omega_n = i\pi T(2n + 1)$	fermionic Matsubara frequency
\mathcal{H}	Hamiltonian
\mathcal{L}	Lorenz number
\mathcal{Z}	partition function
